Power Management in Electric Vehicles

- 4^{th} Semester Master Thesis -

AALBORG UNIVERSITY
STUDENT REPORT

MCE4-1029

Aalborg University
MSc. Energy Engineering - Mechatronic Control Engineering

The written presentation of this report is done in Overleaf, with OneDrive used for internal file-sharing and Slack for communications and project-management. Illustrations are made with Inkscape. For simulations, modelling and data processing MathWorks MATLAB and Simulink have been used.

Aalborg University, 28th of May 2021

Søren T. Madsen

Søren Thyregod Madsen
<stma14@student.aau.dk>

Christian Poul Nørgaard
<cpna16@student.aau.dk>

Institute of Energy Technology
Aalborg University
http://www.aau.dk

Title:
Power Management in Electric Vehicles

Theme:
Control of electric FSAE vehicle

Project Period:
Spring semester 2021

Project Group:
MCE4-1029

Participants:
Christian Poul Nørgaard
Søren Thyregod Madsen

Supervisor:
Erik Schaltz

Copies: 1

Page Numbers: 93

Date of Completion:
May 28th, 2021

Abstract:

AAU Racing is a team of students at Aalborg university who are building their first electric vehicle, the AAUER for use in the yearly FSAE competitions. The team has made some initial design choices with regards to components, but lack knowledge of control methods for electrical powerlines. This thesis compares control methods for traction control and anti-lock braking system, regenerative braking, field oriented control and maximum torque per ampere in regards to performance in the dynamic FSAE events. In order to accommodate this a MATLAB/Simulink model is established of the AAUER, based on knowledge from AAU Racing and design decisions made by the authors. The results show that MTPA with regenerative braking and a linear traction and anti-lock controller performs the best, scoring a total of 527.5 out of 600 possible, when compared to the event scores at FSG Hockenheim in 2012, when disregarding the skidpad event.

Preface

Acknowledgments

This is a Master Thesis report written by the group members of MCE4-1029. All members of this group are part of the 4th semester of the Master of Science in Energy Engineering, with a specialization in Mechatronic Control Engineering at Aalborg University. This master thesis was started in February 1^{st} 2021 and ended in May 28^{th} 2021. The title of the master thesis is Power Management in Electric Vehicles. This project was supervised by Associate Professor Erik Schaltz. The members of this group would like to thank Calspan and the FSAE Tire Test Consortium for making test data of the tires available for use in this report. A special thanks to Morten Nør for helping to provide information and measurements from previous cars AAU Racing has built.

Reading guide

A table of content is included at the start of this report where each chapter and section are displayed with their respective starting page. After the table of content, a complete nomenclature is included with all symbols, subscripts, and abbreviations used throughout this report. At the end of the report, a complete list of references is presented. Citations made throughout this thesis are done in Vancouver style.
The structure of the entire master thesis is as follows. In chapter 1 background information about the FSAE competition, including all of the different events, and AAU racing is presented. Chapter 2 presents the premise of the challenges associated with designing a well-performing drivetrain for the AAU race car. At the end of chapter 2, a series of proposed topics are selected to increase the performance of the AAU race car. Chapter 3 presents the problem formulation of the master thesis, including important limitations imposed both by the writer, but also restrictions imposed upon the design of the race car by FSAE. Chapter 4 aims to describe the driveline of the potential AAU electric race car. This also includes mechanical equations needed to explain vehicle dynamics which is then all combined into one large Matlab Simulink model. Chapter 5 includes all motor control designs and all extended motor control designs. Two motor control methods, and two extended

motor control methods are designed to later determine which is better. Furthermore, additional features such as regenerative braking and choice of controller reference are considered. Chapter 6 is used as both a validation of the designed controllers from chapter 5, but also a series of simulated events, as described in chapter 1, on the 2012 Hockenheim track. These simulations of the various events will then be used to calculate a predicted score if the designed electric race car was to have participated in the various events. Finally, chapter 7 is used to draw a conclusion based upon the results of chapter 6. Additionally, the results in chapter 6 are used as a platform for further discussion in chapter 7, and finally various unexplored, but potentially valuable, ideas are considered which were not presented in the thesis.

Contents

Nomenclature

Symbol	Description	Unit
a	acceleration	$\frac{m}{s^2}$
J	rotational inertia	Kgm^2
F	Force	N
m	mass	Kg
N	number of	—
g	gravitational acceleration	—
K	error constant	—
R	Radius	m
r	ratio	—
t	time	s
v	velocity	$\frac{m}{s}$
Q	Capacity	J
c	Coefficient	—
s	Laplace operator	—

Symbol	**Description**	**Unit**
β	Beta axis in stationary reference frame	—
τ	Torque	Nm
$\ddot{\theta}$	Angular acceleration	$\frac{\mathrm{rad}}{\mathrm{s}^2}$
$\dot{\theta}$	Angular velocity	$\frac{\mathrm{rad}}{\mathrm{s}}$
θ	Angle	rad
μ	Adhesion Coefficient	—
ρ	Fluid density	$\frac{\mathrm{kg}}{\mathrm{m}^3}$
ψ	Slip	—
ξ	-	Nm
ζ	Damping Coefficient	—
σ	Sliding Variable	—
ω	Angular Velocity	$\frac{\mathrm{rad}}{\mathrm{s}}$
ϕ	Angle between dq-voltage vectors	rad
α	Alpha axis in stationary reference frame	—
ζ	Damping Coefficient	—
χ	Equilibrium brake torque	Nm

Subscript	Definition
acc	Acceleration
const	Constant
e	electic
total	Total
d	d-axis
q	q-axis
mpm	
v	Vehicle
r	Rotational
g	Center of gravity
w	Wheel
RL	Resistance-Inductance
RC	Resistance-Capacitance
JB	Intertia-Friction
P	Proportional gain
I	Integral gain
c	Controller
cl	Closed Loop
ref	Reference
b	Brake
s	Settle
lyap	Lyapunov
r	Reaching
disturbance	Disturbance
DC	DC
max	Maximum
loss	Discharge Efficiency Factor
0	Initial Value
N	Nominal Value
pp	Pole Pair
drag	Drag
visc	Viscous Friction
em	Electro-magnetic
T	Traction
Burck	Burckhardt
Pacej	Pacejka
TH	Thevenin
Bat	Battery
L	Load
series	Series Connected
limit	Limit
parallel	Parallel
cell	Cell
discharge	Discharge
actual	Actual
ideal	Ideal
error	error
sample	Sample
delay	Delay

Subscript	Definition
ref	Reference
s	Stator
t	torque
p	Plant

Abbreviation	Definition
EV	Electric Vehicle
RB	Regenerative Braking
AAUER	Aalborg University Electric Racer
CV	Combustion Vehicle
DV	Driverless Vehicle
SoC	State of Charge
SoH	State of Health
PMSM	Permanent Magnet Synchronous Machine
DW	Distributed Windings
MMF	Magnetic Motive Force
WLTC	Worldwide Harmonized Light Vehicle Test Procedure
TC	Traction Control
ABS	Anti-lock Brake System
STSMC	Super-Twisting Sliding Mode Controller
OCV	Open Circuit Voltage
OC	Open Circuit
FDR	Final Drive Ratio

Chapter 1

Introduction

AAU Racing is a team of students at Aalborg University, who competes in the annual Formula Society of Automotive Engineers (FSAE). AAU Racing is making their first electric vehicle (EV), the Aalborg University Electric Racer (AAUER), for the EV category in FSAE to replace their current gasoline-powered car. As the team has not designed an EV before, design consideration will have to be made along the way.
The competition revolves around making a 1-man car design with certain criteria and restrictions. AAU Racing currently uses a car powered by an internal combustion engine as seen in Figure 1.1

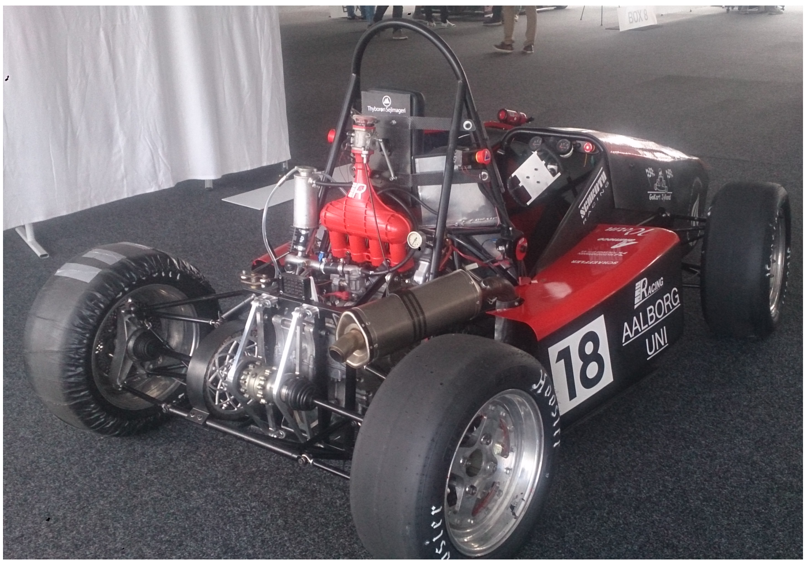

Figure 1.1: The Eighth generation combustion powered vehicle, built by AAU Racing

An incomplete CAD drawing was made available by AAU Racing as seen in Figure 1.2 with dimensions and part description added.

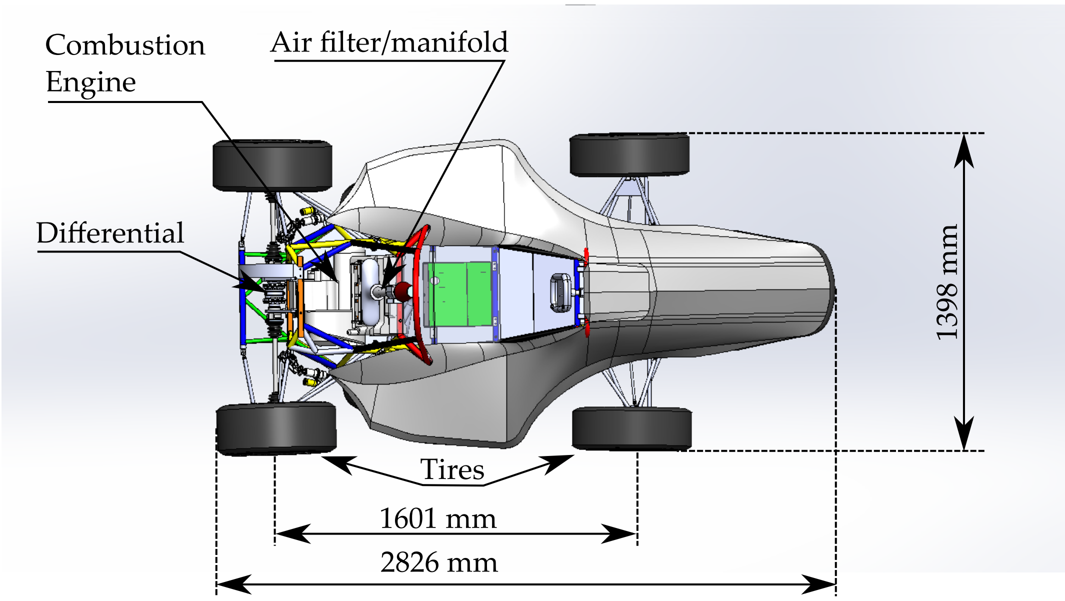

Figure 1.2: The Eighth generation combustion powered vehicle, built by AAU Racing

Cars designed with combustion engines have different limitations compared to cars with electrical motors, however, the limitations have similar functions such as limiting the maximum power output of the powertrain. This is both an equalizing limitation such that smaller teams can still be competitive, but also a safety precaution as higher speeds could lead to worse accidents. As an example, combustion engines must have an air intake diameter of $20[mm]$ while a battery pack for electric cars may not output more than $80[kW]$ [8][CV 1.7.2] & [8][EV 2.2.1]. While there are many rules specifically for the safety of the car, driver, and the general audience. There are not as many restrictions on general design such as how many cylinders a combustion engine may have or how many electric motors and the type of motor.
The car will have to pass a scrutiny inspection colloquially known as "scrutineering" where the car must pass four tests to make sure it is safe to drive and to have driven on the tracks. The tests are as follows:

- Technical Inspection: Judges will select rules at random and check whether the car is compliant.
- Tilt Inspection: The car, with a driver seated, will be tilted to $60°$ measured from horizontal and inspected. No parts may fall off and no fluids may leak.
- Noise Test, combustion engine only: The rules state a maximum allowed noise level of $110[dB]$, this is tested at a specific RPM.

- Brake Test: The car is allowed to accelerate up before braking hard. The test is passed when the car has shown capable of blocking all four tires at the same time while moving.
- Rain test, electric only: The car is placed in an artificial rain environment for $240[s]$, half the time with artificial rain, the other half without. For the entire duration, the Isolation Monitoring may not trip i.e. no short circuits may occur.

When Scrutineering is passed, the car can finally enter the events. An event is simply a challenge, it could be covering $75[m]$ distance the fastest, starting from a standstill while a different event is about the cars design and the decision that lead up to it where the team will have to answer any question posed by judges much similar to a master thesis defense in a university. In total there are 8 events during competition and they are split into two types with three categories. The two types are static and dynamic and the three categories are Combustion Vehicle (CV), Electric Vehicle (EV), and Driverless (DV). CV and EV have the same dynamic events while DV has one event replaced. The Dynamic type relates to driving the car, they list as follows:

- Acceleration: The car must cover a straight $75[m]$ road in the shortest amount of time possible, starting from a standstill.
- Skidpad: The car must drive in circles with an inner diameter of $15.25[m]$ in the shortest time possible. The car does two circles both clock- and anti-clockwise. The fastest time in either direction is counted.
- Autocross: Similar to traditional track racing but with a limited number of cars on the track at any given time. The track is designed to specifications from the rules with the fastest time giving maximum points.
- Endurance: The car drives on the same track as in Autocross, but must now complete multiple laps until $11[km]$ is reached. The car is then forced to do a driver change and drive another $11[km]$. For CVs, refueling is not allowed and for EVs charging or changing the battery is not allowed.
- Efficiency: While the car is driving the Endurance event a measurement of energy usage is recorded. CVs have their fuel tank filled to a measurement point and refilled after endurance to measure liters of fuel consumed, while EVs must measure the current and voltage of the battery pack while driving.

DVs are not competing in the Endurance event but instead have a Track Drive event similar to the Autocross event but with ten laps.
The three last events are static types i.e. the car is not moving, but judges are asking questions to the team members. The static events are as follows:

- Business Plan: The team has developed a business plan before arriving at the competition. The plan revolves around the car being a prototype for a profitable business opportunity.
- Cost and Manufacturing: The team member's understanding of manufacturing costs is evaluated and is based on a Cost Report which has been submitted before the competition.
- Engineering Design: The team members will answers questions about the engineering design of the vehicle. What thoughts underlie the ideas, what are the design goals, and many other things. The format is akin to that of a university exam with judges asking the questions, but the questions are directed at a team member with the best understanding for the given question. a total of eight team members are present at any given point to respond to questions from eight judges.

The total amount of points that can be scored in the eight events are shown in table 1.1.

Event	Maximum points
Acceleration	75
Skidpad	75
Efficiency	100
Autocross	100
Endurance	325
Business Plan	75
Cost & Manufacturing	100
Engineering Design	150
All Events	**1000**

Table 1.1: Table of the maximum points that can be scored in the 4 events.

During the competition, it is possible to score a total of 1000 points with 325 being from static events [5].
The score granted at the dynamic events is relative to the best time, that is, the best time gets maximum points while the scores of the remaining teams are calculated based on time relative to the best. The equations used to calculate the scores can be found in Appendix C.
The scores awarded for the static events are based on the judges' opinions.
From the points granted by each event, it is clear that doing well in the endurance event is important as it accounts for close to half the points granted by the dynamic events. However, good performance in endurance will not exclude good performance in other dynamic events, it is the contrary. Doing well in endurance would

also be reflected in the autocross event as it is the same track but with multiple laps. Doing well in the acceleration event can also be reflected in the autocross and endurance event as the many turns of the track will allow many opportunities for the car to accelerate out of corners after having decelerated before it. An efficient powertrain will have indirect effects on car performance, such as weight reduction, as less fuel or batteries are needed.
To win the competition the maximum amount of points possible must be scored. This is not done by outperforming competing teams in one single event but all events. While manpower and time are limited, ingenuity is not. For this reason, the effort of this thesis will be focused on the most time-effective improvements possible to do to an EV for the FSAE competition. While things such as aerodynamic packages and weight reductions from chassis design are considered sophisticated improvements, that is, improvements to be done on an already well-designed vehicle and will therefore not be considered in this thesis. As the AAUER is the first electric vehicle designed by AAU Racing, the team will start with a simple vehicle design. This means a single electric motor with a similar driveline as the G8. This also means the control methods and some component designs, will have to be developed from scratch. The control of both powertrains has a similar purpose, to make sure the torque from the powertrain is efficiently and effectively put to use. Powertrain control will thus be the main focus of this thesis.

Chapter 2

Problem Analysis

2.1 Problem Identification

As no work has previously been done by the team, to control an electric powertrain, this is considered an open field of development. The most important control to have is motor control. This can, however, be approached in different ways and will be investigated. Motor control can be improved with Traction Control(TC), similar to what is used in modern cars' Anti-lock Braking System (ABS) but with improved acceleration capability as well. Thus, TC will be investigated. As an electric motor can also act as a generator the possibility of regenerative braking is available and will be investigated as well. As regenerative braking will recharge the battery pack, it is important to not overcharge the battery pack or charge with a higher voltage or current that is allowed by the FSAE rules or what the battery pack is designed for. Proper battery management is not considered a performance increase but is necessary to avoid faults while the AAUER is racing. To better recharge, the battery pack information about its remaining energy level is needed and thus methods for estimating this will be investigated. The list of topics to investigate is as follows,

- Regenerative Braking
- TC/ABS
- State of Charge Estimation
- Motor Control

2.1.1 Regenerative Braking

The software Optimum Lap is used for simulating the car on a track that was used for the endurance event. Optimum lap uses a car model with parameters specified by the user. The parameters specified can be seen in Appendix A. The test track was chosen to be a recreation of the endurance track from the 2012 Formula Student Germany (FSG). The track is shown in Figure 2.1

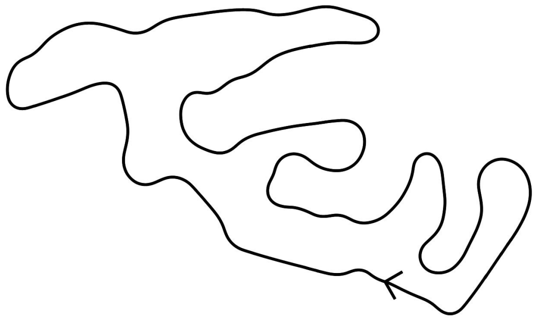

Figure 2.1: Outline of the FSG test track from the 2012 competition

The track is 1267$[m]$ long. Optimum Lap can calculate the speed of a car moving along the track using the parameters in Appendix A. The parameters are based on the latest CV built by AAU Racing but modified to fit with an electric motor instead. The electric motor is a Permanent Magnet Synchronous Machine (PMSM) with the specifications in Appendix A. The decision to use a PMSM has been made by AAU Racing. Other parameters such as wheel radius and car mass remains the same as no structural design changes are made.
From the simulation, the speed of the car driving on the FSG 2012 endurance track, can be seen in Figure 2.2 for a single lap. As previously discussed, a negative change in speed means lost energy to mechanical braking i.e. heating the braking discs. This energy can be approximated by calculating the change in kinetic energy from a local maximum speed to a local minimum.

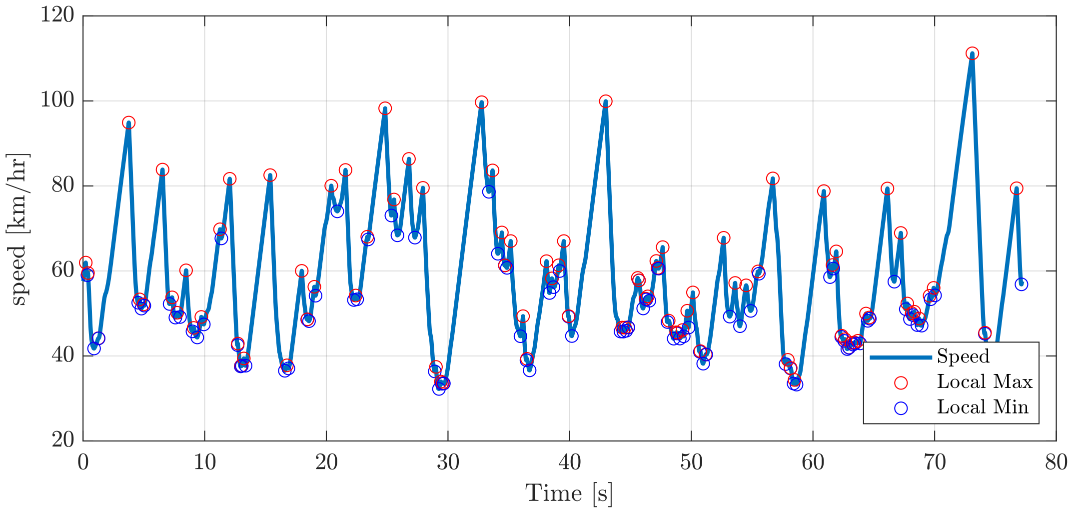

Figure 2.2: Speed curve from Optimum Lap with local maximums and minimums marked.

Calculating the kinetic energy at a local maximum and subtracting the energy from the following local minimum then gives the wasted energy but does not take into account the energy lost to frictions while decelerating. Calculating this gives an energy waste of $1.26 \cdot 10^6[J]$ As this will only be for one lap, it will be multiplied with the number of laps needed to reach $22000[m]$ rounded up. The number of laps is then $\frac{22000[m]}{1267[m]} = 17.36 \approx 18$. This gives a total wasted energy of $2.26 \cdot 10^7[J]$. From Optimum Lap, the power used by the car is found. This data can then be integrated for time to find the energy expended to drive one lap. The energy need is found to be $2.82 \cdot 10^6[J]$. The energy needed to drive 18 laps is then $2.82 \cdot 10^6[J] \cdot 18 = 5.07 \cdot 10^7[J]$ with no regenerative braking. This includes a driveline efficiency of $\eta_{DL} = 0.90$ and for the PMSM $\eta_{PMSM} = 0.90$. If it was possible to recover 100% of the lost kinetic energy, the energy needed to drive 18 laps would be reduced by $\frac{2.26 \cdot 10^7[J]}{5.07 \cdot 10^7[J]} \cdot 100 = 44.62\%$. It would be incorrect to conclude a reduction of the battery pack mass by 44.62%, since it would be ignoring important concerns about battery management and health, however, regenerative brake will still enable a mass reduction in the battery pack while improving the efficiency score in the competition.

2.1.2 Battery Management

The battery of the AAUER is also important to investigate since this will be the power source of the EV. The battery will be lithium-ion based due to its well-known high capacity and discharging limits. Management of the lithium-ion battery is important since it must operate within a specific temperature and voltage window to avoid degradation of the battery and maintain safe operations[19]. Quantities such as State of Charge(SoC) and State of Health(SoH) can be used to determine the health of the battery. SoC is used the measure the amount of remaining energy in the battery while SoH is a measure of a battery's ability to store energy relative to its nominal capabilities[16]. SoC can be measured in various ways, some of these methods include[25, pp. 274, 277],

- Coulomb counting
- Model-based estimation of SoC

Coulomb counting is a very simple method that integrates the current measurement over some time as shown in equation (2.1).

$$SoC = SoC_0 + \frac{1}{C_N} \int_{t_0}^{t} (I_{batt} - I_{loss})dt \tag{2.1}$$

Where I_{batt} is the measured current entering the battery, I_{loss} is a discharge/charge efficiency factor, SoC_0 is the initial state of charge of the battery, and C_N is the nominal capacity. Nominal capacity is determined from a cycling test where the battery is charged fully and discharged to the cut-off voltage at rated current[16]. One of the main disadvantages is the fact that Coulomb counting suffers from drift due to the integral term. This error, due to drift, will increase as time progresses[25, p. 274].

2.1.3 Slip Control

In this project, TC and ABS will be considered as two individual parts which make up the combined slip control for the AAUER [26]. Both control strategies use the slip ratio, ψ, between the tire and the road surface to determine the required motor torque to accelerate the vehicle as fast as possible [2, p. 49]. The slip ratio of a vehicle is related to the difference between the angular velocity of the wheel and the resultant velocity of the vehicle. The adhesion coefficient, μ, of a given road surface depends on the slip ratio. It is possible to obtain the adhesion coefficient of a surface using optical sensors or various estimation techniques such as the extended Kalman filter[39]. Different road surfaces have varying adhesion coefficients depending on road conditions. A general trend of μ as a function of slip ratio is shown in Figure 2.3

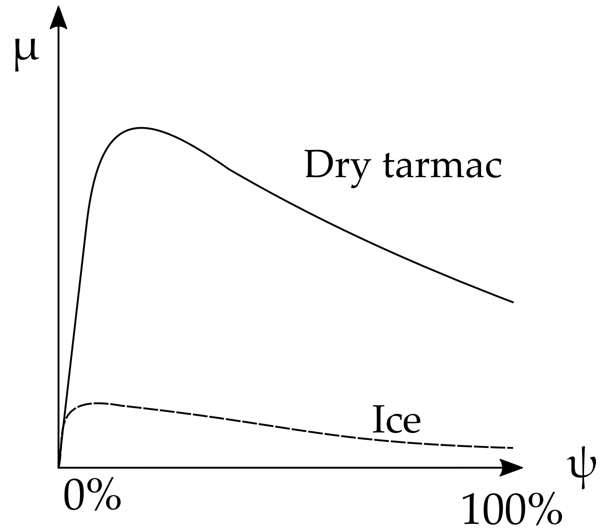

Figure 2.3: Figure 2.3 is inspired from [39] using the Burckhardt friction model. Adhesion coefficient as a function of slip ratio on two different road surfaces.

As can be seen from Figure 2.3 different road conditions have different adhesion coefficients. From Figure 2.3 there exists an optimal area where a certain amount of slip, $15-25\%$, provide a large adhesion coefficient value[2, p. 38]. Via Optimum Lap simulation, it is seen from Figure 2.4 that a higher adhesion coefficient enables higher acceleration.

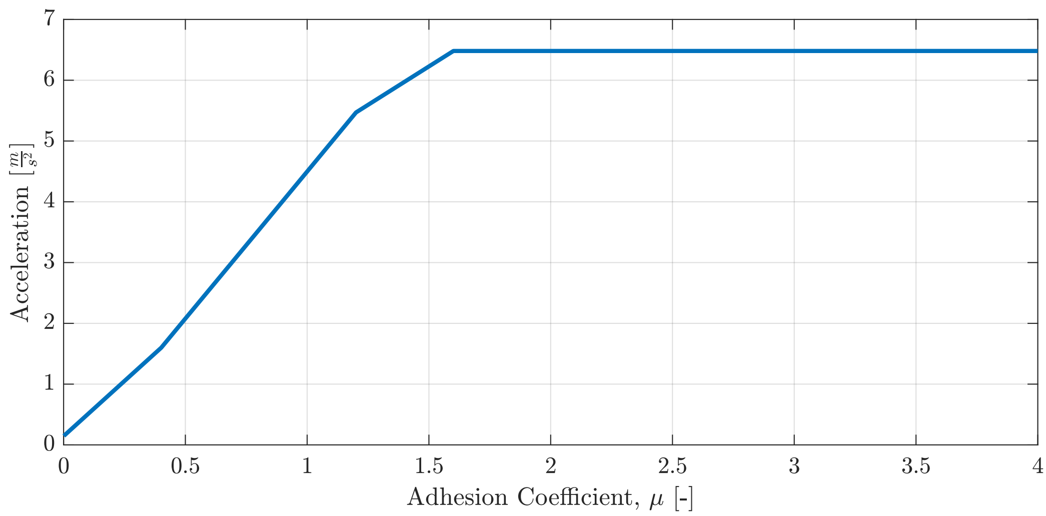

Figure 2.4: Acceleration as a function of the adhesion coefficient, calculated with Optimum Lap on the 2012 FSG test track.

As seen from Figure 2.4 eventually the limiting factor for vehicle acceleration is no longer the adhesion between the road surface and the tire, but restrictions set by the motor itself. As a result, increasing μ from two onward does not result in an increased acceleration. In [34], launch control is implemented in a rear-wheel drive hybrid electric vehicle using a PID controller. With launch, control implemented it is possible to reduce the time taken to accelerate from $0[mph]$ to $30[mph]$ by 10%. The goal of TC is to keep the slip at an optimal point when the vehicle accelerates. The way which this is done is by either manipulating the output torque of the motor or the braking torque[2, pp. 48–49]. In [2, pp. 53–55] a fuzzy PID TC system is implemented and thus able to accurately estimate the slip for optimal acceleration as shown in Figure 2.5.

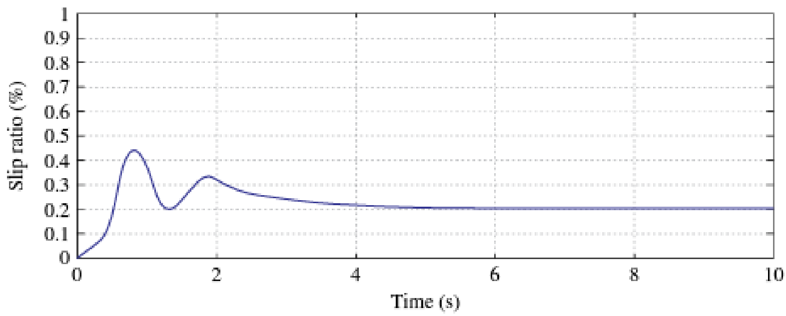

Figure 2.5: Esimated slip using a fuzzy PID[2, p. 54].

As seen from Figure 2.5 the slip initially overshoots, but after $3[sec]$ the slip remains in its optimal range. Thus providing the optimal conditions for the vehicle to accelerate. In [21] a nonlinear controller with integral feedback is used in a ABS system. Figure 2.6 shows the results of a test where the vehicle brakes from $72\left[\frac{km}{h}\right]$ on a flat dry road

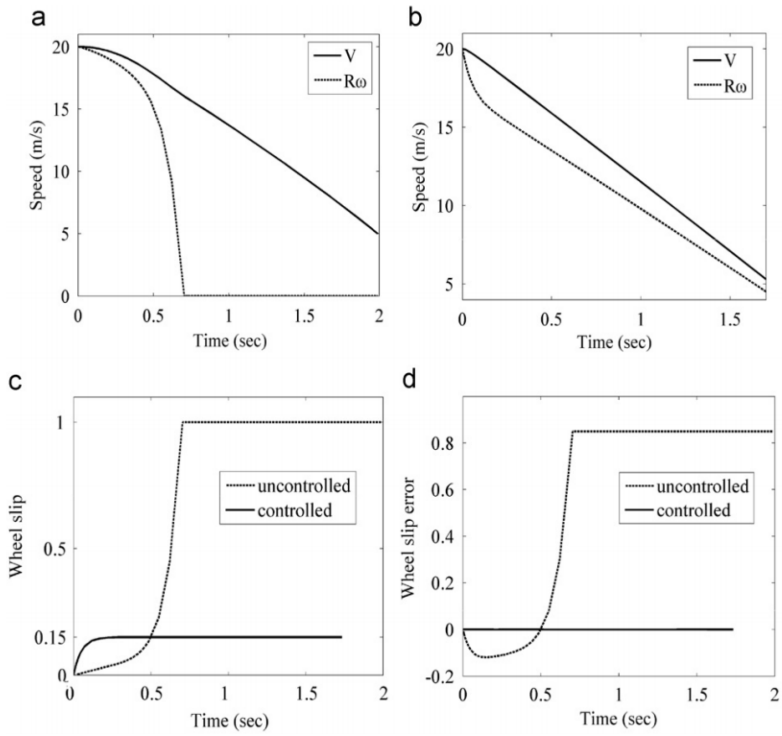

Figure 2.6: Non linear control with integral feedback with and without ABS control strategy[21]. (a) and (c) is the brake test without any ABS control, (b) (d) is with ABS control implemented for the same test. V is the vehicle speed and Rω is the wheel angular speed.

As can be seen from Figure 2.6 without the ABS implemented the wheels lock and as a result, the wheel slip increases to 100% which will result in loss of control of the vehicle while braking. For the same test, the nonlinear controller ensures that the wheels do not lock and as a result, the vehicle decelerates faster.

2.1.4 Motor Control Strategies

The electric motor which will be implemented in the AAUER will be a EMRAX Model 228 High Voltage PMSM with the specifications shown in Appendix A. A photo of the EMRAX 228 can be seen in Figure 2.7 and a technical drawing in Figure 2.8.

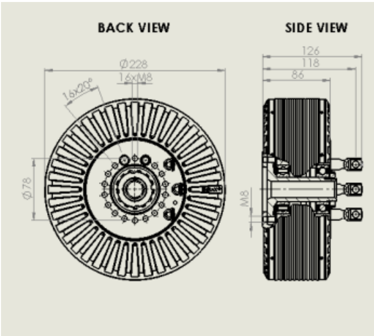

Figure 2.7: Back and side view of the EMRAX 228 with general dimensions [4, p. 9]

Figure 2.8: Front picture of the EMRAX [4, p. 9]

The torque equation for the PMSM, as seen in equation (2.2), is obtain via energy considerations of the PMSM [18, pp. 157–158].

$$
\begin{aligned}
\tau_{em} &= \frac{3}{2} N_{pp} (\lambda_d i_q - \lambda_q i_d) \\
\tau_{em} &= \frac{3}{2} N_{pp} ((L_d - L_q) i_d i_q + \lambda_{mpm} i_q)
\end{aligned}
\tag{2.2}
$$

N_{pp} is the number of pole pairs, L_d, and L_q is the inductances for the d and q-axis respectively. λ_d and λ_q are the magnetic flux for the d and q axis respectively. λ_{mpm} is the axial magnetic flux. As can be seen from equation (2.2) the PMSM produces both a reluctance torque and a magnetic torque. Since this PMSM is salient, $L_d \neq L_q$ as can be seen in Appendix A, this means that the PMSM can produce reluctance torque as well. A possible way to achieve linear torque control of the PMSM would involve setting $i_d = 0$ thus eliminating the reluctance torque component and making the generated motor toque only dependent on the i_q current. This linear torque control is known as Field-Oriented Control (FOC)[23]. The resultant equation for the motor torque can be seen in equation (2.3).

$$\tau_{em} = \frac{3}{2} N_{pp} (\lambda_{mpm} i_q) \tag{2.3}$$

By setting the $i_d = 0$ the reluctance torque component is eliminated as a result the maximum torque which the PMSM could produce is not utilized. Different nonlinear control methods exist for the PMSM to fully utilize this reluctance torque, such as Maximum Torque Per Ampere (MTPA). MTPA uses the maximum current and voltage constraints set by the inverter and equation (2.2) to determine i_d and i_q which produces the highest possible torque. Another possible control method is the Direct-Torque Control (DTC) method. The DTC uses the angle between the stator and the rotor flux linkage in the PMSM to control the output torque. This is achieved by changing the stator flux linkage of the PMSM using the voltage vector supplied to the inverter. However, the unmodified DTC since there are only 8 positions for the voltage vector results in unwanted torque and flux linkage ripples. Since the voltage vector will snap between these eight positions. This leads to poor steady-state performance for DTC[38] and as such will not be investigated further in this thesis.

2.1.5 Summary

From section 2.1.1 it can be seen that regenerative braking has the potential to recover a significant amount of energy whenever the AAUER brakes. With the ability to recover energy the size of the battery could potentially be reduced. This will benefit the AAUER's performance in the Endurance, Acceleration, and Efficiency events. When charging the battery it is important to track the SoC of the battery. Coulomb counting is a simple and straightforward method, however, it suffers from drift. Estimation of the SoC will help manage how much energy can be regenerated while avoiding degrading the batteries.
The launch control will be vital to perform well in the acceleration event. TC will still be useful for autocross and endurance since the AAUER needs to accelerate out of corners on the track. TC will ensure that this acceleration is the highest possible with the optimal slip ratio. This means that TC will also have a positive effect on the efficiency event since the motor torque will not be used frivolously when accelerating. This will benefit the AAUER's performance in the Acceleration, Autocross, Endurance, and Efficiency events.
Various motor control strategies have been investigated in section 2.1.4. FOC and DTC offer easy implementation solutions for torque control of the motor. However, both of these techniques have different disadvantages. FOC uses $i_d = 0$ ref and as a result, any reluctance torque will not be utilized. The unmodified DTC suffers from torque and flux linkage ripples and as a result poor steady-state performance. MTPA utilizes both the reluctance torque and the magnetic torque of the PMSM.
A summary of the control methods which will be implemented and where they work best is seen in section 2.1.5.

	Acceleration	Autocross	Endruance	Efficiency
Regnerative Braking		+	+	+
Sip Control	+	+	+	+
SoC Estimation			+	+
MTPA/FoC	+	+	+	+

Chapter 3

Problem Formulation

3.1 Problem Description

AAU Racing is building an EV from scratch and needs to develop all the needed control methods, while also choosing components, to make it run. For the team to be competitive the control methods must be the best possible. Therefore a comparison of different control methods is needed to tell what works the best for this specific application. Motor control, regenerative braking and slip control are all performance related, while SoC estimation is a necessity to avoid battery degradation and proper use of regenerative braking. The goal of this thesis is thus:

To make a comparative study of Motor control, regenerative braking and slip estimation methods, with SoC estimation as a necessity for proper operation of the AAUER, in order to find the best combination of methods for AAU Racing to use

3.2 Limitation

Limitations for this project are associated with the limitations of the FSAE rule set. The impactful limitations to this thesis include:

- A battery pack power limit of 80 kW at any given time.
- A maximum of 600V DC between any lines.
- The AAUER has yet to be build making testing not possible.
- Powertrain design considerations will not be made, as AAU Racing makes such decisions.

3.3 Reading Guide

The coming chapters are organized in a certain order for easier consumption by the reader. Chapter 4 serves to explain a MATLAB/Simulink testbed Model. The model is representative of a EV's powerline and certain car dynamics. The model will serve as a testbed for the control strategies and estimation methods that are mentioned in chapter 2. The specific strategies and methods are derived, explained, and implemented in chapter 5, with multiple presented for each strategy or method. Chapter 6 will contain results of the strategies and methods shown in chapter 5. Chapter 7 will conclude the thesis.

Chapter 4

Testbed Modelling of AAUER Platform

4.1 The AAUER

To test different control strategies, a mathematical model is established for the AAUER, in MATLAB/Simulink. The simulation will act as a testbed for the control strategies and estimation methods, as well as different combinations of them. Some assumptions are made to model the power train, wheel, and car equations and will be explained throughout the chapter. The AAUER will have a similar driveline to the G8, that is, the components after the G8's gearbox in the powertrain, will remain the same. The powerline of the AAUER can be seen in 4.1.

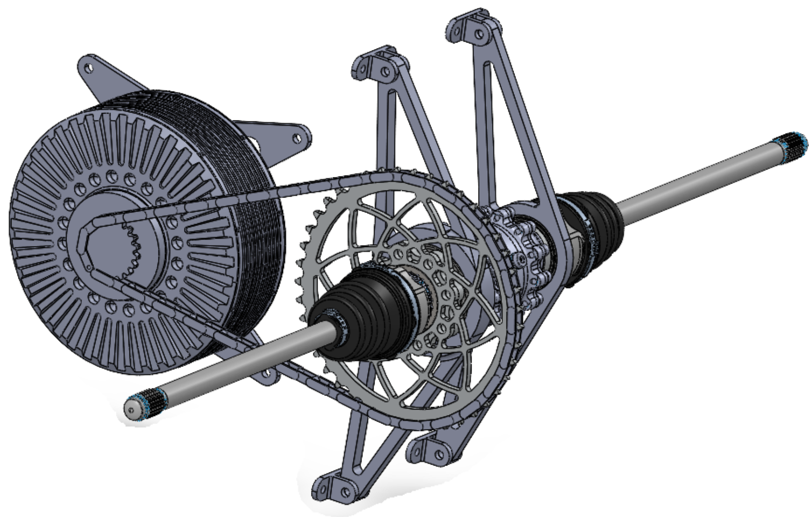

Figure 4.1: powerline of the AAUER

This chapter will be divided into mechanical and electrical sections. The mechanical section covers the equations related to the dynamics of the wheel and car. The electrical section includes descriptions of Space Vector Modulation, voltage source inverter dynamics, the battery package, and the PMSM. All of this can be seen in Figure 4.2.

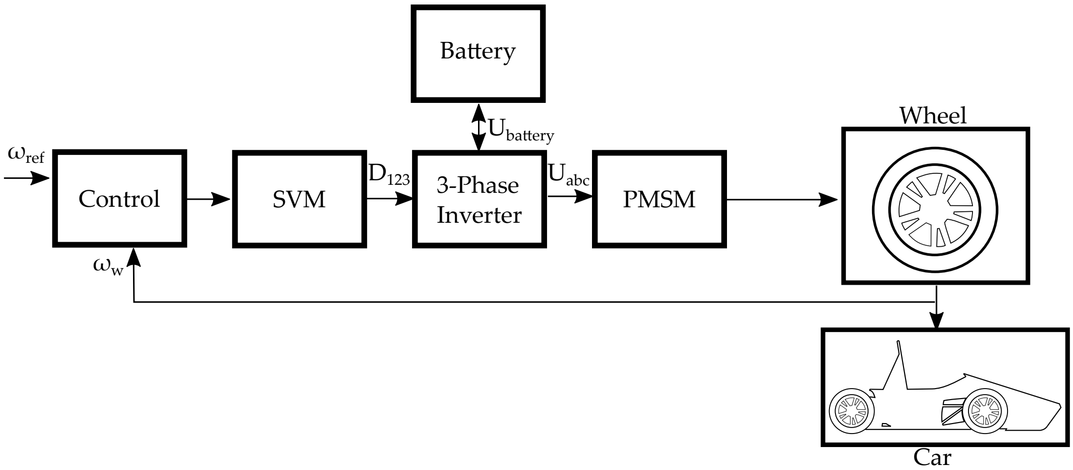

Figure 4.2: Diagram of the general simulation structure of both the mechanical and electrical part.

4.1.1 Mechanical Model

The mechanical model covers frictional forces, car and wheel model, and finally how the car and wheel are connected through adhesion as a function of slip ratio.

Friction

The AAUER is modeled as inertia with two types of friction. The inertia of the AAUER is the measured mass based on the latest combustion-powered car including a $70[kg]$ driver. The first friction is viscous which will be modeled with a friction coefficient affecting the wheel. It was not possible to retrieve this empirically from the AAUER itself so instead a preexisting rolling resistance was retrieved from a similar racer[7]. The viscous friction force is given by equation (4.1)

$$F_{visc} = c_{visc}\omega_w \tag{4.1}$$

ω_w is the feel speed and c_{visc} is the viscous friction coefficient. The second friction is related to the aerodynamics of the AAUER, it is modeled after the drag force in equation (4.2)

$$F_{drag} = \frac{1}{2}\rho A c_{drag} v^2 \tag{4.2}$$

v is the speed of the AAUER, ρ is the fluid density and c_{drag} is the drag coefficient. Values of the different parameters can be found in appendix A

Wheel Model

The wheel dynamics of the car are accounted for using Newton's 2^{nd} Law.

$$\sum \tau = J_w \dot{\omega}_w$$
$$\dot{\omega}_w = \frac{\tau_{em} - \tau_b - R_w F_T - R_w F_{visc}}{J_w} \tag{4.3}$$

It should be noted that different scenarios exist for τ_e and τ_b. That is

Motor Torque

$$\tau_e = \begin{cases} \text{Acceleration} & \tau_{em} > 0 \\ \text{Motor Brake} & \tau_{em} < 0 \end{cases} \tag{4.4}$$

Brake Torque

$$\tau_b = \begin{cases} \text{No Mechanical Braking} & \tau_b = 0 \\ \text{Mechanical Braking} & \tau_b > 0 \end{cases} \tag{4.5}$$

For equation (4.4) two scenarios can take place. One of the two possibilities, τ_e is positive and the torque contribution accelerates the AAUER. The other possibility τ_e is negative and it decelerates the AAUER through motor braking. τ_b represents the braking torque as a result of mechanical braking. These different scenarios will become important later when considering regenerative braking. R_w is the radius of the wheel, F_T is the traction force that propels the car forward, F_w is viscous friction force and J_w is the equivalent rotational inertia of the powerline. This includes the components shown in Figure 4.1 but also the wheels which are not shown in the Figure 4.1.

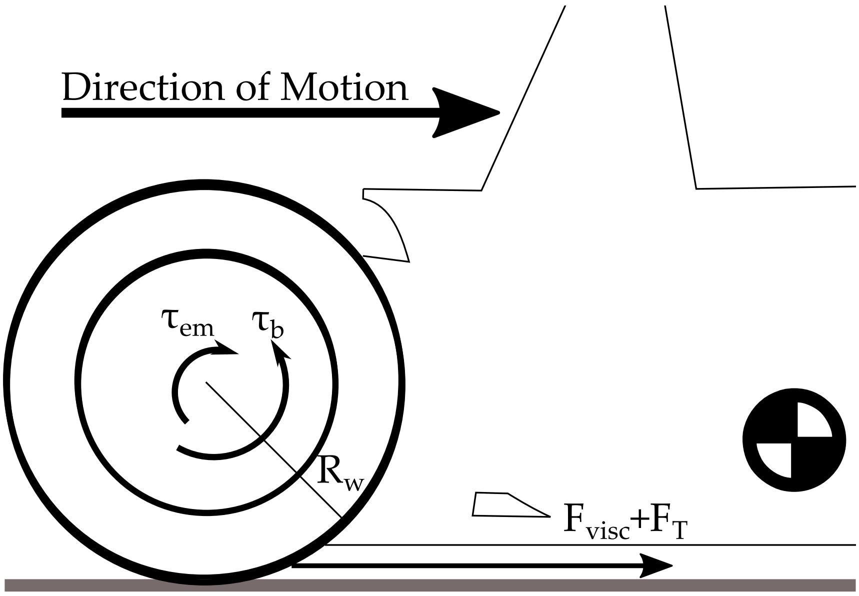

Figure 4.3: Wheel of the AAUER

The tractive force is generated between the tire and the surface of the road. The equation for the tractive force can be seen in equation (4.6)

$$F_T = \mu(\psi)N_v \tag{4.6}$$

μ is the adhesion coefficient between wheel and road surface, N_v is the normal force of the tire. From a previous competition it is known that 52% of the AAUERs weight is placed on the rear wheels. As seen in equation (4.6), the tractive force of the wheel is dependent on the adhesion coefficient which is dependent on the slip ratio between the wheel and road surface. Slip occurs whenever the tractive force of the wheel exceeds the maximum tractive force due to the adhesiveness between the wheel and the road surface[3, pp. 27–28]. In other words, slip occurs when the movement of the wheel is greater than the translational movement of the vehicle. The slip ratio is defined in equation (4.7)

$$\psi = \frac{(v_w - v)}{\omega}$$

$$v_w = \omega_w R_w$$

$$\omega = max(\omega_w R_w \vee v) \tag{4.7}$$

Where ω_w is the angular velocity of the wheel. ω is either the max value of v_w or v depending on if the vehicle is accelerating or decelerating[26, pp. 7–8]. equation (4.7) is only valid for the forward motion of the vehicle. This is sufficient for the design of the AAUER since it is not allowed to be able to reverse [10][D2.2.2].

Car Model

The acceleration of the vehicle can be described using Newton's 2^{nd} Law.

$$\dot{v} = \frac{F_T - F_{drag}}{M_v} \tag{4.8}$$

F_v is the drag force experienced by the vehicle as a whole and M_v is the mass of the vehicle and driver. With equation (4.8) it is then possible to describe the overall dynamics associated with the vehicle. The translational velocity in equation (4.8) has a equivalent angular velocity if divided by R_w.
Combining equations (4.3) and (4.8) a comprehensive system model of the entire wheel-car system can be seen in equation (4.10)[26, p. 11].

$$\dot{v} = \frac{N_v}{M_v}\mu(\psi) - \frac{F_{drag}}{M_v} \tag{4.9}$$

$$\dot{\omega}_w = \frac{-R_w F_{visc}}{J_w} - \frac{R_w N_v}{J_w}\mu(\psi) + \frac{\tau_{em} - \tau_b}{J_w} \tag{4.10}$$

With equation (4.10) it is possible to determine both the wheel and vehicle dynamics as a function of the slip.

Adhesion Model

For the car model to work, a correlation between slip and the adhesion coefficient is needed. This is can be done with either the Burckhardt equation or the Pacejka equation, which is sometimes also known as the Magic Equation. The Burckhardt equation is shown in equation (4.11) and the Pacejka equation in equation (4.12)

$$\mu(\psi) = (c_{1,Burck}(1 - e^{-c_{2,Burck}\cdot\psi}) - c_{3,Burck}\cdot\psi)e^{-c_{4,Burck}\cdot\psi\cdot v} \tag{4.11}$$

$$\mu(\psi) = c_{3,Pacej}\cdot sin(c_{2,Pacej}\cdot tan^{-1}(c_{1,Pacej}\cdot\psi - c_{4,Pacej}(c_{1,Pacej}\cdot\psi - tan^{-1}(c_{1,Pacej}\cdot\psi)))) \tag{4.12}$$

For Burckhardt, the parameters c_1, c_2, c_3 and c_4 are chosen based on the road surface [14][p. 37-40],[28]. For Pacejka the parameters B, C, D and E are chosen based on the road surface[14][p. 40]. The AAUER will only be driving on the tarmac and thus only one set of coefficients is needed, if the wet surface wants to be considered, a new set of coefficients are needed. Measurement data from a company called Calspan are available to AAU Racing for use. The measurements are done with the same model of slick tire that the G8 uses and the AAUER will be using. These measurements are used to fit the parameters in equation (4.11) and equation (4.12).

The curve fitting tool in MATLAB has the option to fit a custom equation to data, as seen in Figure 4.4

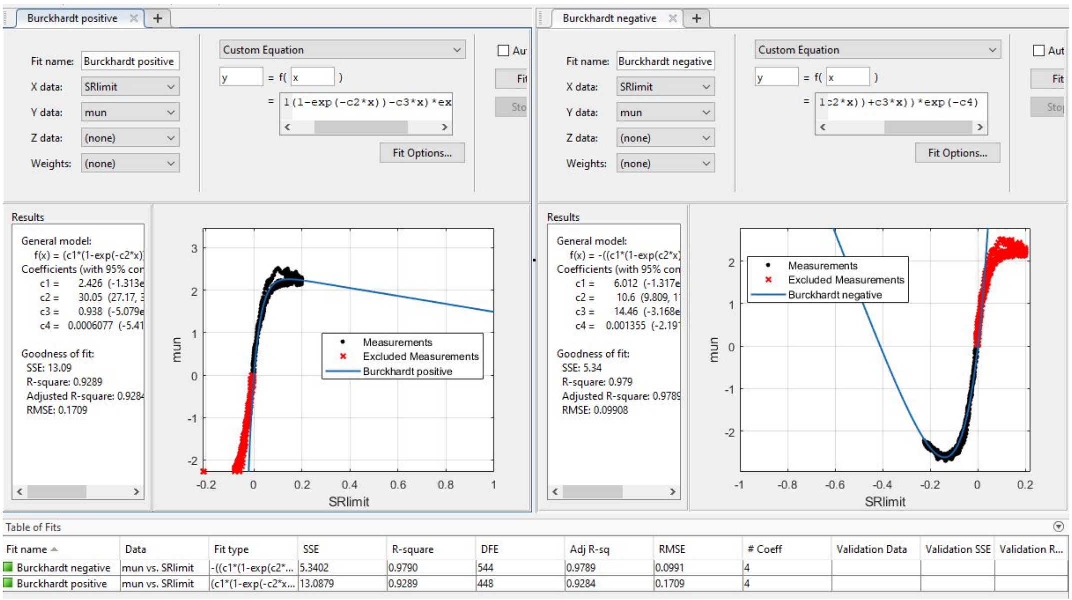

Figure 4.4: Screenshot of the MATLAB fitting tool used to fit c_1, c_2, c_3 and c_4 in the Burckhardt equation.

The fitted Burckhardt for positive slip has a $R^2 = 0.9289$ while the fitted Burckhardt for negative slip has a $R^2 = 0.9790$. From the equation is clear that this Burckhardt equation does not account for the negative slip ratio. This problem is circumvented by fitting a second Burckhardt equation to the data for negative slip. This means the adhesion coefficient has a different absolute value for the same positive and negative slip ratios as seen in Figure 4.6.

The coefficients of the Pacejka equations are fitted using the same method. The fitted equation is shown in figure 4.5 with a $R^2 = 0.9924$.

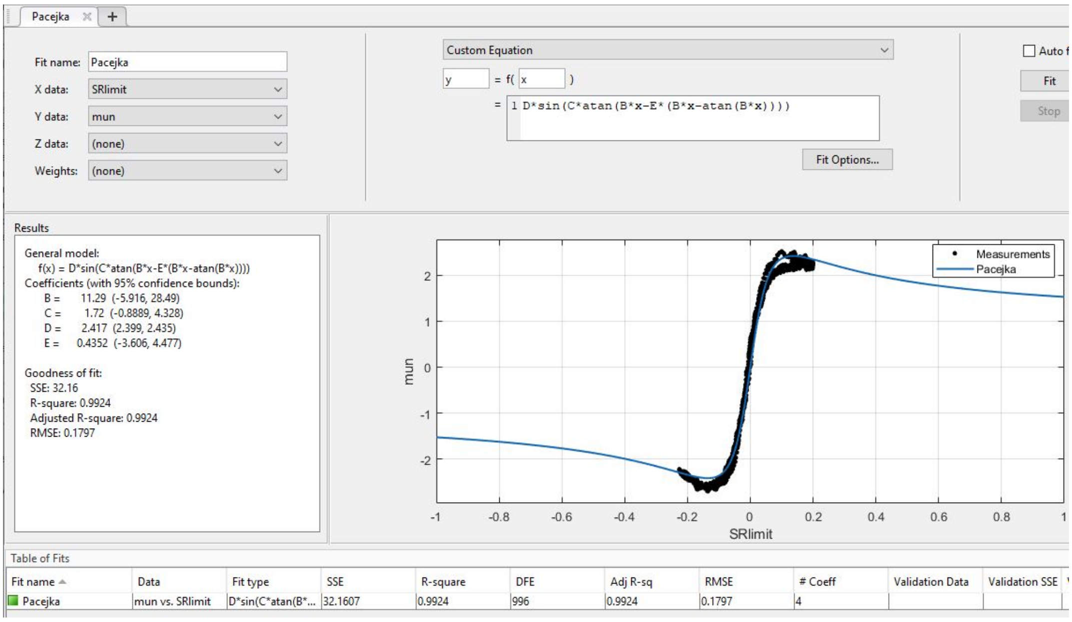

Figure 4.5: Screenshot of the MATLAB fitting tool used to fit B, C, D and E in the Pacejka equation.

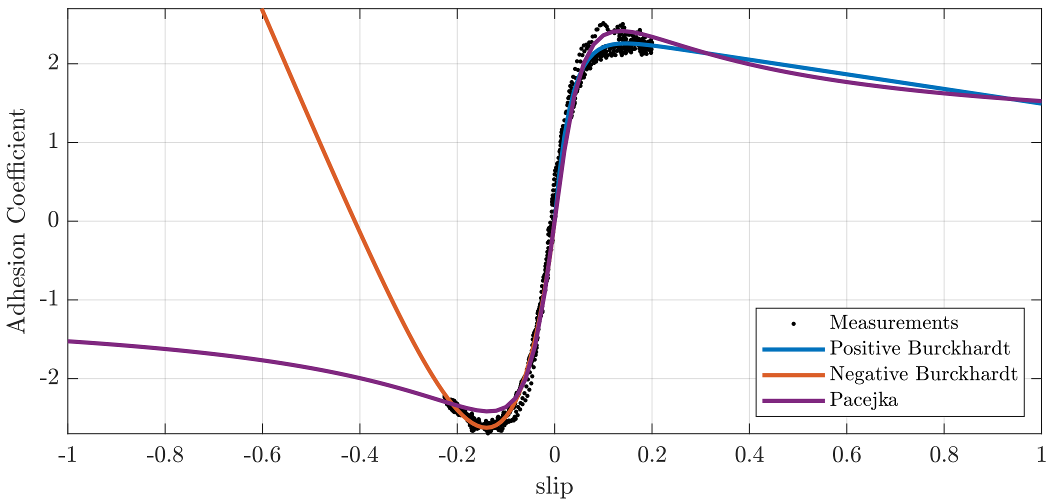

Figure 4.6: A plot of the fitted Burckhardts and Pacejka equations, and the data they are fitted to.

While Burckhardt could handle the asymmetrical nature of the adhesion for positive and negative slip, it is also seen that the fit for the negative slip is capable of reaching positive values of adhesion with negative slip. This is undesirable as it is not representative of reality. While the Pacejka equation does not take the asymmetric nature of adhesion into account, it is still representative, while also being

easier to implement and is thus chosen for the MATLAB/Simulink model.
The values and what they represent in the Pacejka model are[17],

Name	Symbol	Value
Stiffness Factor	$c_{1,Pacej}$	11.29
Shape Factor	$c_{2,Pacej}$	1.72
Peak Value	$c_{3,Pacej}$	2.42
Curvature Factor	$c_{4,Pacej}$	0.44

The expected road conditions for the AAUER will either be dry or wet tarmac depending on weather conditions on the race track. However, no experimental data from Calspan exists where the same tiers are tested on wet tarmac conditions. Instead, public data from MATLAB[20] will be used to determine a scaling factor between wet and dry tarmac for each coefficient in equation (4.12). Finally the cover letter from Calspan mentions:

> *In past Rounds the "real world" peak lateral and longitudinal forces reported by FSAE teams are roughly 2/3 of those seen at Calspan.*

For this reason, a gain of 2/3 is used to scale the adhesion to a realistic value. This gives a peak value of 1.61 for the adhesion coefficient on dry tarmac.

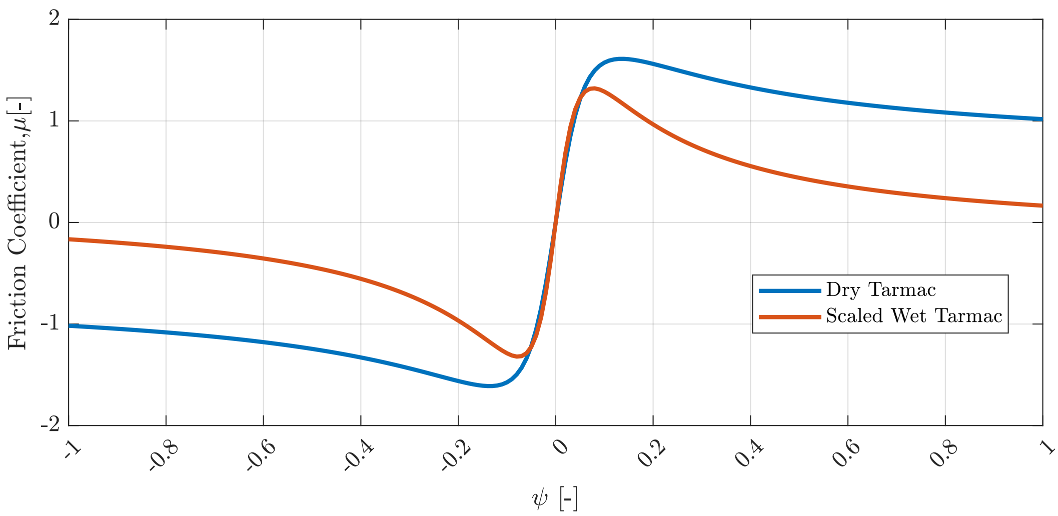

Figure 4.7: Dry and scaled Wet Tarmac adhesion coefficient as a function of slip (ψ)

To demonstrate the car and wheel model, a test scenario is simulated. The equations used to create this test scenario are equations (4.7) and (4.10) and for the adhesion coefficient equation (4.12) with the values given in section 4.1.1. The motor and brake torque are stepped to $600[Nm]$ for $2[s]$ and $1[s]$, respectively. The motor torque step occurs at $1[s]$ and becomes $0[Nm]$ at $3[s]$, the brake torque steps at $7[s]$ and becomes $0[Nm]$ at $8[s]$. The resulting wheel and car speed, motor, and brake torque, slip, and car acceleration is seen in Figure 4.8. When the motor torque increases the wheel accelerates and causes slip to increase. The increase in slip leads to the adhesion coefficient being positive giving the car positive acceleration. similarly, when the braking torque is stepped the slip becomes negative and the car decelerates. When no torque is applied, the friction forces decelerate the car and the wheel.

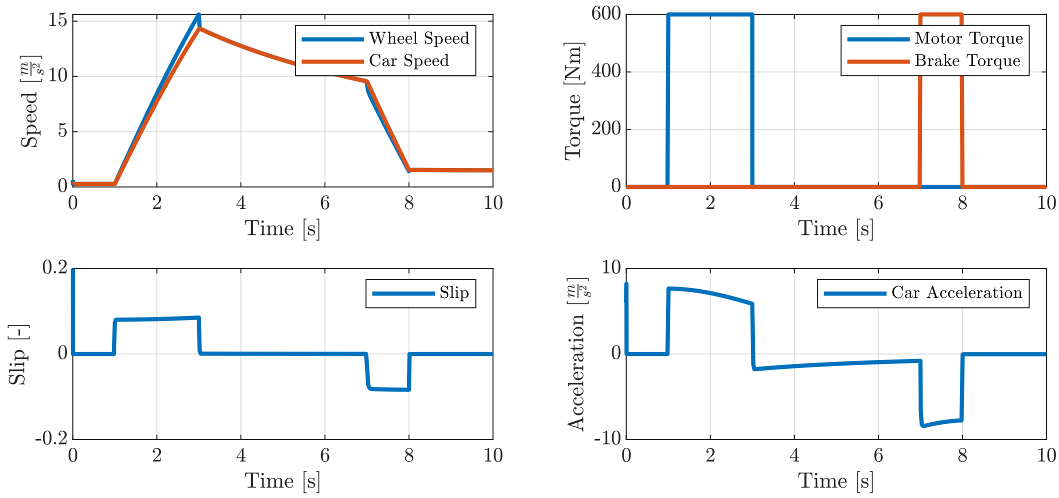

Figure 4.8: Slip, Car acceleration, Motor and Brake torque, and Wheel and Car speed for the testing scenario.

4.2 Electric Model

4.2.1 Space Vector Pulse Width Modulation

The derivation present in this section is inspired from [40]. Space Vector Pulse Width Modulation (SVPWM) is done in the complex plane. This plane is divided into 6 sections, 60° each, by 6 switching vectors. These 6 switching vectors, v_x where $x = 1, 2, 3..$, define a sequence of conducting and non-conducting switches in the inverter. There are an additional 2 zero state vectors for whenever all 3 switches are conducting to positive or negative side only. For a given section in the complex plane, a voltage command in the $\alpha\beta$ frame can then be decomposed into a d_x, d_y, and zero component. This decomposition can be seen in equation equation (4.14).

$$\mathbf{U}_{\alpha\beta} = d_x \cdot \mathbf{v}_1 + d_y \cdot \mathbf{v}_2 \tag{4.13}$$

$$
\begin{aligned}
d_x &= \frac{\sqrt{3}|U_{\alpha\beta}|}{U_{DC}} \frac{2}{3} sin\left(\frac{\pi}{3} - \theta\right) \\
d_y &= \frac{\sqrt{3}|U_{\alpha\beta}|}{U_{DC}} \frac{2}{3} sin(\theta) \\
d_0 &= 1 - d_x - d_y
\end{aligned}
\tag{4.14}
$$

Where d_x and d_y represent the duration which each corresponding switching vector for a given sector needs to be conducting. d_0 is then the remaining zero vector[40].

4.2.2 Battery Package

This section will begin with modeling a battery cell and then scale the cell to a battery pack that fits the requirements of the AAUER. The battery cells in the battery pack will be modeled as a Thevenin equivalent circuit with an additional RC component as shown in Figure 4.9.

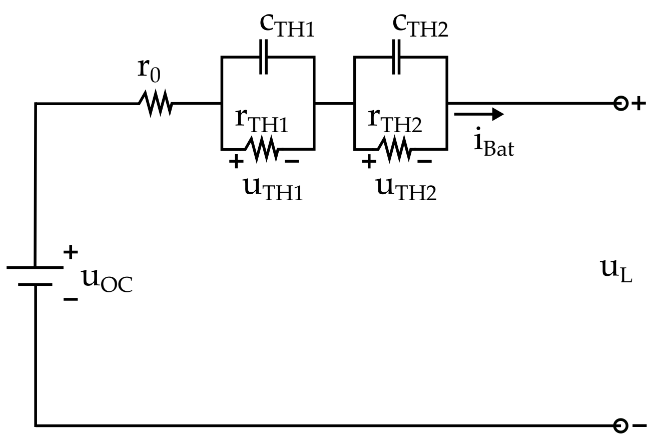

Figure 4.9: Thevenin equivalent circuit with 2 RC of a battery cell

This specific equivalent circuit was chosen due to its high accuracy[36]. r_0 is the internal resistance of the battery, u_{OC} is the open-circuit voltage, $r_{TH,i}$ is the polarization resistance, and $i = 1, 2$ depending on which of the two RC pairs are considered. Polarization is resistance inside the battery due to various electrochemical processes[33]. $c_{TH,i}$ is the equivalent capacitance, this also determines the transient response of the battery during charging and discharging. i_{Bat} is the outflow current of $c_{TH,i}$ [13]. From Kirchhoff's current law it is possible to derive the governing equations for the RC segments of the equivalent circuit are shown in Equation (4.15).

$$
\begin{aligned}
\dot{u}_{TH1} &= -\frac{u_{TH1}}{r_{TH1}c_{TH1}} + \frac{i_{Bat}}{c_{TH1}} \\
\dot{u}_{TH2} &= -\frac{u_{TH2}}{r_{TH2}c_{TH2}} + \frac{i_{Bat}}{c_{TH2}}
\end{aligned}
\tag{4.15}
$$

From Kirchhoff's Voltage law the voltage seen by the load from the battery can be expressed as

$$u_L = u_{OC} - u_{TH1} - u_{TH2} - i_{Bat}r_0 \tag{4.16}$$

defenateli Experimental data has been provided by Erik Schaltz which contains the parameters necessary to complete the battery model. All of the plots for this data can be found in Appendix D. $R_0, R_{TH1}, R_{TH2}, C_{TH1}, C_{TH2}$ and u_{OC} are all dependent on the SoC of the battery pack. To accommodate this a lookup table has been implemented for each variable. The only thing which remains is calculating the SoC of the battery pack. As mentioned in section 2.1.2, one possibility is Coulomb counting. This will serve as a good, easy-to-implement solution to determining the SoC. Combining equation equation (4.16) and all SoC dependent parameters a dynamic model of a battery cell is realized. The visualization of the Simulink implementation can be seen in figure 4.10

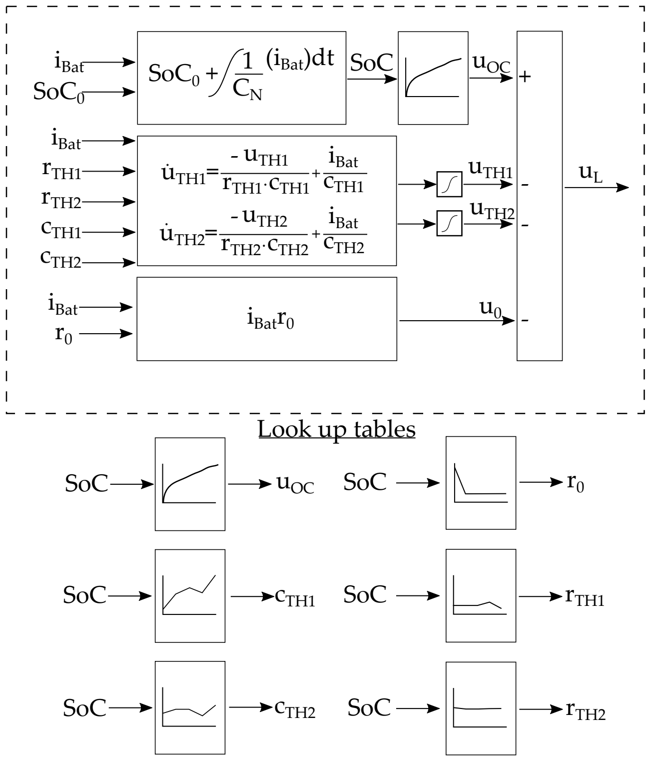

Figure 4.10: Illustration of the simulink structure for the battery cell

Verification of the battery pack

To verify the equivalent circuit model comparison will be made between the model and experimental data obtained from a Worldwide Harmonized Light Vehicle Test Procedure(WLTP) test. An offset was removed between the battery model and the laboratory data, the reason being that the initial SoC between the experimental data and the battery model could be different. The offset was equal to $0.2311[V]$.

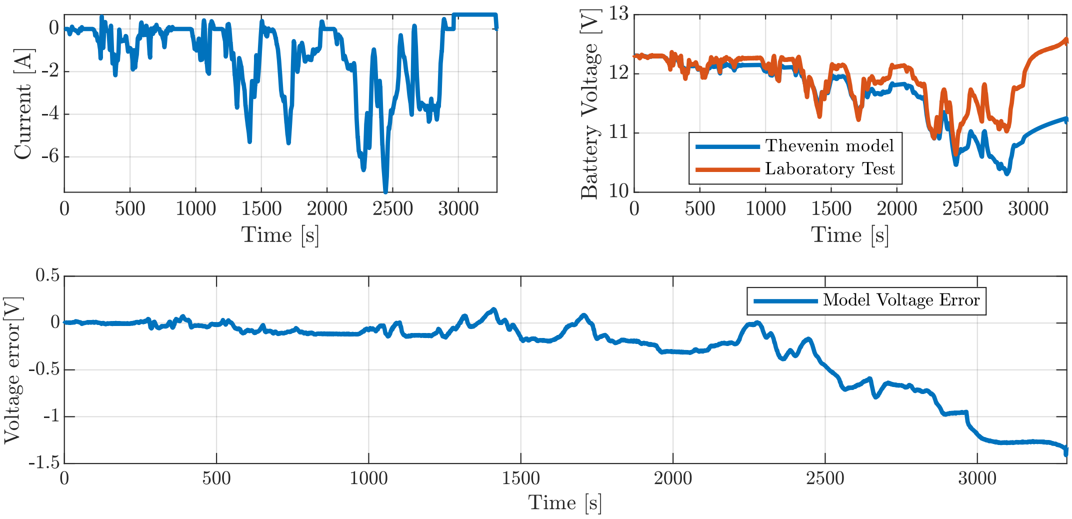

Figure 4.11: Battery voltage of the Thevenin model and the laboratory measurements, as well as the current going into the battery.

It is seen that the Thevenin model reacts similarly to the input current. However, it is also seen that the OCV of the model deviates as time goes by. The battery model finds the SoC via the coulomb counting method which is known to drift over time, thus the increasing error in OCV is believed to be caused by the coulomb counting.

Cell to battery pack

The battery cell needs to be properly scaled such that it can provide the desired voltage and have a sufficiently large capacity. Given the equivalent circuit of a single cell in figure 4.9 and the required amount of energy needed to complete the endurance race as calculated in section 2.1.1. Furthermore, when considering the design of the battery pack not only the pack must fulfill the requirements set by the AAUER itself but also the regulations set by FSAE as mentioned in section 3.2. The batteries used for the AAUER will be the Samsung INR18650-35E [29]. A single cell has the specifications shown in Appendix chapter A.
In the FSAE ruleset the battery pack is required to be divided into segments [10][EV5.3.2], however, for simplicity battery segment design will not be considered in this scaling process. Instead, the entire pack will be designed as a whole.

Firstly, the number of cells in series needed to meet the load voltage requirement will be calculated, and then the number of parallel connections to meet capacity requirements. The battery pack must not exceed $600[V]$ DC [10][EV4.1.1] thus,

$$\begin{aligned} N_{series} &= \frac{U_{limit}}{U_{max}} = \frac{600}{4.2} \approx 142 \\ U_{pack} &= N_{series} \cdot U_c = 142 \cdot 4.2[V] = 596.4V \end{aligned} \tag{4.17}$$

To increase the capacity of the battery pack, the individual cells are connected in parallel. With N_{series} series-connected cells a load voltage of $596.4[V]$ is seen at the output terminals of the battery pack. The equation for the capacity of all the cells in series is seen in equation (4.18) [35, pp. 40–41].

$$\begin{aligned} Q_{series} &= N_{series} U_{max} Q_{bat} \cdot 3600 \\ Q_{series} &= 142 \cdot 4.2[V] \cdot 3.4[Ah] \cdot 3600 \approx 6.25MJ \end{aligned} \tag{4.18}$$

Thus, the total amount of parallel connections required to contain enough energy for the entirety of the endurance race is,

$$N_{parallel} = \frac{Q_{total}}{Q_{cell}} = \frac{50.7[MJ]}{6.25[MJ]} \approx 9 \tag{4.19}$$

The battery pack will contain 142 series-connected and 9 parallel connected cells such that it can meet both voltage and capacity requirements set by the AAUER and the FSAE.
How the battery pack is implemented in Simulink is done via scaling the existing cell as shown in figure 4.10 up to have equivalent cell parameters to that of a battery pack with 142 series connections and 9 parallel connections. For $r_0, r_{TH1}, r_{TH2}, c_{TH1}, c_{TH2}$ this involves summing the parallel and series resistance/capacitance. The new OCV is calculated by multiplying the output of the OCV lookup table by the number of series-connected cells. Finally, the capacity of the battery needs to be recalculated based on the new battery pack parameters.

4.2.3 Voltage Source Inverter

The SVPWM will output 3 duty cycles which will then be supplied to the 3-phase Voltage Source Inverter(VSI).

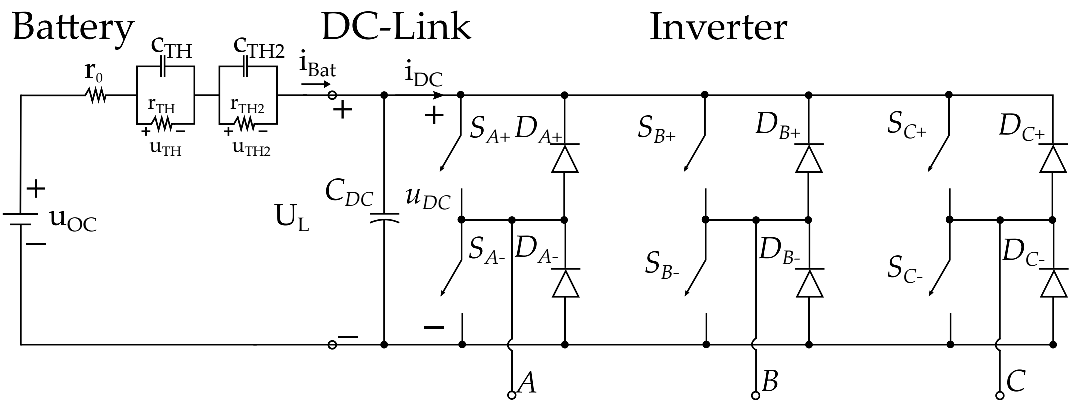

Figure 4.12: Battery, DC-Link and inverter illustration

The switching frequency of the VSI should be larger than the fundamental frequency of the inverter output. That is, the frequency modulation ratio, m_f, should be as high as possible. Nonlinearities such as dead time will not be considered in the controller design but will be present in the final simulations[15]. Dead time is an additional time delay introduced every switching instance in order to make sure that the both switches in one of the inverter legs do not conduct at the same time[22].

The derivations presented in this section are based on the work presented in [18, pp. 551–553] for the DC-link and [11] for the average model of the voltage error caused by dead-time in the inverter. ˆ represents an average value of a dynamic variable.

$$\frac{d}{dt}\hat{u}_{DC} = \frac{\hat{i}_{Bat} - \hat{i}_{DC}}{C_{DC}} \tag{4.20}$$

The current entering the inverter can be approximated to equation (4.21) [18, p. 553].

$$\begin{aligned} \hat{i}_{DC} &= \frac{3}{2}\frac{\hat{u}_q\hat{i}_q + \hat{u}_d\hat{i}_d}{\hat{u}_{DC}} \\ \hat{u}_q &= \hat{u}_{DC} m \cdot cos(\phi),\ \hat{u}_d = \hat{u}_{DC} m \cdot sin(\phi), \\ m &= \frac{\mid U_{dq} \mid}{\hat{u}_{DC}},\ \phi = \angle(u_d + ju_q) \end{aligned} \tag{4.21}$$

$$i_{DC} = \frac{3}{2} m(\hat{i}_q cos(\phi) - \hat{i}_d sin(\phi)) \tag{4.22}$$

Modulation index can be calculated as shown in equation (4.21) since the modulation technique used is SVM. With equations (4.20) and (4.21) it is possible to describe the dynamics of the DC-link.

Including dead-time in average inverter model generates a voltage error which needs to be accounted for. The actual output of the inverter is a combination of the ideal voltage commanded by the controller and then voltage error calculated by the average model, as seen in equation (4.23).

$$u_{actual} = u_{ideal} + u_{error} \tag{4.23}$$

The ideal voltage output of the inverter is calculated from the dq-frame voltage commands given to the inverter from the controller. Using SVM and transforming the rotating dq-frame to the stationary $\alpha\beta$-frame using the Clarke transform [18, p. 98] it is possible to calculate the modulation index using equation (4.24).

$$m = \frac{\mid u_{\alpha\beta} \mid}{u_{DC}} \tag{4.24}$$

With the corresponding modulation index it is then possible to calculate the corresponding $\alpha\beta$ voltage phasor using the same relation in equation (4.24)

$$u_{\alpha\beta,ideal} = m \cdot u_{DC} \tag{4.25}$$

The corresponding ideal $\alpha\beta$ voltage commands are transformed into the dq-frame using equation (4.26).

$$u_{dq,ideal} = \begin{bmatrix} cos(\theta) & sin(\theta) \\ -sin(\theta) & cos(\theta) \end{bmatrix} \begin{bmatrix} u_{\alpha,ideal} \\ u_{\beta,ideal} \end{bmatrix} \tag{4.26}$$

All that remains now is to determine the corresponding average voltage error. The average voltage error is caused by dead time in the switches which can be expressed as,

$$u_{error} = u_{DC} \frac{t_{delay}}{T_{sample}} \tag{4.27}$$

Where t_d is the dead time between two switches, T_s is the time period of the switching instances. The magnitude of equation (4.27) remains constant, however, the location of the voltage error phasor in the space vector domain changes as a function of the current polarities as seen in Figure 4.13.

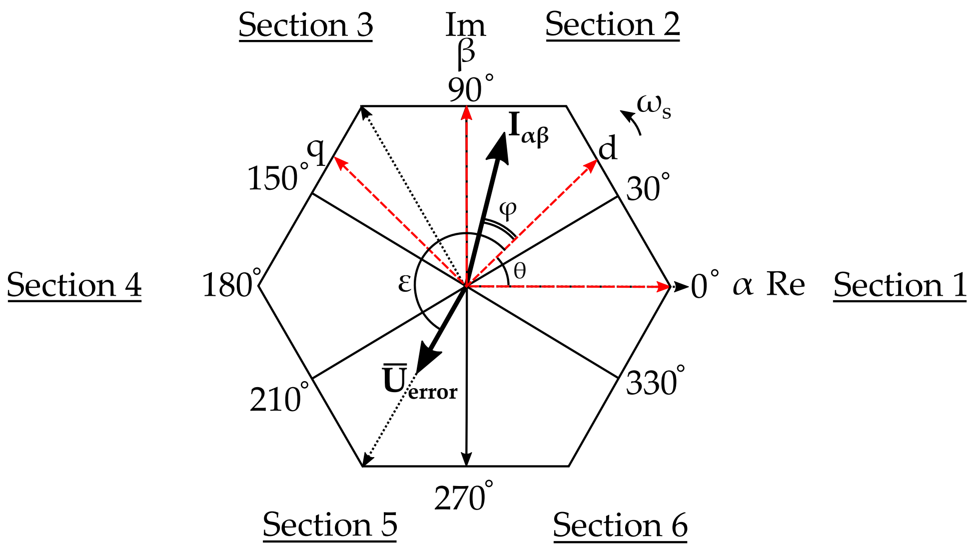

Figure 4.13: Space vector representation of the voltage error phase and the corresponding $\alpha\beta$ current phasor. Both the stationary $\alpha\beta$ frame and the rotating dq-frame can be seen in the diagram. This diagram is inspired from [11]

ϕ is the angle of the current phasor with respect to the dq-frame. Thus, the first step in determining the location of the voltage error phasor is to determine the location of the current phasor. I_{dq} can be directly measured from the output of the PMSM, applying the Clarke Transform to the stationary $\alpha\beta$-frame as seen in equation (4.28).

$$i_{\alpha\beta} = \begin{bmatrix} cos(\theta) & -sin(\theta) \\ sin(\theta) & cos(\theta) \end{bmatrix} \begin{bmatrix} i_d \\ i_q \end{bmatrix} \tag{4.28}$$

The angle of the current phasor in the $\alpha\beta$ frame can then be obtained from equation (4.29).

$$\phi = \angle i_{\alpha\beta} = \angle(i_\alpha + j i_\beta) \tag{4.29}$$

The voltage error phasor moves in discrete steps from sector to sector in Figure 4.13 depending on the polarities of the current. Table 4.1 summarizes the results of the movement of U_{error} with a varying current polarity.

Sector #	sign of			U_{error}	range of a sector	ϵ
	i_a	i_b	i_c			
1	+	-	-	$\frac{4}{3}u_{error}$	$-30° < (\phi+\theta) < 30°$	$180° - \theta$
2	+	+	-	$\frac{4}{3}u_{error}$	$30° < (\phi+\theta) < 90°$	$240° - \theta$
3	-	+	-	$\frac{4}{3}u_{error}$	$90° < (\phi+\theta) < 150°$	$300° - \theta$
4	-	+	+	$\frac{4}{3}u_{error}$	$150° < (\phi+\theta) < 210°$	$0° - \theta$
5	-	-	+	$\frac{4}{3}u_{error}$	$210° < (\phi+\theta) < 270°$	$60° - \theta$
6	+	-	+	$\frac{4}{3}u_{error}$	$270° < (\phi+\theta) < 330°$	$120° - \theta$

Table 4.1: From [11] illustrating change of the angle of U_{error} depending on the current polarities and the associated magnitude of U_{error}.

Where θ is the angle between α in the $\alpha\beta$-frame and the rotating d-axis in the dq-frame. Knowing the angle of the current phasor, ϕ, it is then possible to determine the section in which the current phasor is located and as a result, the corresponding section which U_{error} is. Given the discrete nature of u_{error}, angle of U_{error} as seen in table 4.1 and the angle of the dq-frame , θ. It is then possible to project U_{error} to the dq-frame as seen in equation (4.30).

$$\begin{bmatrix} u_{d,error} \\ u_{q,error} \end{bmatrix} = \begin{bmatrix} \frac{4}{3}u_{error}cos(\epsilon-\theta) \\ \frac{4}{3}u_{error}sin(\epsilon-\theta) \end{bmatrix} \tag{4.30}$$

With equations (4.23), (4.26) and (4.30) the average inverter model with voltage error due to dead time can be implemented. With the implementation of the average inverter model the general behaviour of the inverter is still accounted for without the need to implement actual switches in the inverter model.

4.2.4 PMSM

To simplify the derivations of the PMSM, the winding configuration of the PMSM is assumed to be Distributed Windings (DW). This means that the Magnetic Motive Force(MMF) of the PMSM will be approximately sinusoidal. Thus, making it possible to use the standard equations for the PMSM in the dq0-frame[6, pp. 3, 14]. The voltage equations for the PMSM can be seen in equation (4.31).

$$\begin{aligned} u_q &= R_s i_q + \frac{d}{dt}\lambda_q + \omega_e\lambda_d \\ u_d &= R_s i_d + \frac{d}{dt}\lambda_d - \omega_e\lambda_q \end{aligned} \tag{4.31}$$

Where,

$$\begin{aligned} \lambda_q &= i_q L_q \\ \lambda_d &= i_d L_d + \lambda_{mpm} \end{aligned} \tag{4.32}$$

R_s is the stator resistance, ω_r is the angular velocity of the the rotor, and λ_{mpm} is the flux linkage of the permanent magnet. Combining equation (4.31), equation (4.32) and solving for i_q and i_d individually yields the dynamic current equations as seen in equation (4.33),

$$\begin{aligned} \frac{d}{dt}i_d &= \frac{1}{L_d}(u_d - Ri_d + \omega_r\lambda_q) \\ \frac{d}{dt}i_q &= \frac{1}{L_q}(u_q - Ri_q - \omega_r\lambda_d) \end{aligned} \tag{4.33}$$

With equation (4.33) i_q and i_d dynamics can be described inside the PMSM.

4.3 System Model

Figure 4.14 is an illustration of the fundamental Simulink model which all controllers designed in chapter 5 will be implemented with. The content of figure 4.14 is all of the different components described in this chapter.

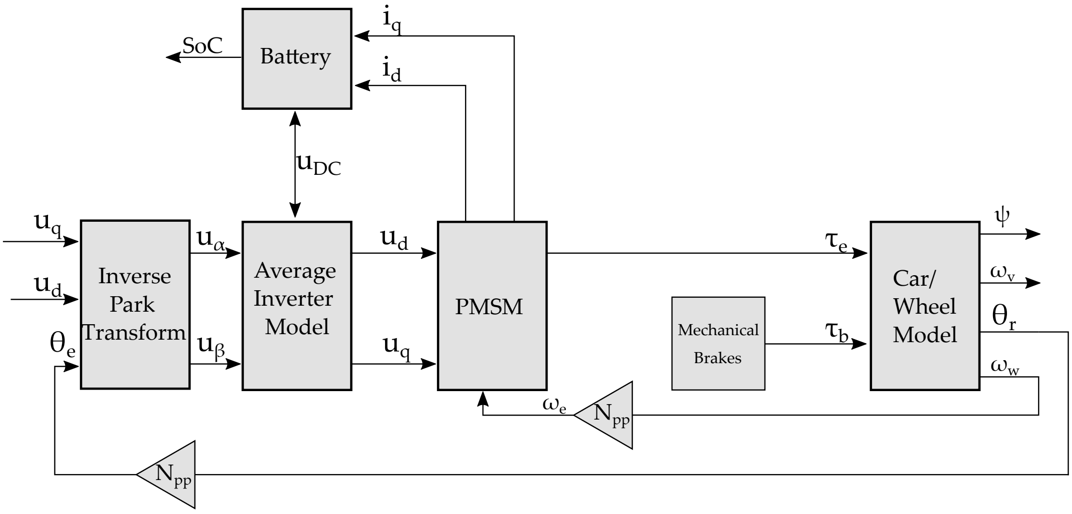

Figure 4.14: Illustration of the fundamental Matlab Simulink for the AAUER.

Chapter 5

Control Strategies

This chapter serves to explain and derive all of the different control strategies and estimation methods that will be tested on the model described in Chapter 4. Demonstrations of the control methods are shown through the chapter, but with simplified models for simplicity's sake.

5.1 Control Structure

The control structure used for both the motor control and extended motor control will be implemented in a cascade-like typology. Extended motor control is additional control that is implemented on top of the motor control. For example, slip control or regenerative braking. For the real-life AAUER the speed loop does not exist. Instead, a speed pedal will be present which will provide the current control with a given reference. That means that additional design considerations need to be made when designing each loop. Specifically, the inner loop, current control, needs to have a dominating pole that is faster than that of the slip control and the speed controller. The Slip controller needs to be faster than the speed loop but slower than the current loop and so forth. This general idea is illustrated in Figure 5.1.

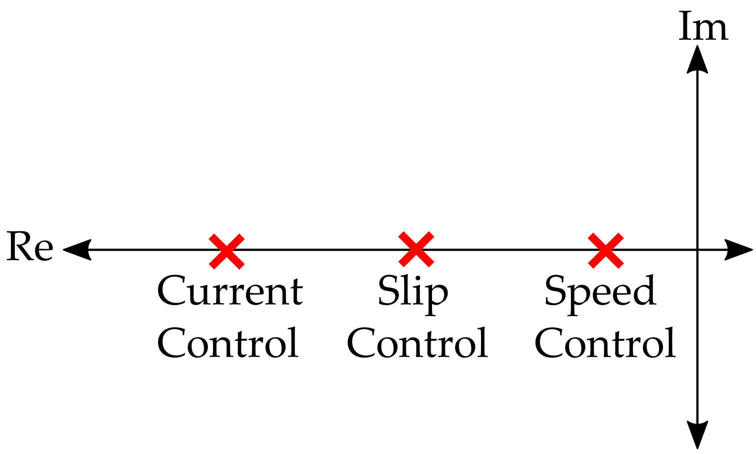

Figure 5.1: Illustration of the general structure of the cascade control loops and the placement of their respective dominating poles when designing the cascade loops.

5.2 Emulation

All controller designed presented in this section is done in the continuous-time domain but is implemented in the MATLAB Simulink model described in figure 4.14 in the discrete domain. This is an appropriate approximation as long as the Bilinear Approximation is upheld. That is, as long as the bandwidth of the controller design is at least 20 times lower than the sampling frequency[24, pp. 622–623]. The sampling frequency is chosen to be $10[kHz]$ as a result.

5.2.1 Field Oriented Control

Current Loop

The PI controller for the inner current loop is designed first. The current controllers used for i_d and i_q are identical, and as such only the design of the i_d controller will be shown. As the q-axis current is the only torque-producing current, for FOC, it would be undesirable to have a large overshoot. Since a significant enough overshoot could result in a torque high enough to make the rear wheels lose traction due to an increase in slip. Furthermore, it will increase the strain on the inverter or battery in case of excessively high currents. For this reason, the current controllers are designed to have a 1.5% overshoot. The transfer function is equivalent to that of an RL circuit with a back-emf term. From equation (4.33) it can be seen there exists a coupling between i_d and i_q, to counteract this unwanted coupling back-emf decoupling is implemented. The back-emf is canceled via back-emf decoupling in the PI, which makes the transfer function an RL circuit. A block diagram of the back-EMF decoupling is showing in Figure 5.2.

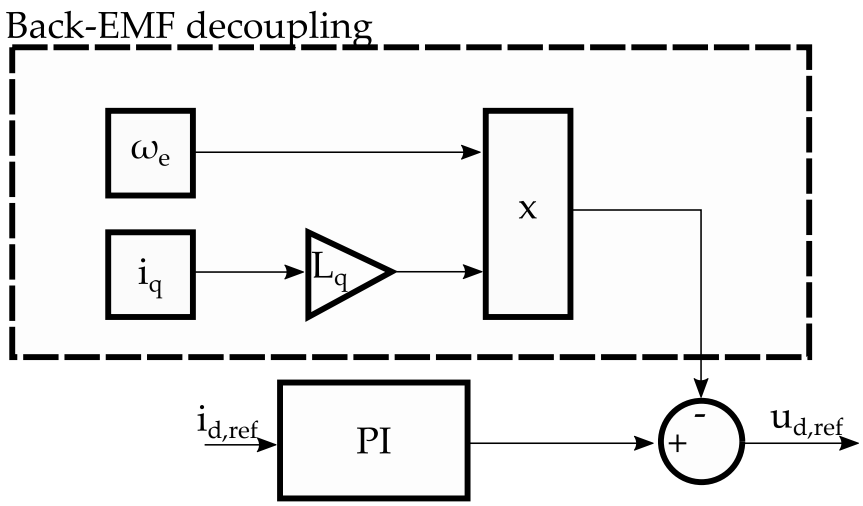

Figure 5.2: Block diagram of how the back-EMF decoupling is implemented in simulink.

An ideal time delay is also included to account for the inverter not responding immediately[37]. The delay transfer function has a time constant equal to 1.5 times the switching frequency. The three transfer functions, in an open loop, then become:

$$G_{RL,open} = \frac{i_d}{i_{d,ref}} = \underbrace{\frac{1}{sL_d + R_s}}_{RL\ circuit} \underbrace{\frac{1}{st_0 + 1}}_{delay} \underbrace{\frac{sk_{RL,P} + k_{RL,I}}{s}}_{PI} \tag{5.1}$$

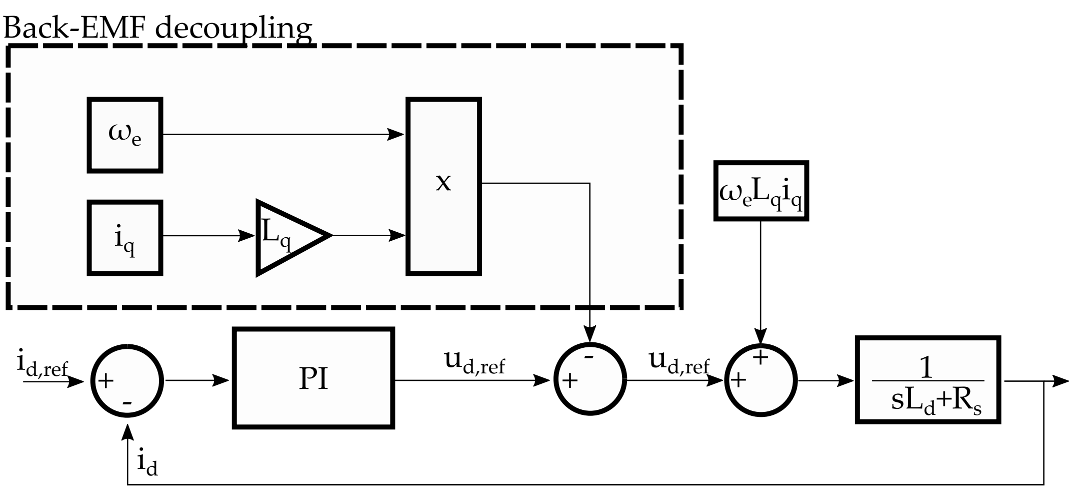

Figure 5.3: Block diagram of the closed loop current control for i_d

The complete closed loop current control can be seen in figure 5.3

$$G_{RL,closed} = \frac{k_{RL,I}}{L_d t_0} \frac{s + \frac{k_{RL,I}}{k_{RL,P}}}{s(s + \frac{R_s}{L_q})(s + \frac{1}{t_0})} \tag{5.2}$$

Where t_0 is the time constant introduced by the inverter. By deriving the closed-loop transfer function it is seen that $k_{RL,I}$ can be chosen as $k_{RL,I} = k_{RL,P}\frac{R_s}{L_q}$ in order to cancel the pole located at $-\frac{R_s}{L_q}$. This simplifies the closed-loop system to a second-order system.

$$G_{RL,closed} = \frac{i_d}{i_{d,ref}} = \frac{\frac{k_{RL,P}}{L_q t_0}}{s^2 + \frac{1}{t_0}s + \frac{k_{RL,P}}{L_d t_0}} = k\frac{\omega_n^2}{s^2 + 2\zeta\omega_n s + \omega_n^2} \tag{5.3}$$

The value of $k_{RL,P}$ is then calculated to get an overshoot of 1.5%[24, p. 149].

$$\begin{aligned} O &= 1.5\% \\ \zeta = cos\left(tan^{-1}\left(\frac{-\pi}{ln(O/100)}\right)\right) &= 0.80 \\ \omega_n = \frac{1}{2\zeta t_0} &= 4162.77\,\frac{rad}{s} \\ k_{RL,P} = w_n^2 L_q t_0 &= 0.47 \\ k_{RL,I} = k_{RL,P}\frac{R_s}{L_d} &= 43.40 \end{aligned} \tag{5.4}$$

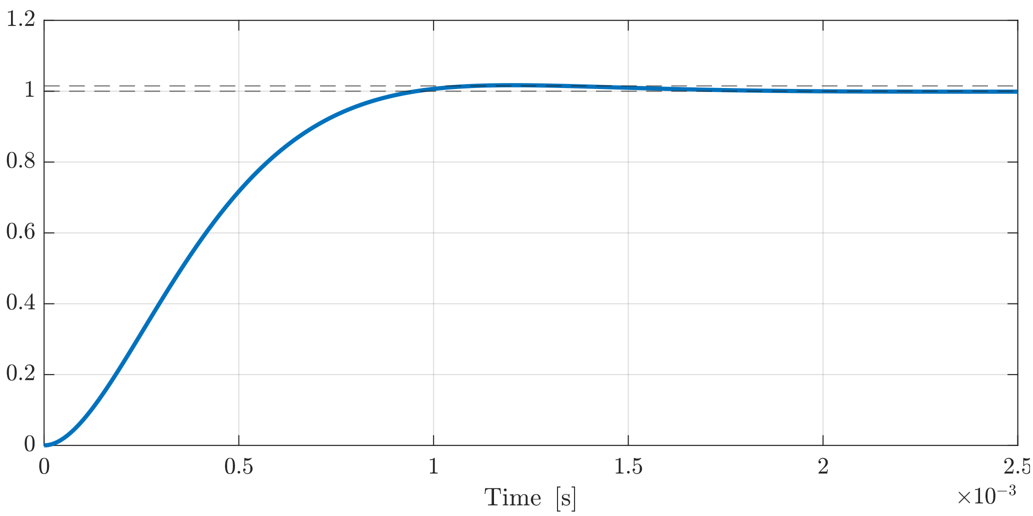

Figure 5.4: Step response of the i_d current controller.

As can be seen from Figure 5.4 the overshoot is exactly 1.5% and as such the current controller performs as designed.

Speed Loop

With a fully designed current controller, the speed controller is designed. The same arguments from the current controllers can be made for the speed controller. An overshoot in wheel speed will result in a temporary increase in slip which potentially could decrease the adhesion of the wheel, making it slide. The wheel speed controller is thus designed to have no overshoot. The wheel equation is restated here for convenience as stated in chapter 4.

$$\dot{\omega}_w J_w = \tau_{em} - \tau_b - R_w F_T - R_w F_{visc} \tag{5.5}$$

$$\dot{\omega}_w J_w = \tau_{em} - R_w \mu(\psi) N_v - R_w B_v v \tag{5.6}$$

The term related to the adhesion forces in equation (5.6), are treated as disturbance and are neglected when deriving the transfer function. While there are separate terms for the braking and accelerating torque, they will be combined into one term for simplicity. The transfer function for the wheel then becomes that of a rotating mass with friction.

$$G_{wheel}(s) = \frac{\omega_w}{\tau_{em}} = \frac{1}{J_w s + R_w B_v} \tag{5.7}$$

As the speed loop shares a similar block diagram with a cascade compensator, it would be prudent to include the effects of the current loop when designing the PI for the speed loop. The current loop effects on the speed loop will be approximated with an ideal time delay similar to that used in the current loop design. The time constant will be equal to the dominating pole of the current loop and with a gain equal to the motor constant k_t. The current loop is a second-order system with a dampening ratio of 0.80, it will have two poles which are complex conjugates, but has the same time constant $\frac{1}{\zeta\omega_n}$. From Equation (5.4) the time constant is found to be $\tau_d = 3.0 \cdot 10^{-4}$ and the transfer function is then given by:

$$G_{current} = \frac{k_t}{s\tau_{delay} + 1} \tag{5.8}$$

combining the transfer functions of Equation (5.7), Equation (5.8) and a PI then gives the block diagram seen in Figure 5.5

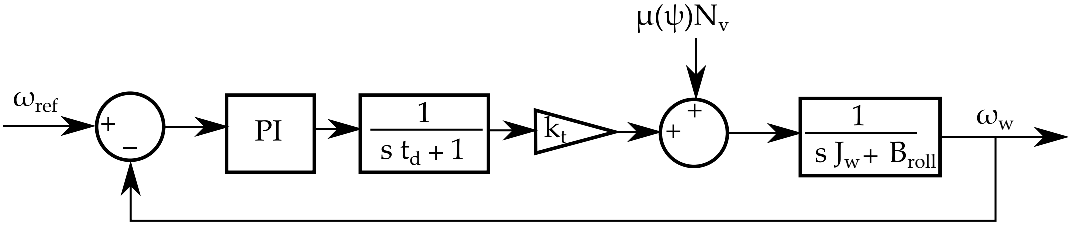

Figure 5.5: speed loop block diagram for the wheel transfer function.

Since the disturbance of the adhesion forces should be rejected, the block diagram is rearranged to have the adhesion force as input as seen in Figure 5.6

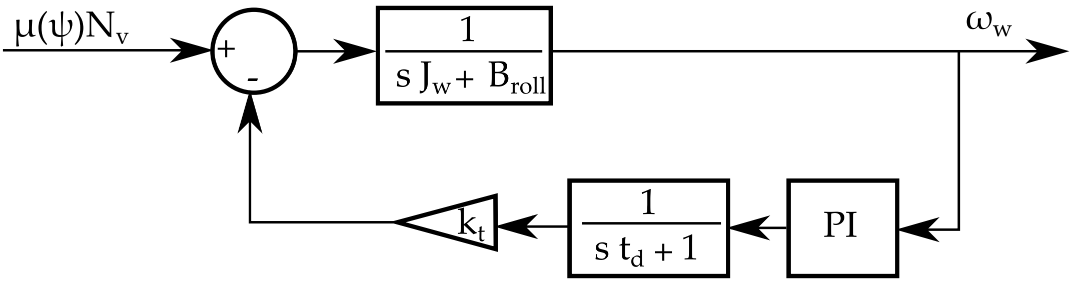

Figure 5.6: block diagram with the adhesion force as input and wheel speed as output

the closed loop transfer function for the disturbance is then given as:

$$
\begin{aligned}
G_{dist}(s) = \frac{\omega_w}{\mu(\psi)N_v} &= \frac{\frac{1}{SJ_wB_{visc}}}{1+\frac{k_{JB,P}+k_{JB,I}}{s}\frac{k_t}{t_{delay}s+1}\frac{1}{sJ_w+B_{visc}}} \\
&= \frac{\frac{s(st_d+1)}{J_wt_{delay}}}{s^3+\frac{B_{visc}t_{delay}+J_w}{J_wtdelay}s^2+\frac{k_{JB,P}k_t+B_{visc}}{J_wt_{delay}}s+\frac{k_{JB,I}k_t}{J_wt_d}}
\end{aligned}
\tag{5.9}
$$

The characteristic equation is that of a third-order system, i.e. it will have three poles. Equating the characteristic equation to that of a third-order polynomial and choosing the location of two of them, it is possible to do a comparison of coefficients for the PI gains.

$$
\begin{aligned}
s^3 + \frac{B_{visc}t_{delay} + J_w}{J_w t_{delay}} s^2 + \frac{k_{JB,P}k_t + B_{visc}}{J_w t_{delay}} s + \frac{k_{JB,Ik_t}}{J_w t_{delay}} &= (s+p_1)(s+p_2)(s+p_3) \\
\frac{B_{visc}t_{delay} + J_w}{J_w t_{delay}} &= p_1 + p_2 + p_3 \\
\frac{k_{JB,P}k_t + B_{visc}}{J_w t_{delay}} &= (p_1 p_2 + p_1 p_3 + p_2 p_3) \\
\frac{k_{JB,Ik_t}}{J_w t_{delay}} &= p_1 p_2 p_3
\end{aligned}
\tag{5.10}
$$

It is decided to place two poles at 169.41 which has a time constant 25 times higher than that of the current loop. This placement is done to avoid the speed controller being so fast that the inverter would become a dominating factor, while still having controller dynamics significantly faster than the wheel and car.

$$
\begin{aligned}
p_1 = p_2 &= 169.41 \\
\frac{B_{visc}t_{delay} + J_w}{J_w} - p_1 - p_2 = p_3 &= 3896.40 \\
k_{JB,P} = \frac{(p_1 p_2 + p_1 p_3 + p_2 p_3) J_w t_d - B_v}{k_t} &= 263.34 \\
k_{JB,I} = \frac{p_1 p_2 p_3 J_w t_{delay}}{k_t} &= 21835
\end{aligned}
\tag{5.11}
$$

The PI controllers are then implemented in the MATLAB Simulink model as described in figure 4.14, which contains the car and wheel as well as the PMSM. Wheel speed reference is started at $1\left[\frac{m}{s}\right]$, when $1[s]$ has passed, the speed reference steps to $10\left[\frac{m}{s}\right]$. 5.7 shows the i_q and i_d currents and wheel speed as well as their respective references and error.

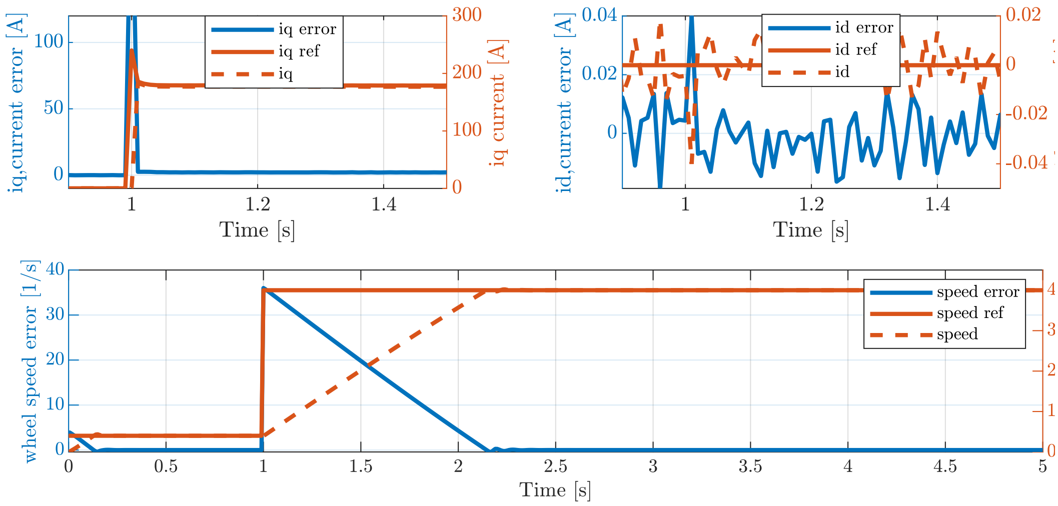

Figure 5.7: Simulation results using the MATLAB Simulink model described in figure 4.14 showing the i_q and i_q currents as well as the wheel speed with their respective references and errors.

From 5.7 it is seen that the i_q current starts with a value different from 0, as the wheel speed starts at a 0. At $1[s]$ the speed reference changes which increases i_q current. The i_d current should be kept at 0 at all times when using FOC control. It is seen that the i_d current is different from 0 when the speed reference changes, which is to be expected as the PMSM back-emf will disturb the i_d PI controller.

5.2.2 Maximum Torque Per Ampere

In FOC the i_d PI has a constant reference of 0, however, this does not utilize the reluctance torque of the EMRAX PMSM. From the PMSM torque equation, restated in 5.12 for convenience, it can be seen that if the i_d current is negative while the i_q is positive, the second term in the equation will contribute positively to the overall torque.

$$\tau_{em} = \frac{3}{2} N_{pp}((L_d - L_q)i_d i_q + \lambda_{mpm} i_q) \tag{5.12}$$

Since the current phase has a limited magnitude there exists an optimal i_q and i_q which produces the highest possible torque. Rewriting equation (5.12) to depend on the maximum stator current I_s with the relations shown in figure 5.8

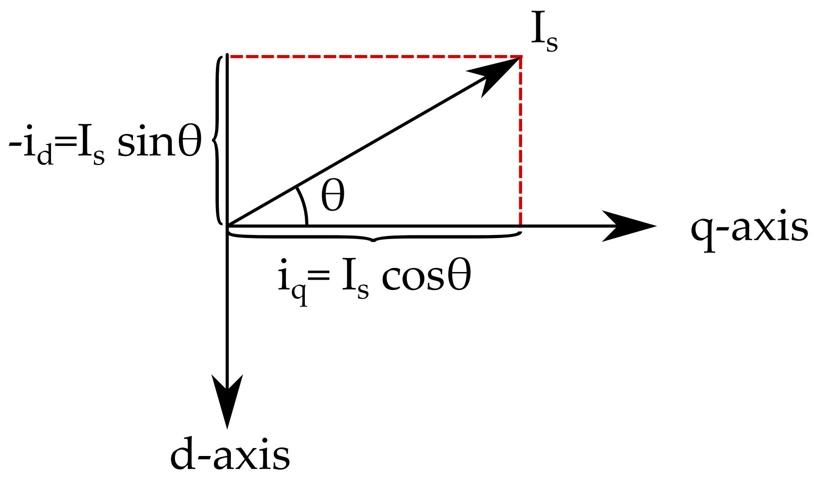

Figure 5.8: relation between the I_s and i_d, i_d currents.

$$\tau_{em} = \frac{3}{2}N_{pp}((L_d - L_q)I_s sin(\theta)I_s cos(\theta) + \lambda_{mpm}I_s cos(\theta)) \tag{5.13}$$

$$\tau_{em} = \frac{3}{2}N_{pp}((L_d - L_q)I_s^2 \underbrace{sin(\theta)cos(\theta)}_{\frac{1}{2}sin(2\theta)} + \lambda_{mpm}I_s cos(\theta)) \tag{5.14}$$

$$\tau_{em} = \frac{3}{2}N_{pp}((L_d - L_q)I_s^2 \frac{1}{2}sin(2\theta) + \lambda_{mpm}I_s cos(\theta)) \tag{5.15}$$

As the torque now only depends on the angle θ of I_s the optimal criteria can be written as

$$\frac{\partial \tau_{em}}{\partial \theta} = -(L_d - L_q)I_s^2 \underbrace{cos(2\theta)}_{cos^2(\theta) - sin^2(\theta)} - \lambda_{mpm}I_s sin(\theta) = 0 \tag{5.16}$$

Replacing $cos(2\theta)$ with a trigonometric identity gives

$$\frac{\partial \tau_{em}}{\partial \theta} = -(L_d - L_q)I_s^2(cos^2(\theta) - sin^2(\theta)) - \lambda_{mpm}I_s sin(\theta) = 0 \tag{5.17}$$

Here the expressions for i_d and i_q are identified and replaced

$$\frac{\partial \tau_{em}}{\partial \theta} = -(L_d - L_q)(\underbrace{I_s^2 cos^2(\theta)}_{i_q^2} - \underbrace{I_s^2 sin^2(\theta)}_{i_d^2}) - \lambda_{mpm}\underbrace{I_s sin(\theta)}_{i_d} = 0 \tag{5.18}$$

Simplifying and rearranging the equation

$$\frac{\partial \tau_{em}}{\partial \theta} = -(L_d - L_q)(i_q^2 - i_d^2) + \lambda_{mpm} i_d = 0 \tag{5.19}$$

$$\frac{\partial \tau_{em}}{\partial \theta} = -(L_d - L_q)i_q^2 + (L_d - L_q)i_d^2 + \lambda_{mpm} i_d = 0 \tag{5.20}$$

$$\frac{\partial \tau_{em}}{\partial \theta} = i_d^2 + \frac{\lambda_{mpm}}{(L_d - L_q)} i_d - i_q^2 = 0 \tag{5.21}$$

Equation (5.21) is seen to be a second order polynomial with the solution being:

$$\begin{gathered} A = 1,\ B = \frac{\lambda_{mpm}}{(L_d - L_q)},\ C = -i_q^2 \\ i_d = \frac{-\frac{\lambda_{mpm}}{(L_d - L_q)} \pm \sqrt{\left(\frac{\lambda_{mpm}}{(L_d - L_q)}\right)^2 + 4i_q^2}}{2} \end{gathered} \tag{5.22}$$

Since only a negative i_d with positive i_q produces a net positive torque, only the negative solution is of interest, thus

$$i_d = \frac{-\frac{\lambda_{mpm}}{(L_d - L_q)} - \sqrt{\left(\frac{\lambda_{mpm}}{(L_d - L_q)}\right)^2 + 4i_q^2}}{2} \tag{5.23}$$

From 5.23 it is seen that the i_d current should only change with i_q, if the motor parameters are assumed constant. 5.23 is then used with the same PI controller, but now the i_d reference changes with i_q.

The test used to get the results in Figure 5.7 is reused to demonstrate the difference in i_q and i_d current and the current magnitude. The resulting currents are shown in Figure 5.9 with the current magnitude being $|i_s| = \sqrt{i_q^2 + i_d^2}$ and difference calculated as $I_{diff} = I_{FOC} - I_{MTPA}$.

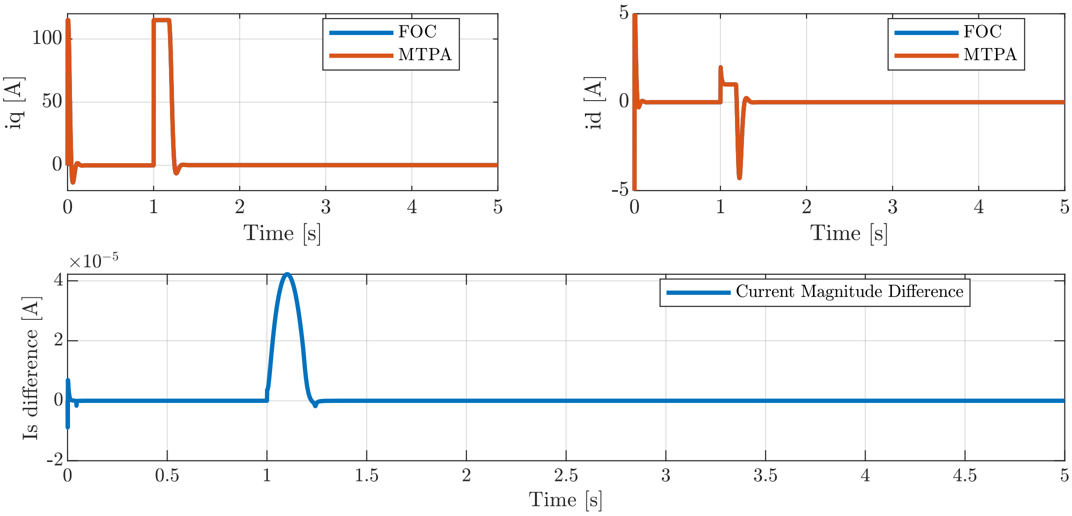

Figure 5.9: Comparison of i_q and i_d currents using FOC and MTPA.

From Figure 5.9 it is seen that the current magnitude difference between FOC and MTPA is small. This is expected as the saliency of the EMRAX 228 is 0.96. The speed reference is stepped at $1[s]$ the i_q current increases but the magnitude is smaller for the MTPA implementation, which is expected.

5.3 Extended Motor Control

Extended motor control is considered an extension of the base motor control, FoC, or MTPA. With the intent to enhance the performance of the AAUER. In this case, extended motor control refers to control of the slip. The reason why slip control is of significant importance is due to the section 4.1.1. Since there exists a point on the adhesion curve where the adhesion coefficient is the highest. The reason why this is favorable can be seen in equation (4.6) since a higher adhesion coefficient value will result in a higher tractive force, which will accelerate the AAUER faster.

5.3.1 Linear Slip Control

The design procedure and stability analysis of the linear controller for ABS is inspired from [30][25-26,31-42,55-62] and then applied similarly to the TC. Before the system of equations is linearized and a transfer function is derived, it is important to consider the properties of the system and how their equilibrium points behave to get a better understanding of how to design the controller properly. The slip controller is divide into two sections. The first analyses the properties of the system, while the second part is concerned with controller design and analysis. Equation equation (5.24) and equation (5.25) show the system of equations for the different slip modes. TC is active when the car accelerates and when the car brakes ABS is active. When discussing theory relevant to both TC and ABS the two control methods will be referred to as slip controllers.

Investigation of equilibrium points

Traction Control

$$\begin{aligned} \psi_{TC} &= \frac{\omega_w R_w - v}{\omega_w R_w} \\ \dot{\omega}_w &= \frac{R_w N_v \mu(\psi) + \tau_{em}}{J_w} \\ \dot{v} &= \frac{N_v \mu(\psi)}{M_v} \end{aligned} \tag{5.24}$$

Antilock-Brake System

$$\begin{aligned} \psi_{ABS} &= \frac{\omega_w R_w - v}{v} \\ \dot{\omega}_w &= \frac{R_w N_v \mu(\psi) - \tau_b}{J_w} \\ \dot{v} &= \frac{-N_v \mu(\psi)}{M_v} \end{aligned} \tag{5.25}$$

To successfully implement slip control, the vehicle speed needs to either be measured through the use of a sensor or an estimation technique. It is assumed that there is direct access to the vehicle speed in the derivations presented below. Both equation (5.24) and equation (5.25) follow the same design procedure and for the sake of simplicity only the derivations of the ABS will be shown, however, results from both TC and ABS will be presented and discussed later. Any friction terms in equation (5.24) and equation (5.25) are treated as disturbances and neglected in the controller design. The equilibrium points which are of interest when considering the stability of the slip controller are when $\dot{\psi} = 0$. Applying the quotient rule to the definition of slip in equation (5.25), ψ_{ABS}.

$$\dot{\psi}_{ABS} = \frac{\dot{\omega}_w R_w}{v} + \frac{\omega_w R_w}{v^2}\dot{v} \tag{5.26}$$

From the definition of slip from equation (5.25) it is possible to rewrite ω_w as

$$\omega_{w(ABS)} = \frac{v}{R_w}(\psi + 1) \tag{5.27}$$

Inserting the definitions presented in equation (5.25) and equation (5.27) into equation (5.26) creates an expression for the change in slip as seen in equation (5.28)

$$\dot{\psi}_{ABS} = \frac{-1}{v}\left(\frac{(1+\psi)}{M_v} + \frac{R_w^2}{J_w}\right) N_v \mu(\psi) + \frac{R_w}{J_w v}\tau_b \tag{5.28}$$

Rearranging equation (5.28)

$$\begin{aligned} \dot{\psi}_{ABS} &= \frac{-R_w}{J_w v}(\chi_{ABS} - \tau_b) \\ \chi_{ABS} &= \left(R_w + \frac{J_w}{R_w M_v}(1 + \psi_{ABS})\right) N_v \mu(\psi) \end{aligned} \tag{5.29}$$

It is clear from equation (5.29) that an equilibrium point exists whenever $\chi_{ABS} = \tau_b$ an equilibrium point exists. This can be seen in Figure 5.10 as the points where τ_b intersects with the curve, the difference in equation (5.29) becomes 0 which then means that $\dot{\psi}_{ABS} = 0$. This can also be seen in Figure 5.11

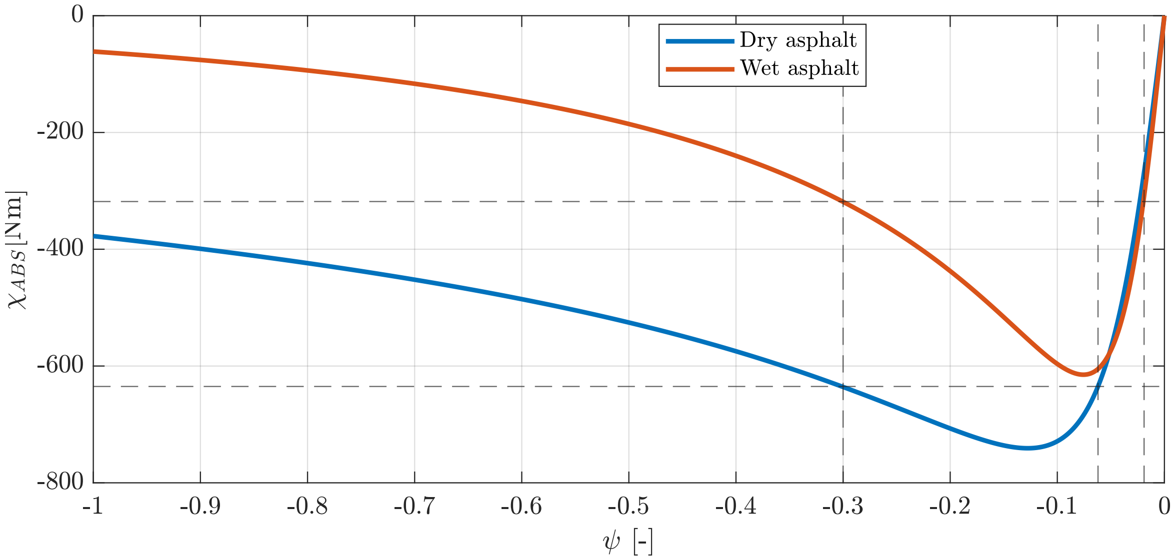

Figure 5.10: Equilibrium points, $\psi_1 = -0.062$,$\psi_2 = -0.3$, for dry asphalt and $\psi_1 = -0.019$,$\psi_2 = -0.3$ for $\bar{\tau}_b = -630[Nm]$ and $\bar{\tau}_b = -318[Nm]$ respectively in ABS mode

For the linearization of τ_b, $\bar{\tau}_b$, means that there are two possible outcomes for the amount of equilibrium points of χ_{ABS}.

- If $\bar{\tau}_b > \min(\chi_{ABS})$ then there exists at least two equilibrium points ψ_1 and ψ_2
- if $\bar{\tau}_b < \min(\chi_{ABS})$ then there exists no equilibrium points for ψ_{ABS}

The linearization point for $\bar{\tau}_b$ is chosen such that the corresponding $\bar{\psi}$ is sufficiently close to the desired operating range. The desired operating range, in this case, is in the vicinity of the peak value of $|\chi_{ABS}|$. The peak value is not chosen since it is not feasible to assume that the AAUER will operate in this area all the time. Instead a value of $\bar{\psi} = 0.3$ is chosen as a compromise, this corresponds to a value of $\bar{\tau}_b = -630[Nm]$. Furthermore, as can be seen from Figure 5.10 $\bar{\tau}_b$ will provide at least two equilibrium points for both TC and ABS to be examined. The stability of these equilibrium points for one of the two road surfaces in Figure 5.10 can be more easily examined in the phase plane portrait of equation (5.29). This can be seen in Figure 5.11 for a dry asphalt road surface.

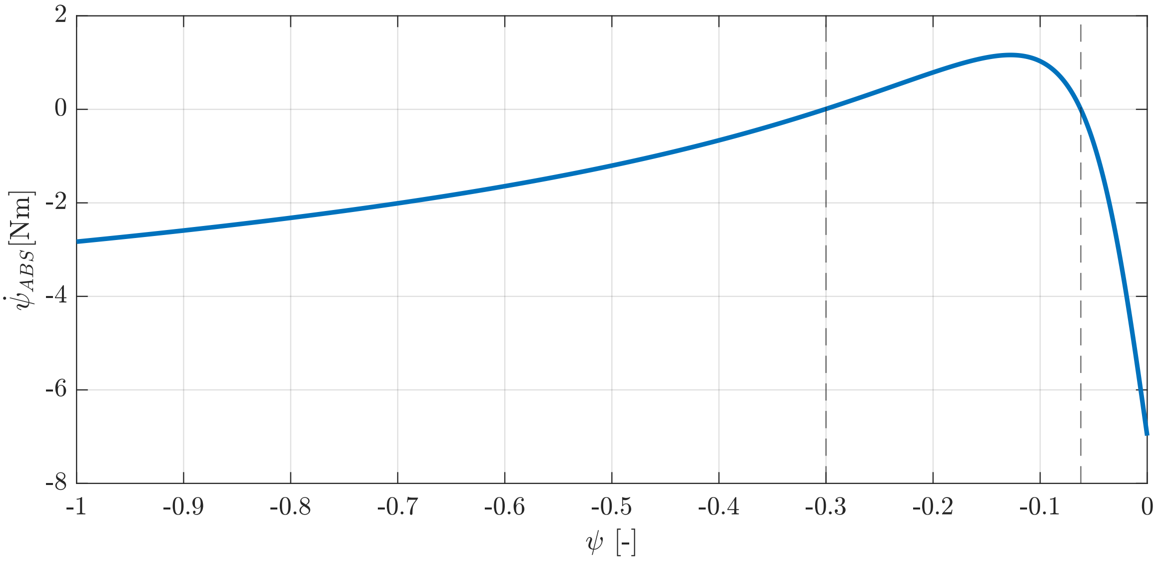

Figure 5.11: Phase plane portrait of $\dot{\psi}_{ABS}$ as a function of ψ at $\bar{\tau}_b$. Equilibrium points at $\psi_1 = -0.062$,$\psi_2 = -0.3$

As seen from Figure 5.11 there exist a locally asymptotically stable equilibrium point at $\psi_1 = -0.062$ and an unstable one at $\psi_2 = -0.3$. Equilibrium point ψ_1 is asymptotically stable since values of ψ close to ψ_1 will converge to zero as $t \to \infty$ due to the change ψ around the equilibrium point[32][p.50]. As can be seen from Figure 5.11 any equilibrium point which is located beyond the peak of the μ curve is unstable since the change in ψ will push ψ away from the equilibrium point.
Repeating the same procedure for TC the change in ψ_{TC} can be described by equation (5.30). Recalling the definition for slip for TC, as seen in equation (5.24), is different for that of ABS, as seen in equation (5.25).

$$\begin{aligned}\dot{\psi}_{TC} &= \frac{-R_w(1-\psi_{TC})^2}{J_w v}(\chi_{TC} - \tau_{em}) \\ \chi_{TC} &= N_v \mu \left(\frac{J}{M_v R_w} \cdot \frac{1}{(1-\psi_{TC})} + R_w \right)\end{aligned} \tag{5.30}$$

Choosing the same linearization point for the motor torque is similar to that of the brake torque. That is, with consideration of the operating range of the TC. That is, $\bar{\psi}_{TC} = 0.3[Nm]$

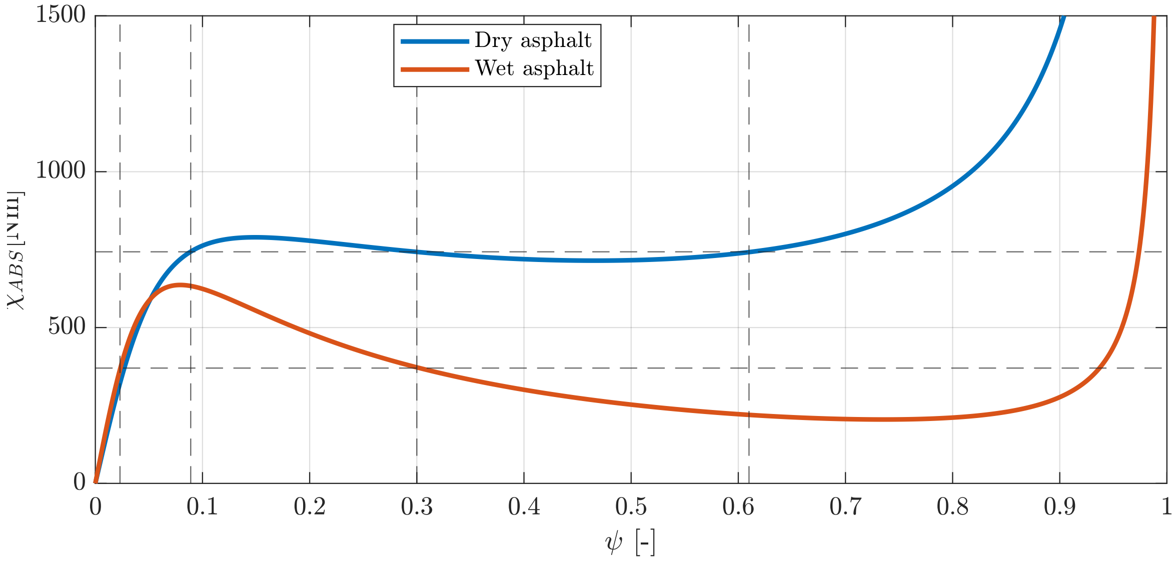

Figure 5.12: Equilibrium points, $\psi_1 = 0.084$,$\psi_2 = 0.30$,$\psi_3 = 0.61$ for dry asphalt and $\psi_1 = 0.023$,$\psi_2 = 0.30$,$\psi_3 = 0.95$ for $\bar{\tau}_b = 743[Nm]$ and $\bar{\tau}_b = 370[Nm]$ respectively in TC mode

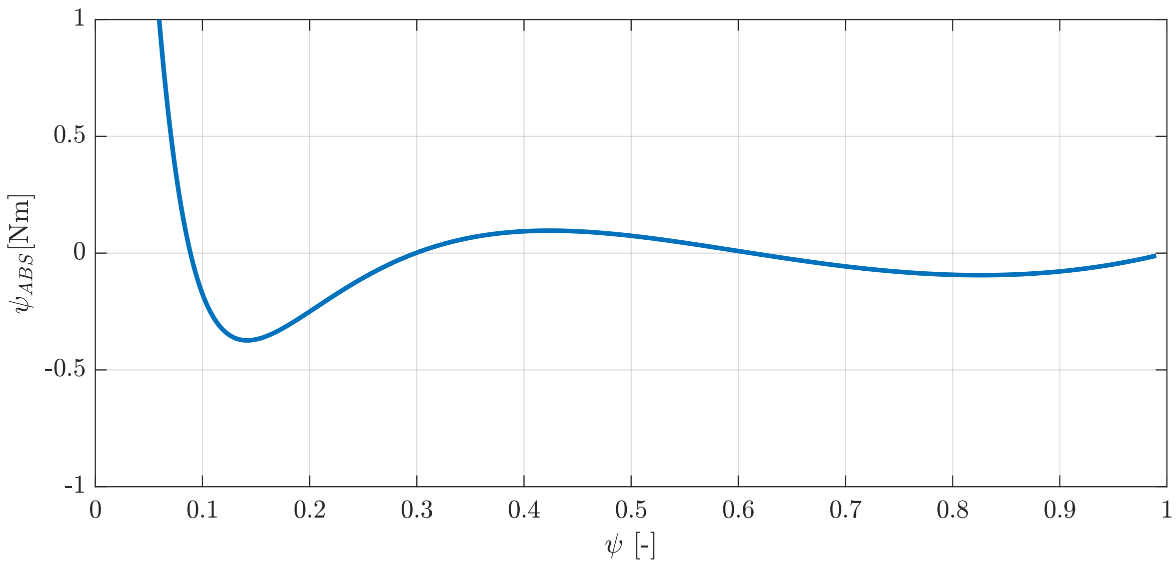

Figure 5.13: Phase plane portrait of $\dot{\psi}_{TC}$ as a function of ψ for $\bar{\tau}_{em}$. Equilibrium points at $\psi_1 = 0.084$,$\psi_2 = 0.30$,$\psi_3 = 0.61$

As can be seen from Figure 5.13 there exist three equilibrium points. $\psi = 1$ is not considered an equilibrium point since for the definition of slip during TC mode as seen in equation (5.24) for it to be equal to 1 would mean that the wheel is moving with the vehicle being stationary or ω_w is infinitely big. Furthermore, no points exists beyond $\psi = 1$ making it unable to describe the equilibrium point[32, p. 50]. With the stability of the equilibrium points analyzed it is now possible to move on to controller design with the properties of the equilibrium points in mind.

Linear Controller Design

In order to implement a linear controller, the nonlinear systems presented in equation (5.24) and equation (5.25) need to be linearized. Specifically the nonlinear adhesion model which both equation (5.24) and equation (5.25) depend upon. Similar to how the equilibrium points were investigated, the procedure will be explained for one of the two slip controllers, and then results from both controllers will be presented in the end. The derivations for the ABS linearization and transfer function are presented here.

$$\begin{aligned} \Delta\omega_w &= \omega_w - \bar{\omega}_w \\ \Delta v &= v - \bar{v} \end{aligned} \tag{5.31}$$

$$\mathbf{x} = \begin{bmatrix} \omega_w \\ v \end{bmatrix} \tag{5.32}$$

The first order Taylor Series Expansion (TSE) of the adhesion model can be seen in equation (5.33)

$$\begin{aligned} \mu(\bar{\psi}) &\approx \mu_0(\bar{\psi}) + \left[\frac{\partial\mu}{\partial\psi}\frac{\partial\psi}{\partial v}\right]\Bigg|_{\psi=\bar{\psi}} \Delta v + \left[\frac{\partial\mu}{\partial\psi}\frac{\partial\psi}{\partial w}\right]\Bigg|_{\psi=\bar{\psi}} \Delta w \\ \mu(\bar{\psi}) &\approx \mu_0(\bar{\psi}) + \mu_1(\bar{\psi})\frac{\omega_w R_w}{v^2}\Delta v - \mu_1(\bar{\psi})\frac{R_w}{v}\Delta\omega \end{aligned} \tag{5.33}$$

Inserting equation (5.33) into equation (5.24) and then take the partial derivatives with respect to the states.

$$A = \begin{bmatrix} -\frac{N_v\mu_1(\bar{\psi})R_w^2}{J_w v} & \frac{N_v\mu_1(\bar{\psi})\omega_w R_w^2}{J_w v^2} \\ \frac{N_v\mu_1(\bar{\psi})R_w}{M_v v} & -\frac{N_v\mu_1(\bar{\psi})R_w}{M_v v^2} \end{bmatrix} \tag{5.34}$$

$$B = \begin{bmatrix} \frac{1}{J_w} \\ 0 \end{bmatrix}, \quad C = \begin{bmatrix} 1 & 0 \end{bmatrix}, \quad x = \begin{bmatrix} \Delta\omega_w \\ \Delta v \end{bmatrix} \quad u = \begin{bmatrix} \tau_b \\ 0 \end{bmatrix} \tag{5.35}$$

Converting the state space formulation into a transfer function using equation (5.36)

$$G_p(s) = C(Is - A)^{-1}B \tag{5.36}$$

Equation (5.37) is used to express the wheel speed in terms of car speed and slip.

$$w_{ABS} = \frac{v}{R_w}(\psi + 1) \tag{5.37}$$

$$G_{\omega_w}(s) = \frac{\omega_w}{\tau_b} = -\frac{s + \frac{N_v \mu_1(\bar{\psi})}{M_v v}(\psi + 1)}{s^2 + s\frac{N_v \mu_1(\bar{\psi}) v}{M_v v}\left(\frac{M_v R_w^2}{J_w} + (\psi + 1)\right)} \tag{5.38}$$

A relationship between wheel deceleration and slip can be established using equation (5.26). This can be seen in equation (5.39).

$$\dot{\omega}_w = \dot{\psi}_{ABS}\frac{v}{R_w} - \frac{\omega}{v}\dot{v} \tag{5.39}$$

Using equation (5.39) and the definitions from equation (5.25) it is possible to rewrite equation (5.38) to equation (5.40)

$$G_{\psi_{ABS}} = \frac{\psi}{\tau_b} = \frac{R_w}{J_w \bar{v}} \frac{1}{s + \frac{\mu_1(\psi) N_v}{M_v \bar{v}}\left(\frac{M_v R_w^2}{J_w} + (\psi + 1)\right)} \tag{5.40}$$

The same procedure is repeated for TC which results in equation (5.41)

$$G_{\psi_{TC}} = \frac{\psi}{\tau_{em}} = \frac{R_w}{J_w \bar{v}} \frac{1}{s + \frac{\mu_1(\psi) N_v}{M_v \bar{v}}\left(\frac{1}{(1-\hat{\psi})} + \frac{M_v R_w^2}{J_w}\right)} \tag{5.41}$$

The pole of equation (5.40) is

$$pole = -\frac{\mu_1(\psi) N_v}{M_v \bar{v}}\left(\frac{M_v R_w^2}{J_w} + (\psi + 1)\right) \tag{5.42}$$

Referring back to Figure 4.6 and seen from equation (5.42) as long as the slope of the adhesion curve is positive the plant is stable. However, once the linearization point of $\bar{\psi}$ passes the peak of the adhesion curve the pole becomes unstable as seen in equation (5.42). Since the slop of the adhesion curve is bounded, as the slip can only vary from minus one to one, then it is still possible to design a controller in order to guarantee asymptotic stability of the slip controller.
The controller used will be a PI controller

$$G_{c,ABS}(s) = \frac{k_{p,ABS} s + k_{i,ABS}}{s} \tag{5.43}$$

The closed-loop transfer function for the system is then

$$G_{cl,ABS} = \frac{\psi}{\psi_{ref}} = \frac{\frac{R_w}{J_w \bar{v}} k_{p,ABS} s + k_{i,ABS}}{s^2 + s\left(\frac{\mu_1(\bar{\psi}) N_v}{M_v \bar{v}}\left(\frac{M_v R_w^2}{J_w} + (\bar{\psi} + 1)\right) + \frac{R_w k_p}{J_w \bar{v}}\right) + \frac{R_w k_i}{J_w \bar{v}}} \tag{5.44}$$

The control design will be done on the basis of a worst case scenario. Which means for the linearization point of $\bar{\psi}$ that it is chosen to be unstable, beyond the peak of the adhesion curve. Furthermore, to prove the robustness of the control design, the controller will be designed for dry asphalt but will be tested on a wet asphalt road surface. A summary of the linearization points used are:

Variable	Value	Unit
$\bar{v}$	17.5	$[\frac{m}{s}]$
$\bar{\psi}$	-0.3	$[-]$

The linearization point of $\bar{v}$ is chosen to be $17.5[\frac{m}{s}]$ since this is the average speed the AAUER achieves during the course of an endurance race, as seen in Figure 2.2. Inserting the numerical values in section 5.3.1 into equation (5.44) yields the following transfer function.

$$G_{plant,ABS} = \frac{\psi}{\tau_b} = \frac{0.00577}{s - 3.051} \tag{5.45}$$

As can be seen from equation (5.45) the closed-loop transfer function with a unit gain is unstable and as a result, requires a controller to both stabilize and meet design requirements. The controllers are designed with the following criteria

- Minimal overshoot. Settling time is considered more important design criteria compared to overshoot. As such, as long as the pole location criteria have fulfilled any overshoot associated with it will be considered acceptable.
- ω_n is designed such that it is located between the dominating pole of the current loop and the speed loop as illustrated in figure 5.1. That is, at least as fast as the dominating pole of the speed loop pole at 169.41.

$$\begin{aligned}
\zeta &= cos\left[tan^{-1}\left(\frac{-\pi}{ln(O)}\right)\right] \implies \zeta > 0.59 \\
\omega_n &= 169.4080\left[\frac{rad}{sec}\right] \\
k_{i,ABS} &= \frac{\omega_n^2}{0.002959} = 2.61 \cdot 10^6 \\
k_{p,ABS} &= \frac{2\zeta_n - 1.102}{0.002959} = 1.87 \cdot 10^4
\end{aligned} \tag{5.46}$$

$$\begin{aligned}
G_{c,ABS}(s) &= \frac{18720s + 2.61 \cdot 10^6}{s} \\
G_{cl,ABS}(s) &= \frac{\psi}{\psi_{ref}} = \frac{108s + 1.51 \cdot 10^4}{s^2 + 105s + 1.51 \cdot 10^4}
\end{aligned} \tag{5.47}$$

A step of equation (5.47) is done in Figure 5.14 where the linearization point of $\bar{v}$ is changed to see its effect. Recall that in order to test the robustness of the control design. The road surface, adhesion coefficient, is changed from dry tarmac to wet tarmac.

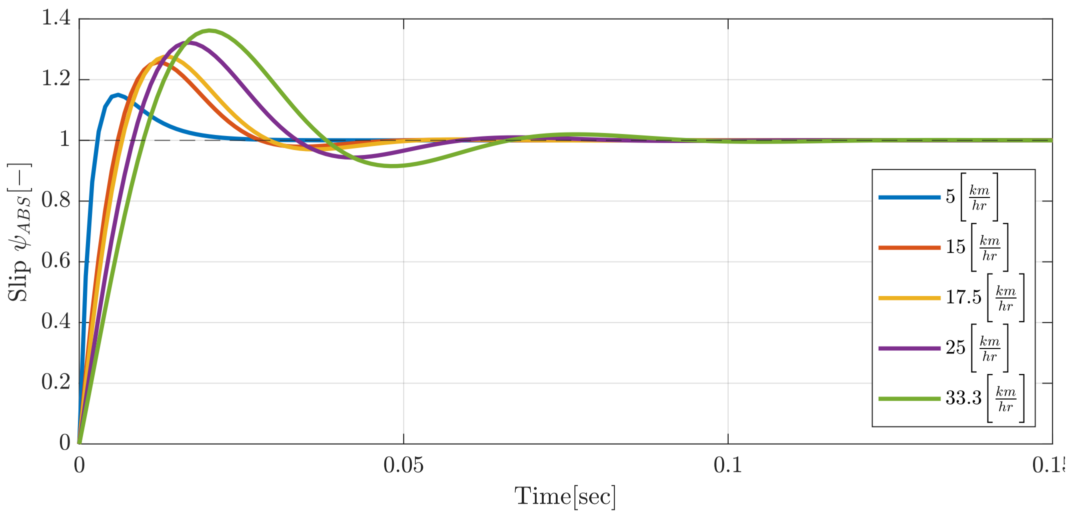

Figure 5.14: Step response of equation (5.47) for different linearization points.

Due to the similarity between equation (5.40) and equation (5.41) the controller designed is also used for TC. Using the same controller designed in equation (5.47) the corresponding closed loop step response can be seen in Figure 5.15 for TC.

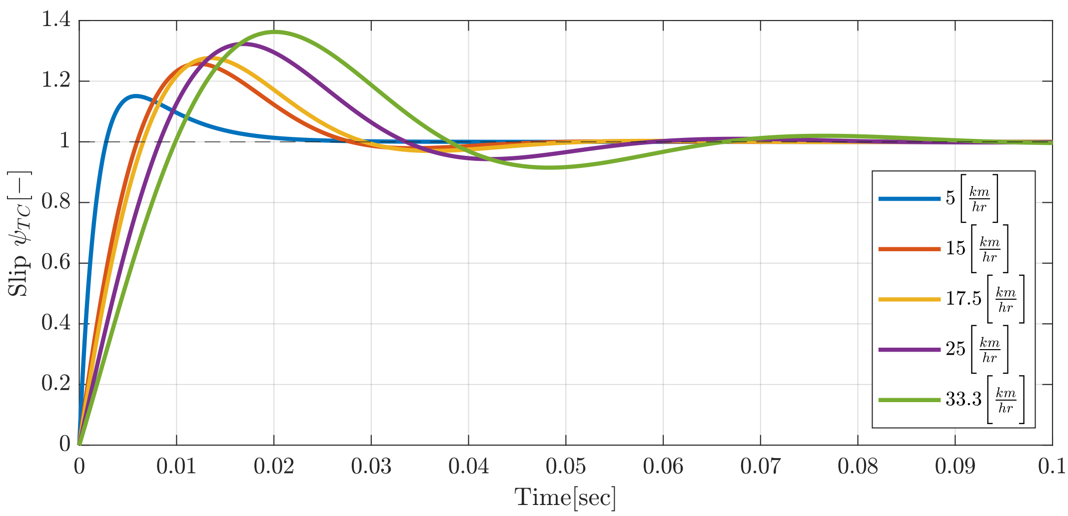

Figure 5.15: Closed loop step response of equation (5.41) and equation (5.47) for TC.

It can be seen that figure 5.14 and figure 5.15 behave identically. This concludes the linear control design section for ABS and TC.

5.3.2 Non-Linear Slip Control

The derivations and discussions presented for the Super-Twisting Sliding Mode Controller(STSMC) are inspired from [31, pp. 33–36]. The STSMC is a continuous adaptation of the conventional discontinuous Sliding Mode Controller(SMC). This is considered favorable compared to the discontinuous control law of the conventional SMC in terms of practical implementation. The STSMC used here will be a tracking control algorithm, which means that instead of system states used for the definition of the sliding variable an error between the reference and current system state is used. This can be seen in equation (5.48).

$$\begin{aligned}\tilde{\psi} &= \psi_{ref} - \psi \\ \dot{\tilde{\psi}} &= \dot{\psi}_{ref} - \dot{\psi}\end{aligned} \tag{5.48}$$

The sliding variable can then be defined as equation (5.49).

$$\begin{aligned}\sigma &= \dot{\tilde{\psi}} + c\tilde{\psi} \\ \dot{\sigma} &= -c\,|\sigma|^{0.5}\,\mathrm{sign}(\sigma)\end{aligned} \tag{5.49}$$

It should be noted that this definition of $\dot{\sigma}$ does not account for any disturbances. A Lyapunov function is introduced in order to derive a control law which provides asymptotic stability about $\sigma = 0$. This equilibrium point is significant since once $\sigma = 0$ the solution to equation (5.49) becomes

$$\begin{aligned}\tilde{\psi}(t) &= \tilde{\psi}(0)exp(-ct) \\ \dot{\tilde{\psi}}(t) &= -c\tilde{\psi}(0)exp(-ct)\end{aligned} \tag{5.50}$$

As can be seen from equation (5.50) when $\sigma = 0$ both error states converge asymptotically to zero. The Lyapunov candidate function can be seen in equation (5.51) and its derivative in equation (5.52)

$$V_{lyap} = \frac{1}{2}\sigma^2 \tag{5.51}$$

$$\dot{V}_{lyap} = \sigma\dot{\sigma} \tag{5.52}$$

In order to guarantee asymptotic stability equation (5.51) needs to be positive definite and equation (5.52) needs to be either negative definite[32, pp. 107–109] or negative semi-definite where equation (5.52) is continuously bounded as postulated by the Lyapunov-like Lemma[32, pp. 123–125]. An additional desirable feature is that of global stability. These conditions for the Lyapunov candidate function are summerized in equation (5.53).

$$\begin{aligned} &V_{lyap} > 0 \text{ for } \sigma \neq 0 \\ &\dot{V}_{lyap} < 0 \text{ for } \sigma \neq 0 \\ &\lim_{|\sigma| \to \infty} V_{lyap} = \infty \end{aligned} \tag{5.53}$$

From the requirements in equation (5.53) and the definition of the sliding variable in equation (5.49) the continuous control law in equation (5.54) is derived.

$$u = c\,|\sigma|^{0.5}\,\text{sign}(\sigma) \tag{5.54}$$

The finite time it takes for equation (5.49) to converge to zero can be determined by integrating equation (5.49) with respect to time as seen in equation (5.55).

$$\begin{aligned} |\sigma|^{0.5} - |\sigma_0|^{0.5} &= -\frac{c}{2}t \\ t_r &= \frac{2}{c}\,|\sigma|^{0.5} \end{aligned} \tag{5.55}$$

The assumption made in equation (5.49) about the absence of any disturbances in impractical from a practical implementation point of view. As a result the control law in equation (5.54) will not converge since the new dynamics of the sliding variable will be as seen in equation (5.56)

$$\dot{\sigma} = f_{disturbance}(t) - c\,|\sigma|^{0.5}\,\text{sign}(\sigma) \tag{5.56}$$

To accommodate this an additional term is added to the control law in equation (5.54) which compensates for any disturbances assuming $\left|\dot{f}_{disturbance}\right| \leq C$.

$$\begin{aligned} u &= c\,|\sigma|^{0.5}\,\text{sign}(\sigma) + w \\ \dot{w} &= b\text{sign}(\sigma) \\ b &= 1.1C \\ c &= 2.0 \cdot 10^4 \\ C &= 100 \end{aligned} \tag{5.57}$$

Another positive attribute of the STSMC besides a continuous approach to the conventional discontinuous SMC is the fact that the chattering is attenuated through the integral term of $\dot{w}$ in equation (5.57). Implementing the STSMC, similar to that of the linear slip control, can be seen in Figure 5.16.

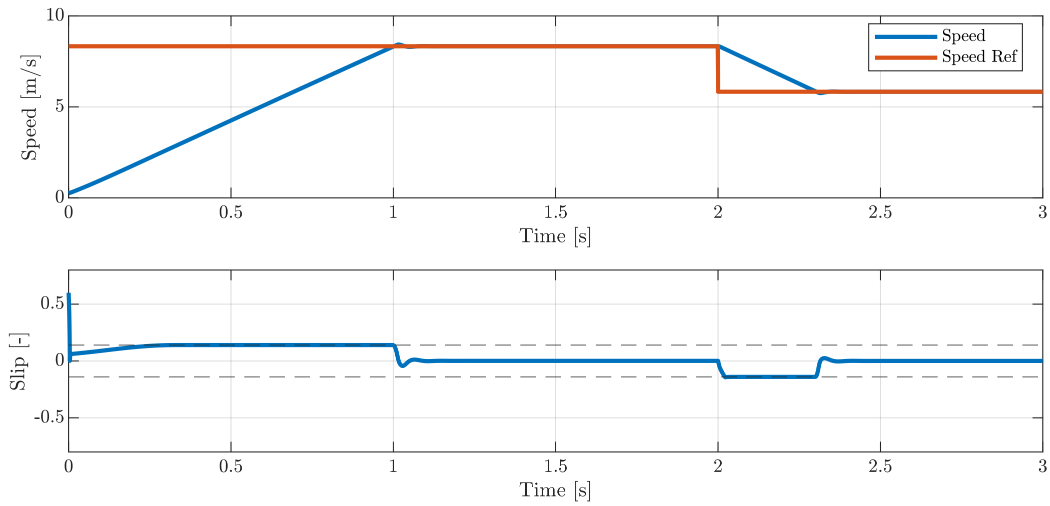

Figure 5.16: STSMC Slip Control

Implementation of Slip Control

TC and ABS are implemented in such as way that they serve as upper and lower limits for the i_q current. This means that the motor torque going into the wheel is already adjusted so optimal slip is achieved in the case of acceleration or deceleration. The torque output from TC and ABS is converted into an i_q current using equation (2.2). The implementation of slip control can be seen in Figure 5.21.

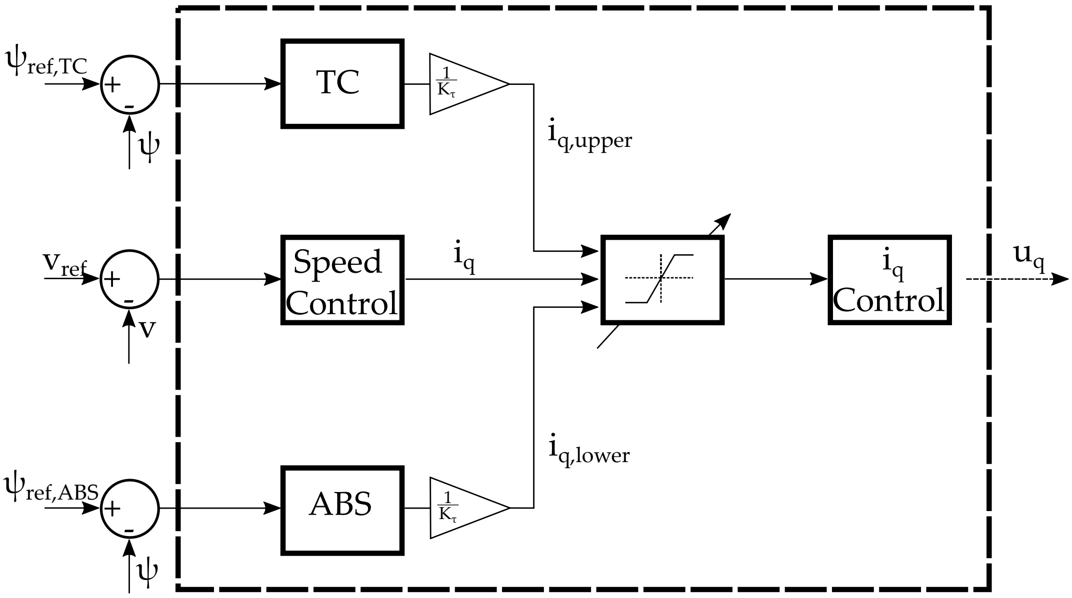

Figure 5.17: Simulink implementation on dynamic upper and lower limit for slip control of i_q

For this implantation to work properly, the upper and lower limits must be adjusted accordingly depending on the speed reference. In other words, when the car is accelerating the TC is limiting the i_q current but at the same time, the ABS should be disconnected to prevent integrator windup.

Activation Logic

To accommodate this, an activation/deactivation logic is implemented. The activation and deactivation are done based on the sign of the i_q current. The reason why the i_q current is due to the non-salient nature of the PMSM and that negative i_q current can be related to braking motion through equation (2.2). That is,

$$ABS = \begin{cases} 0 & \text{if } i_q > 0 \\ 1 & \text{if } i_q < 1 \end{cases} \tag{5.58}$$

$$TC = \begin{cases} 1 & \text{if } i_q > 0 \\ 0 & \text{if } i_q < 1 \end{cases} \tag{5.59}$$

Anti-Wind up

Both the linear controller and the non-linear controller use an integrator in their respective control methods. Whenever activation/deactivation of TC/ABS happens it is important that the controller is disabled properly. As such, it would be prudent to address the issue of integrator windup. The PI controller for the linear slip control is fitted with the common anti-windup topology as shown in Figure 5.22.

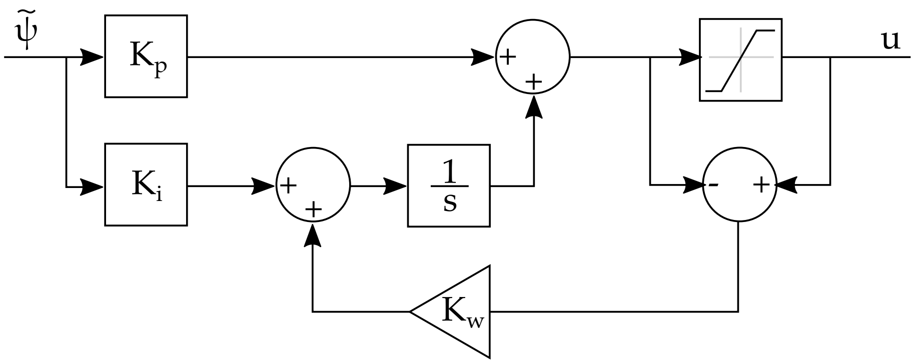

Figure 5.18: Simulink implementation of the integrator anti-windup for the linear PI controller.

In the case of the nonlinear STSMC controller integrator anti-windup is implemented in the form of a switch where both the reference and the controller output are set to zero. This will prevent the STSMC from winding up as the ABS or the TC are deactivated since the input error is zero. Since the STSMC is now located on the sliding surface[1, p. 73]. The controller output of the STSMC is shown in Figure 5.23 with the proposed anti-windup logic and without it in Figure 5.24 where the speed reference is the first 30$[s]$ of the track described in section 2.1.1.

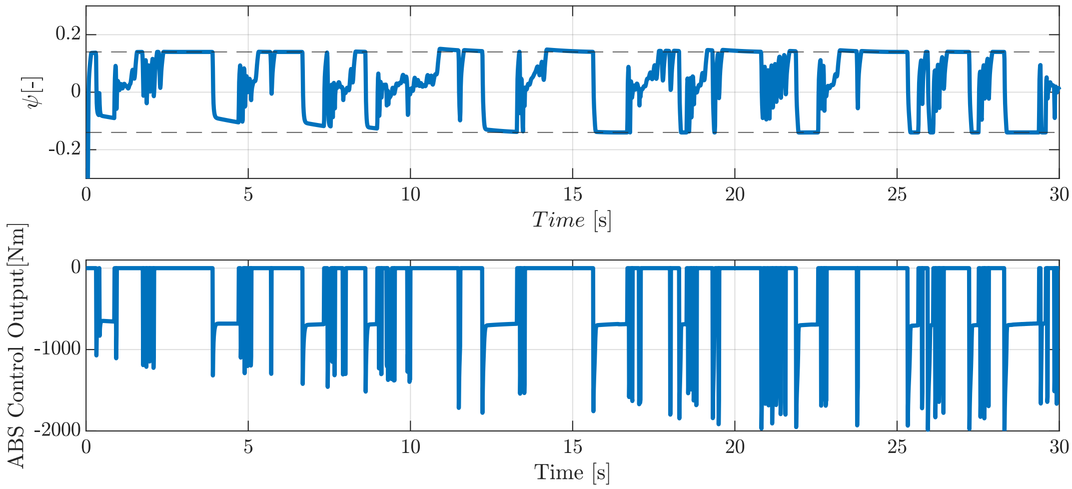

Figure 5.19: STSMC with integrator anti-windup implemented. In the top plot with ψ on the y-axis, the dashed lines show the optimal ψ reference.

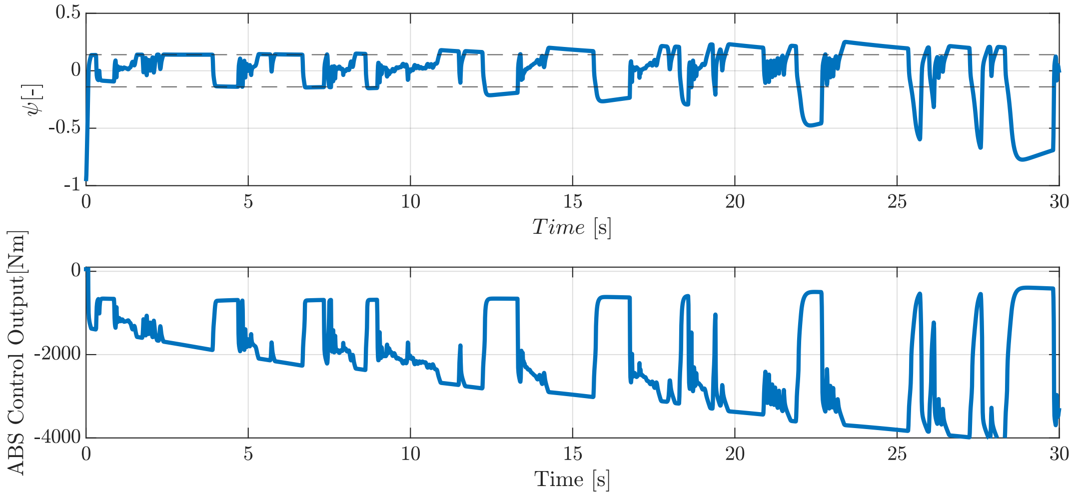

Figure 5.20: STSMC without integrator anti-windup implemented. In the top plot with ψ on the y-axis, the dashed lines show the optimal ψ reference.

As can be seen in Figure 5.24 as time progresses that the integrator value starts accumulating as the ABS is activated and deactivated. This then results in incorrect control signals to the dynamic saturation block for the i_q current which causes the slip to exceed a given reference. However, as can be seen in Figure 5.23 this integrator windup is successfully negated.

Implementation of Slip Control

TC and ABS are implemented in such as way that they serve as upper and lower limits for the i_q current. This means that the motor torque going into the wheel is already adjusted so optimal slip is achieved in the case of acceleration or deceleration. The torque output from TC and ABS is converted into an i_q current using equation (2.2). The implementation of slip control can be seen in Figure 5.21.

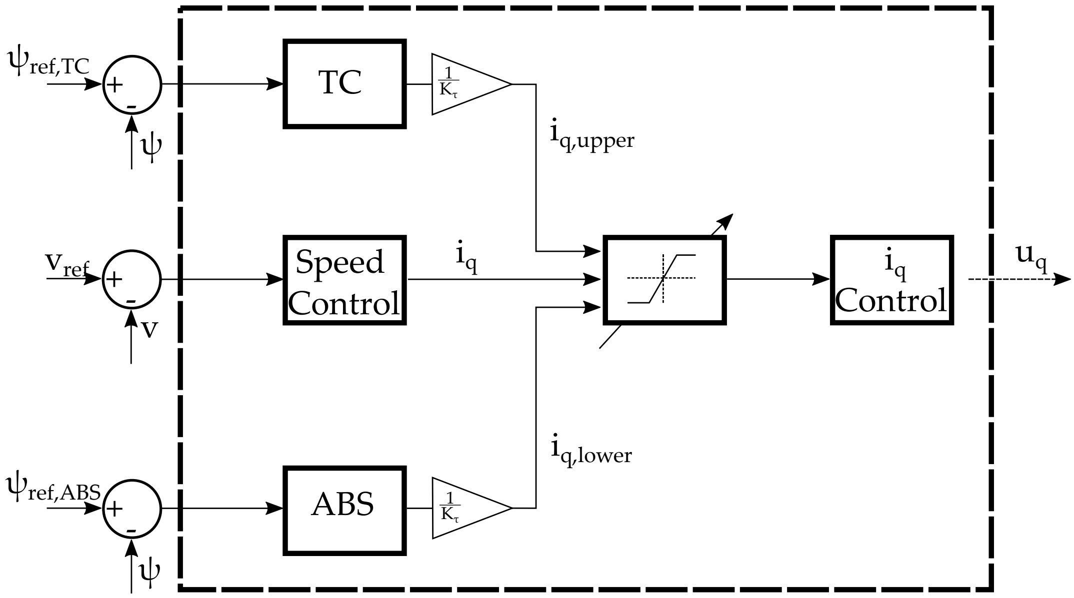

Figure 5.21: Simulink implementation on dynamic upper and lower limit for slip control of i_q

For this implantation to work properly, the upper and lower limits must be adjusted accordingly depending on the speed reference. In other words, when the car is accelerating the TC is limiting the i_q current but at the same time, the ABS should be disconnected to prevent integrator windup.

Activation Logic

To accommodate this, an activation/deactivation logic is implemented. The activation and deactivation are done based on the sign of the i_q current. The reason why the i_q current is due to the non-salient nature of the PMSM and that negative i_q current can be related to braking motion through equation (2.2). That is,

$$ABS = \begin{cases} 0 & \text{if } i_q > 0 \\ 1 & \text{if } i_q < 1 \end{cases} \qquad (5.60) \qquad\qquad TC = \begin{cases} 1 & \text{if } i_q > 0 \\ 0 & \text{if } i_q < 1 \end{cases} \qquad (5.61)$$

Anti-Wind up

Both the linear controller and the non-linear controller use an integrator in their respective control methods. Whenever activation/deactivation of TC/ABS happens it is important that the controller is disabled properly. As such, it would be prudent to address the issue of integrator windup. The PI controller for the linear slip control is fitted with the common anti-windup topology as shown in Figure 5.22.

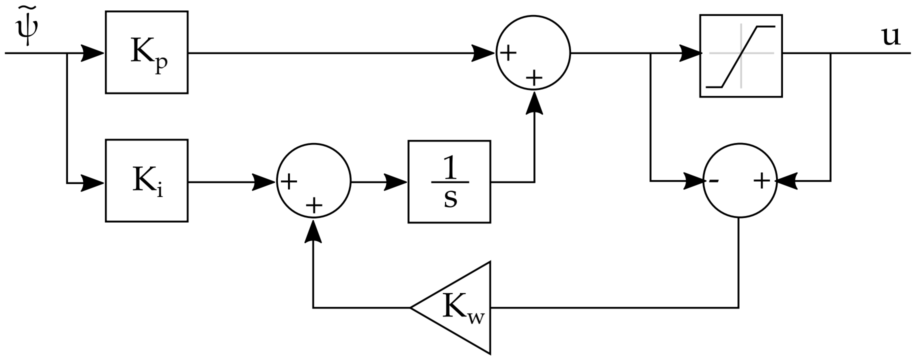

Figure 5.22: Simulink implementation of the integrator anti-windup for the linear PI controller.

In the case of the nonlinear STSMC controller integrator anti-windup is implemented in the form of a switch where both the reference and the controller output are set to zero. This will prevent the STSMC from winding up as the ABS or the TC are deactivated since the input error is zero. Since the STSMC is now located on the sliding surface[1, p. 73]. The controller output of the STSMC is shown in Figure 5.23 with the proposed anti-windup logic and without it in Figure 5.24 where the speed reference is the first $30[s]$ of the track described in section 2.1.1.

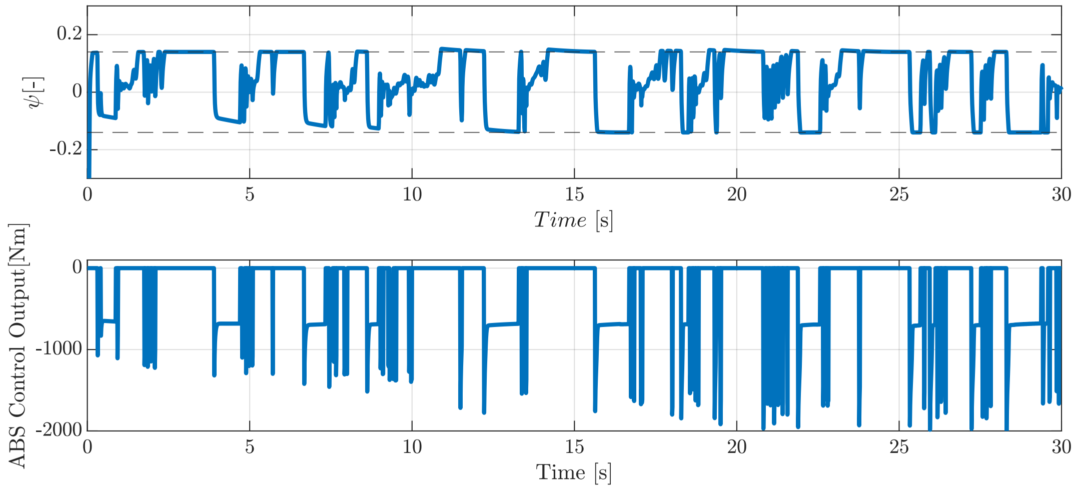

Figure 5.23: STSMC with integrator anti-windup implemented. In the top plot with ψ on the y-axis, the dashed lines show the optimal ψ reference.

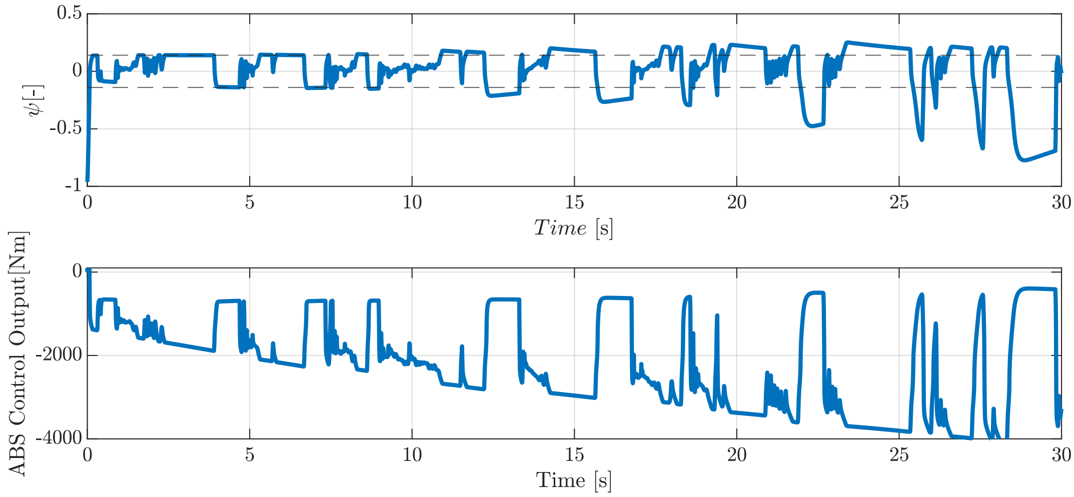

Figure 5.24: STSMC without integrator anti-windup implemented. In the top plot with ψ on the y-axis, the dashed lines show the optimal ψ reference.

As can be seen in Figure 5.24 as time progresses that the integrator value starts accumulating as the ABS is activated and deactivated. This then results in incorrect control signals to the dynamic saturation block for the i_q current which causes the slip to exceed a given reference. However, as can be seen in Figure 5.23 this integrator windup is successfully negated.

5.4 Slip Control Reference

For slip control to provide the maximum tractive force, the slip needs to be so that it provides the maximum adhesion. As can be seen in Figure 5.25 depending on the road condition the maximum adhesion for a given slip ratio changes.

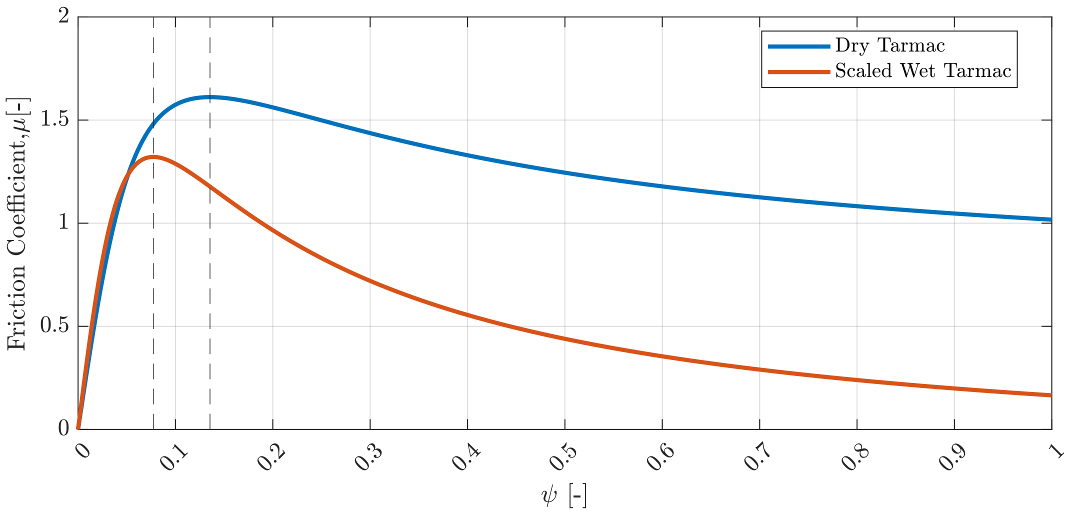

Figure 5.25: Maximum adhesion coefficient as a function of ψ for dry/wet tarmac road conditions. Peak adhesion coefficients are marked with a dashed line.

For the slip reference there are thus two options,

- Online estimation of the optimum slip
- Predefined optimum slip

In [12] a recursive least square(RLS) is suggested as a possibility to estimate slip ratio. In [1] an RLS estimation of the maximum slip for slip control of a small passenger vehicle is implemented. Where the algorithm uses a linear relationship between the adhesion coefficient and the corresponding slip, based on an approximation of the Burckhardt equation, to determine the corresponding slip for the highest possible adhesion coefficient. The advantage of online estimation of the optimal slip is the fact that, as long as convergence is guaranteed, that you always utilize the full tractive force permissible for a given tire-road condition. Furthermore, if the road conditions change during vehicle operation then the slip controller will be able to adapt to these changes as well. In the case of a predefined optimum slip, maximum tractive force is leveraged for robustness. Since the optimum slip is predetermined based on known road conditions, making it impervious to any disturbances could cause a slip estimation to be incorrect. However, as was just mentioned consideration must be made about the road conditions when selecting the slip reference. In the case of the AAUER, since the road conditions are limited to either dry, damp, or wet asphalt [10, p. 199 D3.1], it could be advantageous to select a slip reference based on these conditions. One possibility which will require the least amount of reconfiguration is selecting an optimum slip reference based on a compromise between the two road conditions. From Figure 5.25 the maximum adhesion coefficient for wet tarmac is located at $\psi_{wet} = 0.078$ and $\psi_{dry} = 0.136$. Averaging these yields an optimum slip reference of $\psi_{avg} = 0.11$, the corresponding amount of lost peak tractive force can be seen in section 5.4.

Road Surface	Peak Dry$[Nm]$	Peak Wet$[Nm]$	Peak Loss Dry$[\%]$	Peak Loss Wet$[\%]$
$\psi_{max,dry}$	2394.4	1747.0	-	11.02
$\psi_{max,wet}$	2207.1	1963.3	7.82	-
$\psi_{max,avg}$	2368.9	1873.4	1.06	4.58

From section 5.4, it is evident that choosing a slip equidistant from the two peaks does not result in an equal loss in peak tractive force, due to the shape of the adhesion curves. Another approach instead of choosing an average distance between two peaks could be to implement a switch on the AAUER, where one configuration utilizes the optimum slip reference for dry road conditions, and another configuration sets the slip reference for wet road conditions. This way the robustness of a predefined slip reference is maintained, however, at the expense of relying more on the expertise of the driver to know when each scenario is. The consequences of incorrect management of these configurations will lead to a more severe loss of tractive force, however, the benefit of having reconfigurability while driving and robustness of a constant reference off-sets the potential loss of tractive force.

5.5 Regenerative Braking

As the car will have to brake, the speed controller will make the q-axis current negative to slow down the car. This change in the current sign results in the inverter increasing the DC link voltage to force the current into the battery pack. The DC link voltage is not allowed to exceed $600[V]$ as stated by the FSG ruleset [8][EV4.1.1] and thus the current is limited by the OCV, and in turn SoC, of the battery pack.
The sign of the current is determined by the function in Equation (5.62)

$$i_s = \begin{cases} \sqrt{i_q^2 + i_d^2} & \text{if } \operatorname{sign}(i_q) = 1 \\ -\sqrt{i_q^2 + i_d^2} & \text{if } \operatorname{sign}(i_q) = -1 \end{cases} \tag{5.62}$$

To prevent the inverter from exceeding the $600[V]$ limit, a limit should be calculated based on the OCV of the battery. In Simulink, the OCV is readily available from the lookup tables used for the battery model but would have to be estimated in a real-life application. The inverter voltage command will then have a lower limit calculated by

$$limit = -(V_{DC,max} - OCV) \tag{5.63}$$

The OCV of the battery pack decreases as SoC decreases, meaning the voltage command limit becomes less restricted as the battery pack discharges. There is however a second limitation to consider, which is the battery pack itself. In 4.2.2 an INR18650 cell was scaled to have parameters equivalent to that of a battery pack with the calculated capacity, it was however not considered whether or not the pack can handle the discharging and charging currents required by the PMSM. The datasheet of the INR18650 will serve as a reference for the allowable currents. Charging a maximum of $2[A]$ is acceptable while a discharging current of $8[A]$ continuously and $12[A]$ in short periods are tolerated. These currents are however for a cell or series of cells and are increased if multiple parallel cells are connected. For the AAUER the battery pack is will have 9 parallel connections meaning the currents are allowed to be 9 times higher. The charging current should be limited to $18[A]$ and the discharging to $72[A]$ continuously. Since the torque of the PMSM is dependant on the current, the charging current generated when braking, is also dependant on the torque. From section 4.1.1 it is known that there exists an optimum point for the traction force and in turn the torque. Calculating the maximum possible torque from the highest possible adhesion coefficient can then be related to a current via the motor constant, k_t and FDR. The maximum torque and current is then

$$\tau_{max} = N_v \, R_w \, \mu_{max} = 598.58Nm \tag{5.64}$$

$$i_{q,max} = \frac{N_v \, R_w \, \mu_{max}}{k_t \, FDR} = 169.22A \approx 170A \tag{5.65}$$

if friction forces are neglected. The adhesion coefficient is assumed to have a symmetric behavior, as stated in section 4.1.1, thus the maximum braking torque and current from the motor are the same but negative. This is a problem as the battery pack's charging current should not exceed $18[A]$. To avoid this, the current command signal is set to have a lower limit of $-18[A]$. The upper limit is set to be $72[A]$ to avoid damaging the battery pack. This however poses new problems, firstly, a current of $170[A]$ is needed to achieve the highest possible acceleration, which is not possible with only 9 parallel connections in the battery pack. Secondly, the braking current would of the PMSM being limited to $-18[A]$ will affect performance negatively, as the AAUER will not be able to brake sufficiently. This leads to the need for mechanical brakes to brake however much is required. While mechanical brakes are required by the ruleset, using them is undesired [10][T6.1.1]. In an ideal situation, the PMSM would be able to be used for braking as well, such that the maximum amount of kinetic energy will be regenerated.

Mechanical Brakes

The braking torque acting on the rear wheel is that of the braking current and the mechanical brakes. The sum of these two torques should be equal to the highest possible braking torque, as calculated in Equation (5.65). The driver of the AAUER will have to use the mechanical brakes, but in simulation this is done with a simple logic circuit

$$\tau_b = \begin{cases} 0 & \text{if } i_q \geq -32A \\ \tau_{ABS} - i_q k_t FDR & \text{if } i_q \leq -32A \end{cases} \tag{5.66}$$

where τ_{ABS} is the torque required by the ABS. The logic ensures that the PMSM is prioritized for braking to regenerate the most amount of energy. The -18 condition is based on the maximum allowed charging current which is $18[A]$.

5.5.1 Redesign of the battery pack

Different design criteria will be used this time for the battery pack voltage requirement. Instead of an allowable max by FSAE, it will be based upon the motor parameters of the EMRAX. Furthermore, it will be based upon the worst-case scenario where the speed of the motor is the highest. For this, the rated speed given in the EMRAX data sheet [4] as,$\omega_{rated} = 5500[rpm]$. Furthermore, All calculations are done in steady-state. The reason why the rated speed is a worst-case scenario is due to the back-emf of the motor.
To properly design the battery all of the requirements calculated in equation (5.65) must be converted from the dq-frame to the abc frame where it is then possible to determine the associated RMS value for both the voltage and the current. The current requirement is calculated from equation (5.65) and the voltage requirement is based upon the restrictions imposed by the back-emf at rated conditions.
At rated conditions $\omega_r = 5500[rpm]$ [4],

$$\omega_e = 5500 \cdot N_{pp} \cdot \frac{2\pi}{60} \tag{5.67}$$

The i_d current is assumed assumed to be be zero.

$$\begin{aligned} u_q &= R_s i_q + \omega_e \lambda_{mpm} = 315.01V \\ u_d &= -\omega_e \lambda_q i_q = -179.18V \end{aligned} \tag{5.68}$$

The motor constants in 5.68 can be found in Appendix A. Using the amplitude invariant inverse park [18, p. 151] transform the following 3-phase voltages are calculated.

$$\begin{bmatrix} u_a \\ u_b \\ u_c \end{bmatrix} = \begin{bmatrix} cos(\theta) & -sin(\theta) \\ cos(\theta - 120) & -sin(\theta - 120) \\ cos(\theta + 120) & -sin(\theta + 120) \end{bmatrix} \begin{bmatrix} u_d \\ u_q \end{bmatrix} \quad (5.69)$$

When $\theta = 0$,in a 3-phase balanced system , the magnitude of the a-phase is at its peak.

$$\begin{bmatrix} u_a \end{bmatrix} = \begin{bmatrix} cos(0) & -sin(0) \end{bmatrix} \begin{bmatrix} -179.18 \\ 315.01 \end{bmatrix} = 362V \quad (5.70)$$

The modulation technique is known, from section 4.2.3, as SVM. That means the DC voltage input of the inverter can be calculated as shown in equation (5.71) [27, p. 354]

$$U_{DC} = \sqrt{3}u_a = \sqrt{3}362 = 627.00V \quad (5.71)$$

The DC voltage required from the battery for rated conditions exceeds the battery requirements set by FSAE as per [10][EV4.1.1]. Using the same steps for calculating U_{DC} as has just been presented it is found that it is possible to achive a max value of $\omega_r = 5200[rpm]$ which gives a $U_{DC} = 593.68$. The i_{DC} current is calculated using equation (4.21). Equation (4.21) is repeated for convenience.

$$i_{DC} = \frac{3}{2} \frac{\hat{u}_q \hat{i}_q + \hat{u}_d \hat{i}_d}{\hat{u}_{DC}} \quad (5.72)$$

The following values are used to calculate the required i_{DC} current of the battery.

	Value	Unit
i_q	170	$[A]$
i_d	0	$[A]$
u_q	297.98	$[V]$
u_d	-169.40	$[V]$
u_{DC}	593.68	$[V]$

The reason why the u_d and u_d values are different from those presented in 5.68 are because these values include the new angular velocity of the motor at $\omega_r = 5200$.

$$i_{DC} = \frac{3}{2} \cdot \frac{297.98 \cdot 170 - 169.40 \cdot 0}{593.68} = 127.99A \quad (5.73)$$

As mentioned previously, the initial iteration of the battery pack, as seen in section 4.2.2, does not fulfill the current requirement set by the motor. Furthermore, the initial voltage requirement set by the battery pack is not based on any design requirements. Instead, it was simply designed to the max allowable limit.

That means $593.68[V]$ is the voltage requirement for the revised battery pack. To guarantee that the requirement is met even when the pack is almost drained the number of cells required in series to meet the new requirement is calculated from the charged voltage of the Samsung INR18650-35E of $4.2[V]$ [29].

$$N_{series,new} = \frac{U_{DC,max}}{U_{max}} = \frac{593.68}{4.2} = ceil(141.35) \approx 142 \tag{5.74}$$

The new nominal voltage of the battery pack is $593.68[V]$ which is below the $600[V]DC$ stated by the FSAE ruleset[10][EV4.1.1]. This yields a capacity of all the cells in series of[35, pp. 40–41].

$$Q_{series} = N_{series,new} U_{max} Q_{bat} \cdot 3600 = 142 \cdot 4.2 \cdot 3.4 \cdot 3600 \approx 7.23MJ \tag{5.75}$$

The current and capacity requirement remains. At the same time from section 5.5 the battery is required to be able to discharge $i_q = 170[A]$ or $127.99[A]$DC to produce the maximum possible torque during optimal slip. The maximum continuous discharge current is $8.00[A]$ and as such there need to be at least

$$N_{parallel,current} = \frac{127.99[A]}{8.00[A]} \approx 16 \tag{5.76}$$

From equation (5.76) a total of 16 parallel connections are required in order to meet the max discharge requirement. A final important design consideration is the capacity requirement. The amount of capacity required to finish the endurance race is known from section 2.1.1.

$$N_{parallel,capacity} = \frac{50.7[MJ]}{7.23[MJ]} \approx 7 \tag{5.77}$$

Since regenerative braking will be implemented the required capacity of $50.7[MJ]$ will be reality be lower. From a simulation of the full AAUER Simulink model, as can be seen in figure 4.14, with and without regenerative braking implemented with FoC motor control is was possible to recover 5.95% of the mechanical energy spent by the AAUER. This means that the new revised capacity requirement is

$$N_{parallel,capacity} = \frac{0.945 \cdot 50.7[MJ]}{7.23[MJ]} \approx 7 \tag{5.78}$$

The amount of parallel connects is however still limited by the current requirement so the final revised battery back design is as follows,

- $N_{series} = 142$
- $N_{parallel} = 16$

5.6 Complete Assembly

The complete implementation of all of the different extended motor control and the motor control strategies can be seen in Figure 5.26.

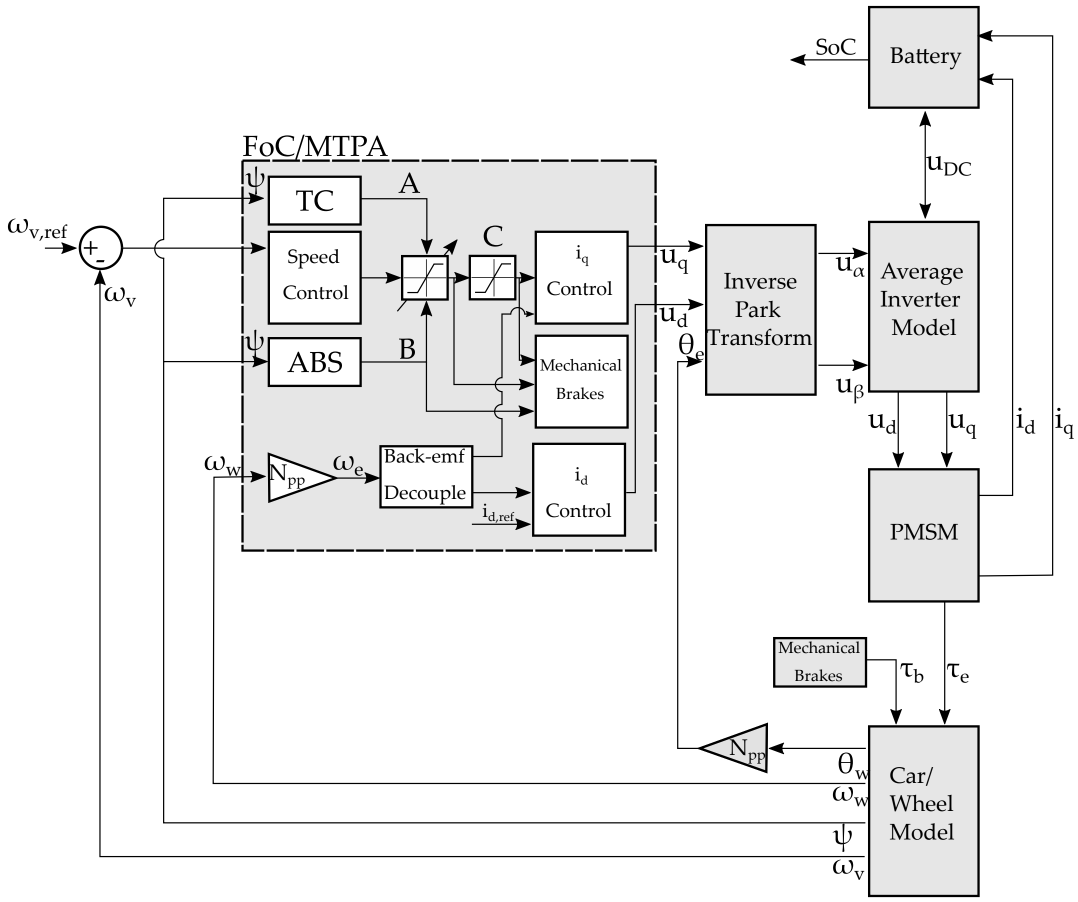

Figure 5.26: A complete illustration of the Matlab Simulink Model

The following description is added to the three labeled parts in Figure 5.26.

- A: The Upper current limitation is provided by TC and is converted from a command torque to an i_q current. In this example the motor control strategy used is FoC and as such the i_q current can be calculated from equation (2.3).
- B: Similar approach as the TC, this time the lower limit for the i_q current is provided by the ABS controller.
- C: This saturation block serves as the current limitations imposed on the battery based upon the battery pack design in section 5.5.1.

The internal control structure of the dashed box labeled is the same for both FoC and MTPA. The only difference between FoC and MTPA is that for MTPA that the $i_{d,ref}$ is calculated based on the relationship shown in equation (5.23). The complete illustration of what the TC and ABS blocks in Figure 5.26 can be seen in Figure 5.27.

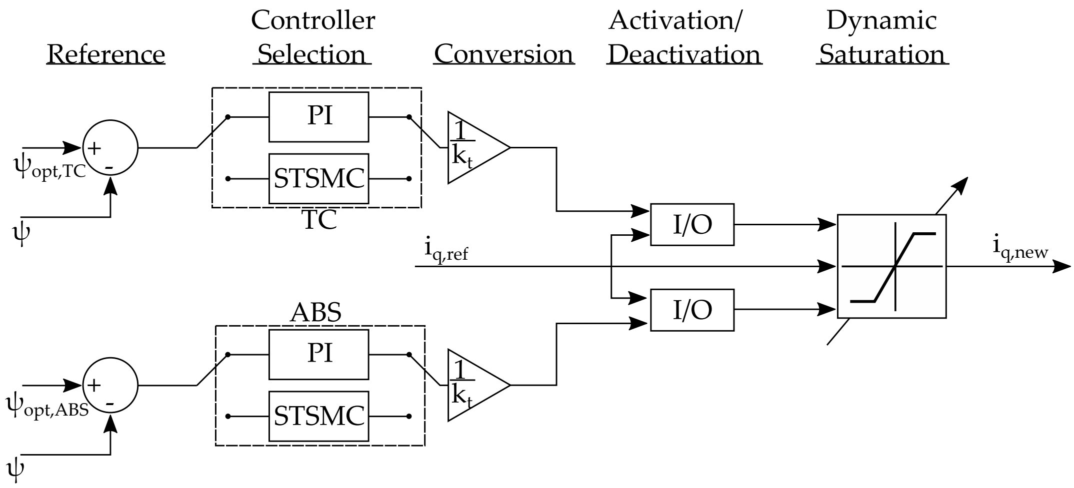

Figure 5.27: Detailed illustration of how slip control is implemented in the Matlab Simulink

As seen from figure 5.27 the slip control has five steps.

- 1. Slip reference error is calculated
- 2. Either the linear or nonlinear controller is selected to be used
- 3. The torque command from either TC/ABS is converted from a torque command to a current command
- 4. The activation/deactivation logic is used to determine whether or not the controller is activated
- 5. The outputs from TC/ABS are used to adjust the dynamic saturation block which is used to adjust the i_q current reference such that the motor torque supplied by the PMSM to the wheel generates the optimal slip ratio conditions between the tire and the road.

With the complete model described and how it is implemented it is now possible to move on to the results chapter.

Chapter 6

Test and Results

With the complete assembly of both motor control and extended motor control it is now possible to test the simulated response of the AAUER. The aim of this chapter will be to prove and validate various aspects of this project. The chapter is divided into two sections. The first section aims to test and verify various components of the AAUER driveline in Matlab Simulink. The second part of the chapter will be a simulated version of the 2012 Hockenheim FSG competition. This means that the matlab simulink version of the AAUER will be tested in all the dynamic events, excluding the skidpad event. The model of the AAUER used for all of the simulation is described in figure 5.26. The list of simulations done in section 6.1 is as follows

- Test of the Slip Control
- Regenerative Braking Test
- Test of different motor control methods
- Change in road conditions during operation

For section 6.2 the order of the events are,

- Acceleration event comparison of slip controllers
- Autocross event with comparison of slip controllers
- Full Endurance event SoC investigation

The different competitions described in chapter 1 will serve as a means to test the different scenarios the AAUER will experience. As mentioned previously, the track used is described in section 2.1.1 and the speed reference which the AAUER needs to follow in order to complete a single lap of the endurance race as well. At the beginning of each test a table is presented which displays the settings under which the simulation was performed. This is done in order to make it more clear which conditions are being tested when and under what circumstances.

6.1 Verification of components

6.1.1 Traction Control and Anti-block System

	Value
Race Type	Acceleration
Control Method	FoC
Slip Control	Slip Control On/Off
Regen Braking	Regen Braking On
Slip Control Method	Linear

Table 6.1: Settings for the slip control test.

The first two tests are done on the TC and the ABS to demonstrate the AAUER performance with and without slip control. During the acceleration of the AAUER the TC is active, this is then followed by an immediate braking even where the AAUER has to brake from $100[\frac{km}{hr}]$ back down to zero.

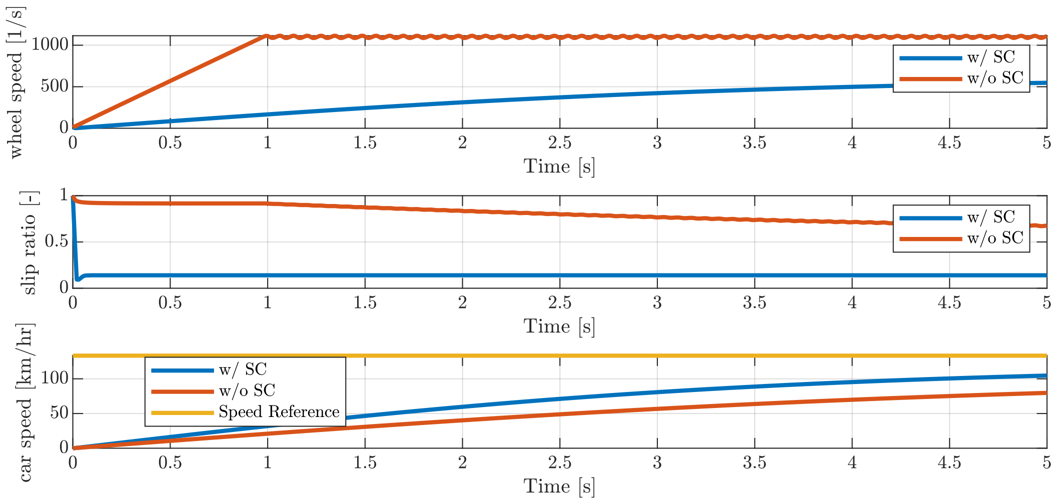

Figure 6.1: linear TC and ABS plots with full throttle

As seen from Figure 6.1 the slip controller performs as intended, keeping the AAUER at optimal slip during acceleration. Without the slip controller the AAUER is given full throttle results in a slip at or in the vicinity of one. Furthermore, after $1[s]$ the wheel speed without slip control reaches the rated speed. This then means that the AAUER without slip control is accelerated sub-optimally.

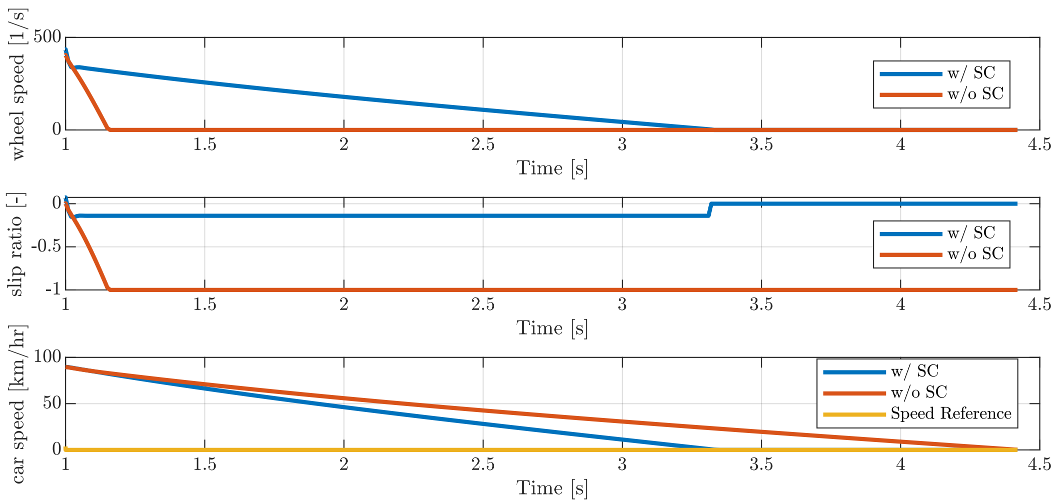

Figure 6.2: linear TC and ABS plots with full throttle

For simulation reasons the ABS test is performed $1[s]$ into the simulation such that both wheel and car speed match at the beginning of the test. As seen from Figure 6.6 the ABS controls the slip according to the constant reference it has been given. This is reflected in the wheel speed as well. Compared to the brake test without slip control, it can be seen that the fastest way to brake the AAUER from $100[\frac{km}{hr}]$ to zero is not by locking the wheel, as is done without slip control.

6.1.2 Energy Saved via Regenerative Braking

The settings in table 6.2 were used to produce Figure 6.3. The track which regenerative braking is tested on is the autocross event.

	Value
Race Type	Autocross
Control Method	FoC
Slip Control	Slip Control On
Regen Braking	Regen Braking On/Off
Slip Control Method	Linear

Table 6.2: Settings for Regenerative Braking test

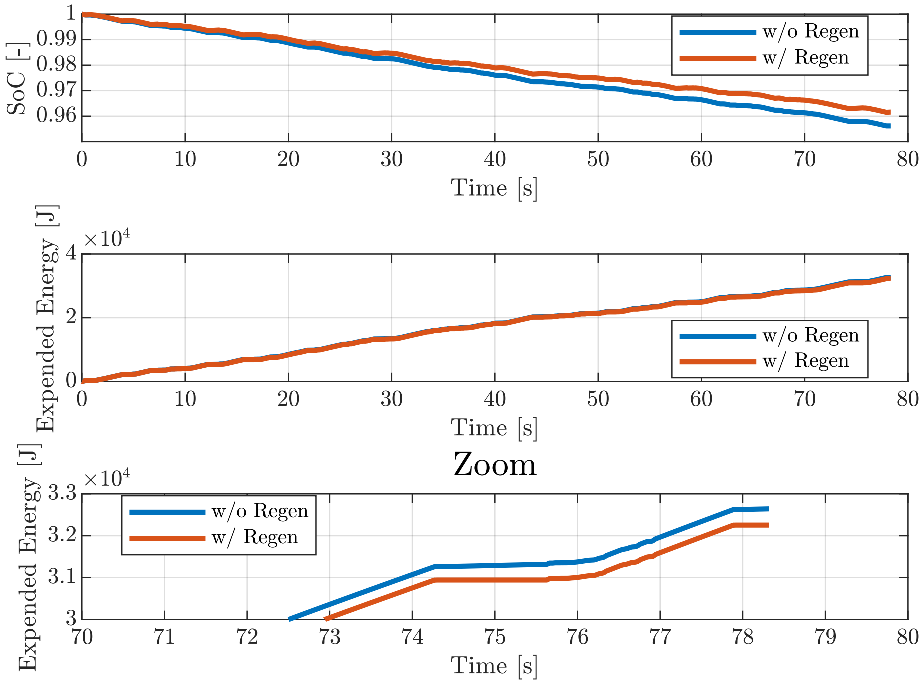

Figure 6.3: Comparison of AAUER performance with and without regenerative braking for one lap.

	SoC	Energy Expended
w/o Regen	0.9562[s]	32.25[kJ]
w/ Regen	0.9616[$-$]	32.64[kJ]

As seen from Figure 6.3 regenerative braking is performing as intended. With regenerative braking it is possible to retrieve approximately 0.39[kJ] , or an additional 0.0054 SoC, during the course of one lap.

6.1.3 FOC and MTPA

The settings in table 6.3 were used to produce Figure 6.4.

	Value
Race Type	Autocross
Control Method	FoC/MTPA
Slip Control	Slip Control On
Regen Braking	Regen Braking Off
Slip Control Method	Linear

Table 6.3: Settings used for producing Figure 6.4.

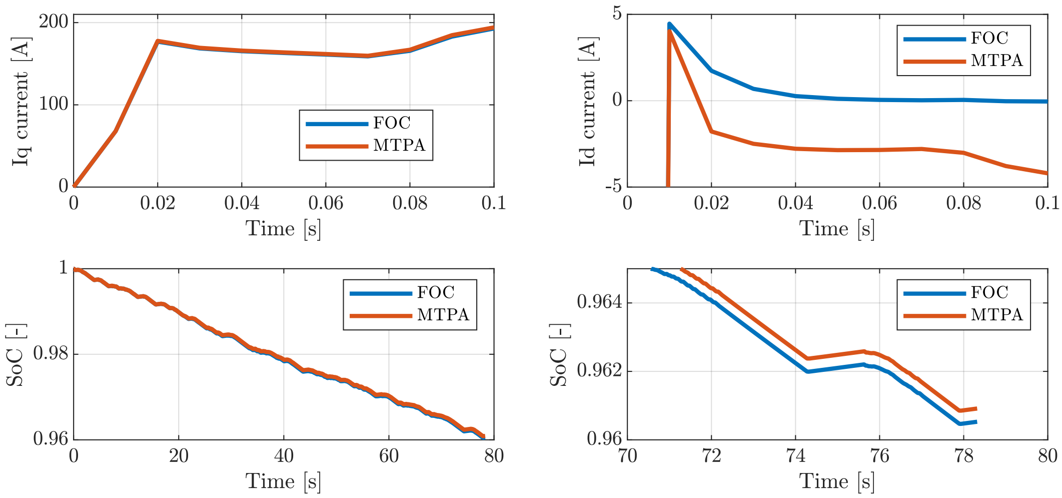

Figure 6.4: MTPA and FOC comparison

As can be seen from Figure 6.4 both FoC and MTPA are very similar in performance. Furthermore, it can be seen that MTPA and FoC both work as intended. This can be seen in the top right plot of figure 6.4 where MTPA has a non-zero i_d current and FoC has a zero i_d current once the i_d current controller settles.

6.1.4 Disturbance Rejection: Change in road condition

A test is performed in order to compare the designed linear PI controller with the nonlinear STSMC controller to see how they perform when a sudden change in road surface happens. That is, when the road condition goes from dry to wet tarmac.

	Value
Race Type	Acceleration
Control Method	FoC
Slip Control	Slip Control On
Regen Braking	Regen Braking Off
Slip Control Method	Linear/STSMC

Table 6.4: Disturbance Rejection settings

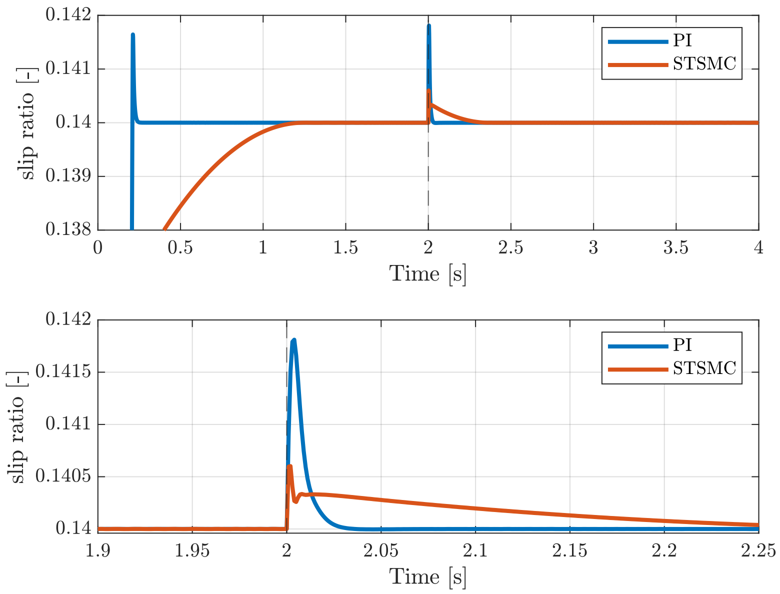

Figure 6.5: PI and STSMC slip control from dry tarmac $t < 1$ to wet tarmac $t \geq 1$.

The first $2[s]$ of the simulation take place on dry tarmac,pre-disturbance, afterwards the road condition is changed to wet tarmac. The initial step,

	Settling time	Overshoot
PI	$0.229[s]$	1.14%
STSMC	$1.16[s]$	0%

The performance of the controllers as the disturbances happens can be seen in table 6.5.

	Settling time	Overshoot
PI	$0.02[s]$	1.29%
STSMC	$0.25[s]$	0.43%

Table 6.5: Controller performance when the road surface is changed

In this instance settling time is calculated as the time it takes from when the disturbance happens to when the slip is within 10% of the reference relative to the peak value. The overshoot once the road condition changes is significantly higher 0.86% relative to 0.29% for the STSMC , however, the linear PI controller rejects the disturbance much faster $0.017[s]$ compared to $0.125[s]$ of the STSMC.

6.2 Events Test

6.2.1 Acceleration Event

In Figure 6.6 the acceleration event is run by setting a constant speed reference to $120[\frac{km}{hr}]$. It is seen that both slip control methods perform similarly in this event. By taking a closer look at the time the AAUER crosses the finish line, it is see that the non-linear STSMC performs slightly better than the linear PI controller.

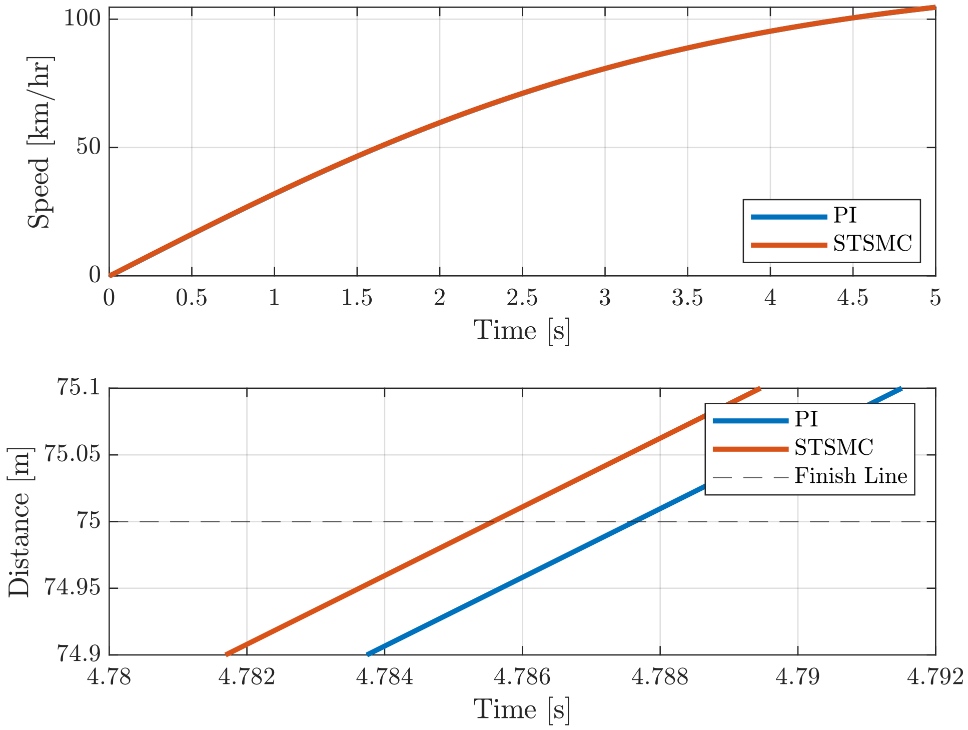

Figure 6.6: Linear vs. Nonlinear slip control for the acceleration event.

	PI	STSMC
speed at 4 [s] mark	$95,3[\frac{km}{hr}]$	$95.33[\frac{km}{hr}]$
time to reach 75 [m]	4.788 [s]	4.786 [s]

Table 6.6

6.2.2 Autocross Event

The linear and nonlinear controller are tested against each other for the autocross event. The results of this test can be seen in Figures 6.7 and 6.8

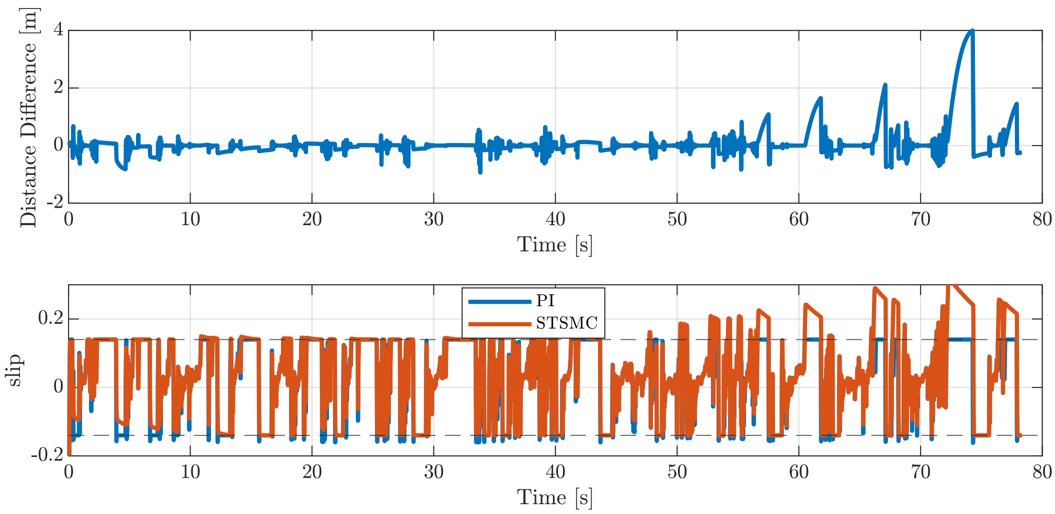

Figure 6.7: Linear vs. Nonlinear slip control for the acceleration event.

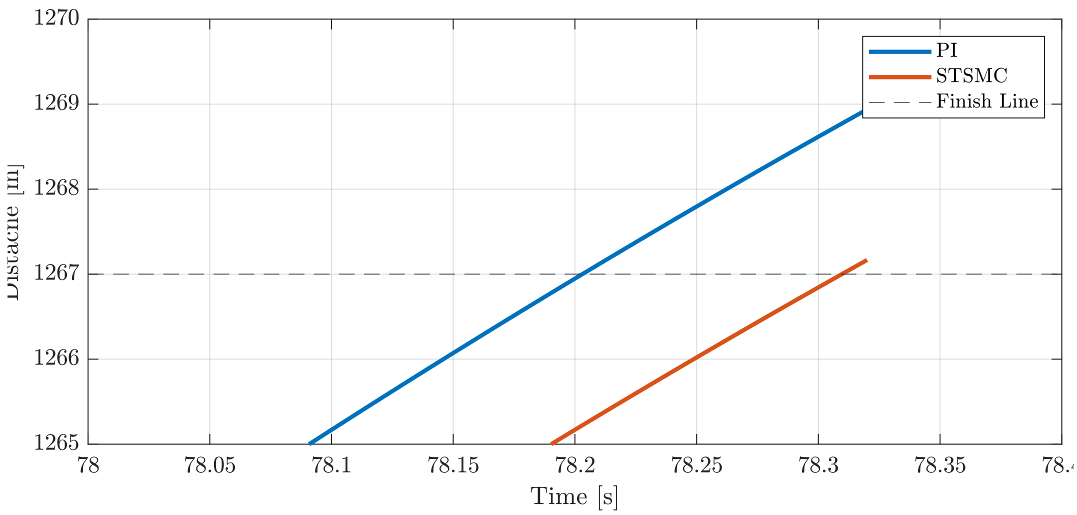

Figure 6.8: Linear vs. Nonlinear slip control for the acceleration event.

From Figures 6.7 and 6.8 it is clear that for the first $60[s]$ that both controllers are very close. However the last $20[s]$ the STSMC shows signs of significant overshoot. A possible reason for this could be the speed reference. That the slow settling time of the STSMC simply means it is unable to converge on the slip reference before the speed reference commands the AAUER to accelerate or decelerate. As a result, the linear slip controller crosses the finish line $0.1[s]$ before the STSMC.

6.2.3 Endurance event + Efficiency event

A full endurance is used to test the battery capacity.

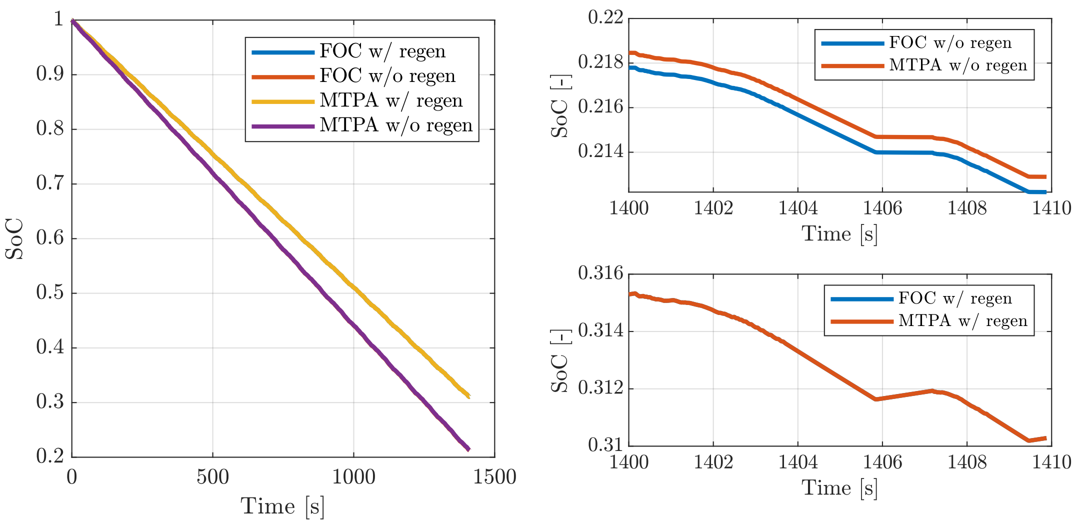

Figure 6.9: MTPA and FOC comparison

	with regen		without regen	
	MTPA	FOC	MTPA	FOC
SoC	0.3103	0.3103	0.2129	0.2122

Table 6.7: SoC results of a complete endurance race.

From figure 6.9 it can be see that almost 0.1 SoC can be saved with the implementation of the regenerative braking. Both FoC and MTPA with regenerative braking save the same amount of energy, one of the reasons for this could be the implementation of regenerative braking in the Matlab SimuLink model.

6.3 Score Comparison from FSG 2012

The scores for the AAUER in the different events are shown in section 6.3. The scores are found from [9]. The equations used to calculate the scores shown in Appendix C.

	AAUER	Best of FSG 2012	score
Acceleration	4.790 [s]	3.454 [s]	15.17
Autocross	78.32 [s]	75.93 [s]	87.33
Endurance	1409,76 [s]	1420.56 [s]	325
Efficiency	0.0093 [kWh]	0.153 [kWh]	100
Total Score			527.5

Chapter 7

Discussion and Conclusion

7.1 Discussion

The slip controllers are both able to perform to expectations. In the acceleration event, the STSMC gives a slightly faster event time. In the road surface test, the STSMC has a smaller deviation in slip, while the PI has faster convergence to the reference value. From the endurance simulations, it was seen that using MTPA saves a small amount of energy. This is expected as the saliency of the EMRAX 228 is close to one thus the reluctance torque is small and does not contribute much.
From the endurance simulations, it is seen that regenerative braking works as expected by recharging the battery pack. While the pack is not limited by its capacity, but rather current limits, it is largely due to the use of the INR18650-35e cell. As a result, an area that can be improved upon is the choice of battery cell for the battery pack. In this case, a battery cell that has a higher charge and discharge current would be favorable compared to more capacity. From Figure 6.9 it can be seen that the battery pack capacity is not an issue.
Another interesting point from chapter 6, Figure 6.4, is the application of MTPA on a PMSM which is almost non-salient. As can be seen from Figure 6.4, MPTA performs better than FoC despite the almost non-salient nature of the PMSM. In a competition such as the FSAE events, it seems that the MPTA provides sufficiently good results to warrant use.
Another issue that has not been considered is how the slip control is activated. As it stands currently, the activation and deactivation of the slip controller is solely based on the sign of the i_q current. For practical implementation, it cannot be expected that the i_q current signal is without noise and as such, any noise which is inevitably added to the signal will distort the activation signal significantly. A possible solution could be to combine the qualities of the i_q current signal with the change in slip ratio. Since the i_q current signal indicates whether or not the motor is braking or accelerating. At the same time, the change in slip ratio is a relatively

less noisy signal, and the change in slip ties directly to the behavior of the AAUER itself.
It could also be interesting to investigate the robustness of the different slip controllers further. With the need for vehicle speed for slip control to work and the noise added from the current sensor, there is a potential for a significant amount of noise being present in a practical implementation of the suggested system seen in Figure 5.26. Despite the STSMC being the slower of the two control methods. In a practical implementation with the presence of noise, the robustness of the STSMC might mean that it will outperform the linear controller.

7.2 Conclusion

From figure 6.4 it was seen that MTPA does not contribute significantly to the AAUERs performance or energy-saving measures even though it does not require any extra components. Regenerative braking was seen to have a significant effect on the AAUERs SoC after an endurance, as 10% could be recovered. This could be used as an increased buffer to compensate for extra energy usage or excessively aggressive driving. Slip control was seen to be not only a necessity but also great performance-enhancing for both the acceleration event but also autocross and endurance. It can be seen that both TC and ABS significantly improve acceleration rate and deceleration rate. The difference between nonlinear and linear slip control is small. However, toward the end of the autocross event, the difference between linear and nonlinear slip control became apparent when the nonlinear controller was unable to maintain the optimal slip reference for TC. This leads to the conclusion that the best combination of control methods for the AAUER will be MTPA combined with regenerative braking and the linear PI slip controller.

7.3 Future Work

There were many aspects of the investigation of the AAUER which were not considered due to time constraints. Some of these subjects include,

- Double corner model
- Max adhesion as a function of slip estimation
- SoC estimation of the battery / SoP
- Experimental setup

The wheel/car model considered in this project was a single corner model. That means that only forces related to the longitudinal motion of the car were considered. This is a good approximation in most cases, however, the added complexity

of the double corner model allows for investigation of lateral motion as well. This becomes a subject of interest when cornering is considered. This would give a better insight into the performance of the AAUER in the skidpad event, for example. A double corner model would also give a better representation of the AAUER's ability to accelerate and brake since chassis heave is not accounted for in the single corner car model, that is, the normal force on the wheels is considered constant. Another interesting vehicle control method that was not implemented but if implemented could improve the AAUER, would be torque vectoring.
Something else which was not considered but would be a subject of interest is the estimation of the optimal slip for a given surface. With such a tool it would be possible to give the slip controller a dynamic optimal slip reference which would change depending on the road condition. This would remove the need for having a driver deciding whether or not the slip reference should be set to dry or wet tarmac.
Finally, it is known that the current estimation technique used to determine the SoC of the battery pack, Coulomb counting, is prone to drift as time passes. An alternative solution to determine the SoC would be to use another form of estimation technique. Thus, removing the issues related to Coulomb counting. All results shown in this thesis have been based purely on simulations. While some data was used in the construction of the mathematical model of the battery pack and the adhesion model, a real-life test would show the model to be accurate and show the control methods presented to work as designed. Tests such an acceleration event would be prudent to see the performance of the slip controllers. Driving an endurance in the AAUER would prove whether the design of the battery package would hold up to the design specifications, especially in regards to temperature variations, which have not been considered in this thesis. Redesign battery pack with different cells for a better fit to the task. Use of a cell with a discharge and charging current limits close to the same value, could lower the number of parallels needed in the AAUER.

Appendices

Appendix A

System Parameters

This appendix servers as a library of parameters throughout the paper.

Car parameters

parameter	value	Description
B_{roll}	0.03 $[\frac{N}{m/s}]$	Rolling Resistance
ρ	1.2 $[\frac{kg}{m^2}]$	Air Density
A	0.81 $[m^2]$	Cross-sectional Area
C_d	0.35 $[-]$	Drag Coefficient
M_v	291 $[kg]$	Mass of Vehicle
R_w	250 $[mm]$	Wheel Radius
L	1601 $[mm]$	Length of Vehicle

The parameters in chapter A have been extracted from a solid works model or measured on the G8.

EMRAX motor parameters

parameter	value	Description
L_q	177 $[\mu H]$	q-axis Inductance
L_d	183 $[\mu H]$	d-axis Inductance
$V_{DC,max}$	680 $[V]$	Max Voltage Capacity
$\omega_{r,max}$	5500 $[rpm]$	Max rpm
N_{pp}	10 $[-]$	Number of Pole Pairs
J_m	0.0383$[kgm^2]$	Motor Intertia
λ_{mpm}	0.0542 $[\mu H]$	Maximum Magnetic Flux
R_s	16.7 $[m\Omega]$	Internal Phase Resistance

All of the above values for the EMRAX parameters can be found in [4].
A single cell has the following specifications All of the above battery specifications for the single cell are found in [29]

EMRAX motor parameters

parameter	value	Description
U_c	4.2 $[V]$	Charging Voltage
$U_{cuttoff}$	2.65 $[V]$	Cutt-off Voltage
Q_{bat}	3,400 $[mA]$	Nominal Capacity of a single cell
$I_{discharge,continuous}$	8 $[A]$	Maximum Continuous Discharge Current
$I_{discharge,peak}$	13 $[A]$	Maximum Peak Discharge Current

Appendix B

Optimum Lap

This appendix servers as a introduction to the software Optimum Lap.

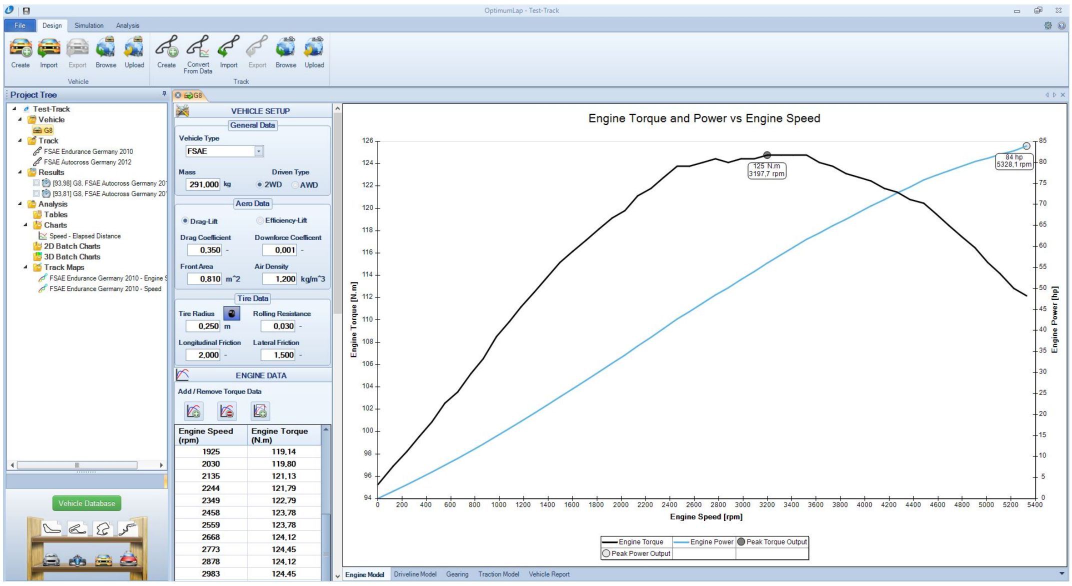

Figure B.1: Screenshot of Optimum Lap, showing the torque/power speed curve

The parameters specified for the car in Optimum Lap are shown in Table B.1. Parameters such as Drag and Down force coefficients, lateral friction and car mass are estimates, while remaining parameters are calculated from data or measured. Optimum Lap uses the specified parameters and a premade track which is specified by its corner radius' and length. It then simulates a point mass moving around the track with limitations set by the parameters. A limitation such as lateral friction would mean the car would not be allowed to move faster in a corner than the lateral friction force would be able to balance out the centrifugal force.

Parameter	Value/Type
Car Mass	291 $[kg]$
Driven Type	Rear Wheel Drive
Drag Coef	0.35
Downforce Coef	0.001
Front Area	0.81 $[m^2]$
Air Density	1.2 $[\frac{kg}{m^3}]$
Tire Radius	0.25 $[m]$
Rolling Resistance	0.03 $[\frac{N}{m/s}]$
Logitudinal Friction	2
Lateral Friction	1.5
Thermal Efficiency	90%
Drive efficiency	90%
Final Drive Ratio	4.5

Table B.1: Car parameters used in Optimum Lap

Appendix C

Event Scoring calculations

The following equations and text is based on the ruleset from Formular Student Germany(FSG)

C.1 Skidpad

3.5 points are awarded to every team that finishes one run. The run time is the average of the right and left time, with penalties added after averaging. T_{team} is the best run time including penalties and T_{max} is 1.25 times the time of the fastest vehicle including penalties. If a team's run time is below T_{max}, additional points are giving based on equation (C.1)

$$additionalscore = 71.5\left(\frac{\left(\frac{T_{max}}{T_{min}}\right)^2 - 1}{0.5625}\right) \tag{C.1}$$

C.2 Acceleration

3.5 points are awarded to every team that finishes one run. T_{team} is the best run time including penalties and T_{max} is 1.50 times the time of the fastest vehicle including penalties. If a team's run time is below T_{max}, additional points are giving based on equation (C.2)

$$additionalscore = 71.5\left(\frac{\left(\frac{T_{max}}{T_{min}} - 1\right)}{0.5}\right) \tag{C.2}$$

C.3 Autocross

4.5 points are awarded to every team that finishes one run. T_{team} is the best run time including penalties and T_{max} is 1.25 times the time of the fastest vehicle including penalties. If a team's run time is below T_{max}, additional points are giving based on equation (C.3)

$$additionalscore = 95.5\left(\frac{\left(\frac{T_{max}}{T_{min}} - 1\right)}{0.25}\right) \tag{C.3}$$

C.4 Endurance

25 points are awarded to every team that finishes one run. T_{team} is the best run time including penalties and T_{max} is 1.333 times the time of the fastest vehicle including penalties. If a team's run time is below T_{max}, additional points are giving based on equation (C.4)

$$additionalscore = 300\left(\frac{\left(\frac{T_{max}}{T_{min}} - 1\right)}{0.333}\right) \tag{C.4}$$

C.5 Efficiency

Energy efficiency is measured during the endurance event. The energy is calculated as the time integrated voltage multiplied by the measured current. Regenerated energy is multiplied by 0.9 and subtracted from the used energy. Teams whose uncorrected time is greater than 1.333 time the uncorrected time for the fastest vehicle, receives zero points for efficiency. If a team finishes the endurance event, efficiency points are awarded based on equation (C.5)

$$additionalscore = 100\left(\frac{\frac{0.1}{E_{Team}} - 1}{\frac{0.1}{E_{max}} - 1}\right) \tag{C.5}$$

E_{team} is the team's efficiency factor E_{max} is the highest efficiency factor. Efficiency factor is calculated by equation (C.6)

$$efficiencyfactor = \frac{T_{min} \cdot EN_{min}^2}{T_{team} \cdot EN_{team}^2} \tag{C.6}$$

T_{team} is the team's uncorrected time and T_{min} is the fasted driving time of teams that score points in efficiency. EN_{team} is the team's corrected used energy and EN_{min} is the lowest corrected energy used by the teams who score points in efficiency.

Appendix D

Battery Parameters Data

The battery cell data which is presented in this section is of a Samsung INR18650-35E 3.6V / 3400mAh Li-ion max 10.5A battery. This data has been provided to us by Erik Schaltz. The following data were measured at 35° at different SoCs.

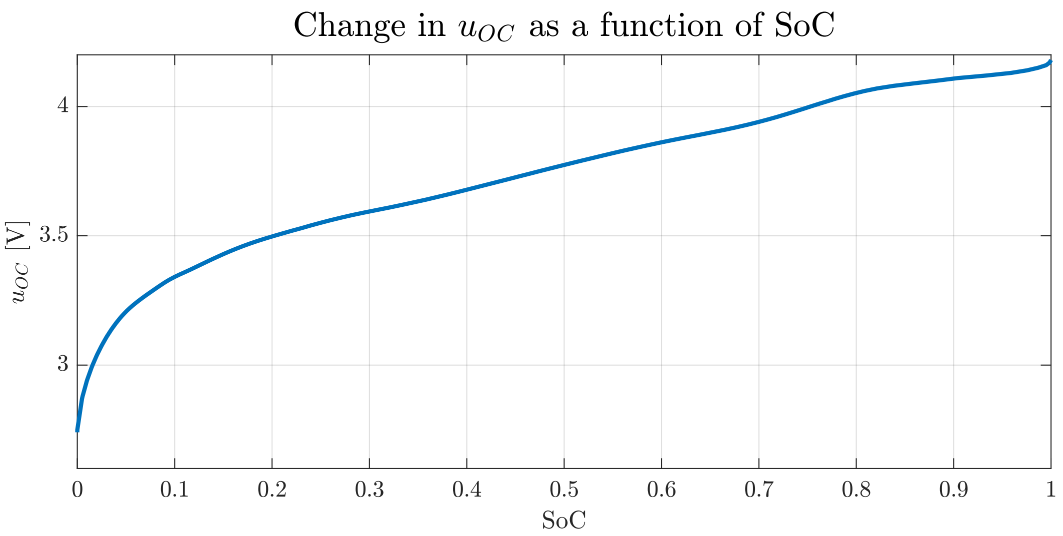

Figure D.1: Screenshot of Optimum Lap, showing the torque/power speed curve

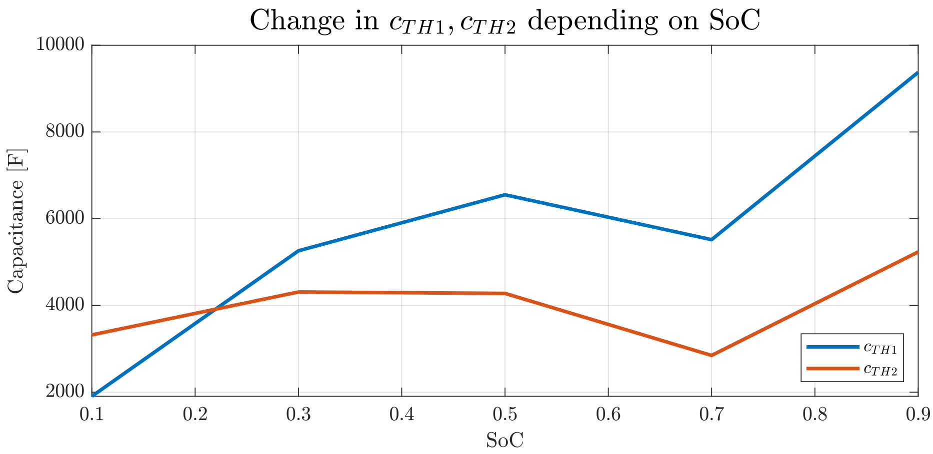

Figure D.2: Screenshot of Optimum Lap, showing the torque/power speed curve

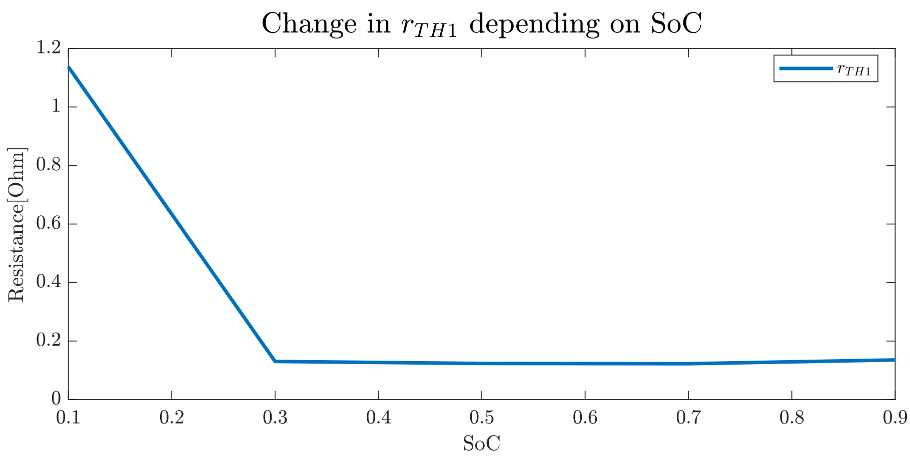

Figure D.3: Screenshot of Optimum Lap, showing the torque/power speed curve

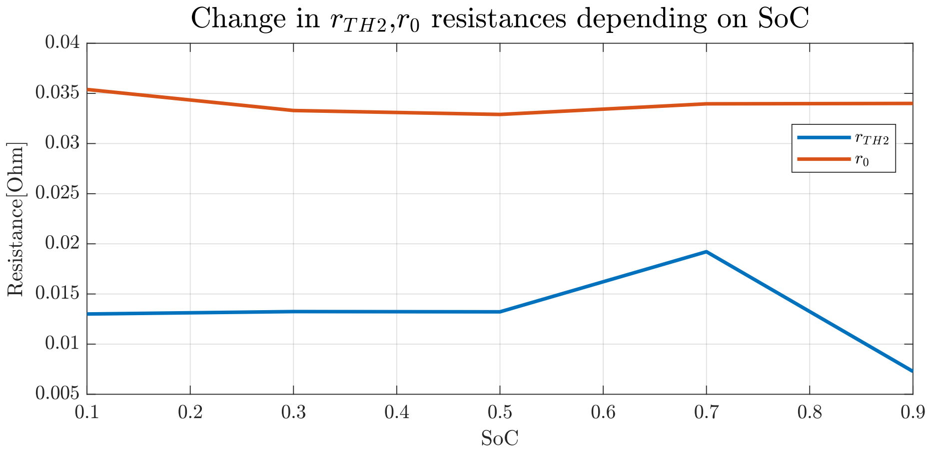

Figure D.4: Screenshot of Optimum Lap, showing the torque/power speed curve

The nominal capacitance of the battery cell is

- $C_N = 3.4$

Bibliography

[1] Mads Hellegaard Andersen and Rune Wiben. *Design of Slip-based Active Braking and Traction Control System for the Electric Vehicle QBEAK*. Tech. rep. Aalborg University, 2012, p. 157.

[2] Wuwei Chen et al. *Integrated Vehicle Dynamics and Control*. John Wiley & Sons, Incorporated, 2016, p. 373. ISBN: 9781118380017. URL: https://ebookcentral.proquest.com/lib/aalborguniv-ebooks/detail.action?docID=4501301{\&}pq-origsite=primo{\#}.

[3] Mehrdad Ehsani, Yimin Gao, and Ali Emadi. *Modern electric, hybrid electric, and fuel cell vehicles fundamentals, theory, and design*. Ed. by Muhammad H Rashid. Second. Vol. 1. 1. NW: CRC Press, 2010, p. 558.

[4] EMRAX.com. *Manual for EMRAX Motors / Generators*. Tech. rep. 2020, p. 57. URL: https://emrax.com/wp-content/uploads/2020/03/manual{_}for{_}emrax{_}motors{_}version{_}5.4.pdf.

[5] *Event scores FSG*. URL: https://www.formulastudent.de/about/disciplines/.

[6] Mohammad Farshadnia. *Advanced Theory of Fractional-Slot ConcentratedWound Permanent Magnet Synchronous Machines*. 2018, p. 266. ISBN: 2190-5061. DOI: 10.1007/F978-981-10-8708-0.

[7] *FSAE car friction coefficient*. URL: http://share.optimumg.com/vehicles/?page=2.

[8] *FSAE rules book*. URL: https://www.formulastudent.de/fileadmin/user_upload/all/2020/rules/FS-Rules_2020_V1.0.pdf.

[9] *FSG Hockenheim Scores*. URL: https://www.formulastudent.de/fsg/results/2012/.

[10] *FSG Ruleset*. URL: https://www.formulastudent.de/fileadmin/user_upload/all/2020/rules/FS-Rules_2020_V1.0.pdf.

[11] Anirudh Guha and G. Narayanan. "Average modelling of a voltage source inverter with dead-time in a synchronous reference frame". In: *2013 IEEE Innovative Smart Grid Technologies - Asia, ISGT Asia 2013* (2013), pp. 1–6. DOI: 10.1109/ISGT-Asia.2013.6698746.

[12] Fredrik Gustafsson. "Slip-based tire-road friction estimation". In: *Automatica* 33.6 (1997), pp. 1087–1099. ISSN: 00051098. DOI: 10.1016/s0005-1098(97)00003-4.

[13] Hongwen He, Rui Xiong, and Jinxin Fan. "Evaluation of Lithium-Ion Battery Equivalent Circuit Models for State of Charge Estimation by an Experimental Approach". In: *energies* (2011), pp. 582–598. DOI: 10.3390/en4040582. URL: www.mdpi.com/journal/energies.

[14] Rolf Isermann. *Fahrdynamik-Regelung: Modellbildung,Fahrerassistenzsysteme, Mechatronik*. GWV Facheverlage GmbH, 2006, p. 460. ISBN: 978-3-8348-0109-8. URL: https://books.google.dk/books?id=LLqlkqmXryMC&pg=PA37#v=onepage&q&f=false.

[15] Hag Wone Kim et al. "Nonlinearity estimation and compensation of PWM VSI for PMSM under resistance and flux linkage uncertainty". In: *IEEE Transactions on Control Systems Technology* 14.4 (2006), pp. 589–601. ISSN: 10636536. DOI: 10.1109/TCST.2006.876622.

[16] Il Song Kim. "A technique for estimating the state of health of lithium batteries through a dual-sliding-mode observer". In: *IEEE Transactions on Power Electronics* 25.4 (2010), pp. 1013–1022. ISSN: 08858993. DOI: 10.1109/TPEL.2009.2034966.

[17] Moad Kissai et al. "A new linear tire model with varying parameters To cite this version : HAL Id : hal-01690792 A New Linear Tire Model With Varying Parameters". In: (2018).

[18] Paul Krause et al. *Analysis of Electric Machinery and Drive Systems*. Third. 2013, p. 635. ISBN: 978-1-118-02429-4.

[19] Languang Lu et al. "A review on the key issues for lithium-ion battery management in electric vehicles". In: *Journal of Power Sources* 226 (2013), pp. 272–288. ISSN: 03787753. DOI: 10.1016/j.jpowsour.2012.10.060. URL: http://dx.doi.org/10.1016/j.jpowsour.2012.10.060.

[20] MathWorks. *Tire-Road Interaction (Magic Formula)*. 2011. URL: https://se.mathworks.com/help/physmod/sdl/ref/tireroadinteractionmagicformula.html.

[21] Hossein Mirzaeinejad and Mehdi Mirzaei. "A novel method for non-linear control of wheel slip in anti-lock braking systems". In: *Control Engineering Practice* 18.8 (2010), pp. 918–926. ISSN: 09670661. DOI: 10.1016/j.conengprac.2010.03.015. URL: http://dx.doi.org/10.1016/j.conengprac.2010.03.015.

[22] A. Munoz-Garcia and T. A. Lipo. "On-line dead time compensation technique for open-loop PWM-VSI drives". In: *Conference Proceedings - IEEE Applied Power Electronics Conference and Exposition - APEC* 1.608 (1998), pp. 95–100. DOI: 10.1109/apec.1998.647675.

[23] Ching Tsai Pan and Shinn Ming Sue. "A linear maximum torque per ampere control for IPMSM drives over full-speed range". In: *IEEE Transactions on Energy Conversion* 20.2 (2005), pp. 359–366. ISSN: 08858969. DOI: 10.1109/TEC.2004.841517.

[24] Charles L. Phillips and John M. Parr. *Feedback Control Systems*. 5th. Pearson, 2013, p. 778. ISBN: 978-93-325-0760-9.

[25] Gianfranco Pistoia and Boryann Liaw. *Behaviour of Lithium-Ion Batteries in Electric Vehicles Battery Health, Performance, Safety, and Cost*. Green Energy and Technology, 2018, p. 343. ISBN: 978-3-319-69949-3. DOI: 10.1007/978-3-319-69950-9. URL: https://link.springer.com/book/10.1007{\%}2F978-3-319-69950-9.

[26] Kachroo Pushkin and Tomizuka Masayoshi. *Vehicle Traction Control and Its Applications*. Tech. rep. 1995, p. 44.

[27] Muhammed H. Rashid. *Power Electronics: Devices, Circuits, and Applications*. Fourth Edi. Pearson Educaion, 2014, p. 1022. ISBN: 978-0-13-312590-0.

[28] Andrius Ružinskas and Henrikas Sivilevičius. "Magic Formula Tyre Model Application for a Tyre-Ice Interaction". In: *Procedia Engineering* 187 (2017), pp. 335–341. ISSN: 18777058. DOI: 10.1016/j.proeng.2017.04.383.

[29] Samsung. *Samsung INR18650-35E 3.6V /3400mAh Li-ion max 10.5A*. URL: https://www.batteribyen.dk/samsung-inr18650-35e-3-6v-3450mah-li-ion-max-10-5a.

[30] Sergio M. Savaresi and Mara Tanelli. *Active Braking Control Systems Design for Vehicles*. Ed. by Michael J Grimble and Michael A Johnson. Vol. 53. Springer, 2013, p. 269. ISBN: 978-1-84996-349-7. DOI: 10.1007/978-1-84996-350-3. arXiv: arXiv:1011.1669v3.

[31] Y. Shtessel, Christopher Edwards, and Leonid Fridman. *Sliding Mode Control and Observation, Series: Control Engineering*. Vol. 10. Birkhauser, 2016, p. 356. ISBN: 978-0-81764-8923. DOI: 10.1007/978-0-8176-4893-0. URL: http://www.springer.com/gp/book/9780817648923{\#}reviews.

[32] Jean-Jacques Slotine and Weiping Li. *Applied Nonlinear Control*. Pearson (1991), 1991, p. 461. ISBN: 0-12-040890-5.

[33] M Stern and Geary A.L. "Electrochemical Polarization I. A Theoretical Analysis of the Shape of Polarization Curves". In: *JOURNAL OF THE ELECTROCHEMICAL SOCIETY* 104 (1957), pp. 56–63. DOI: 10.1149/1.2428496. URL: https://iopscience.iop.org/article/10.1149/1.2428496/pdf.

[34] Adam Michael Szechy. "Traction and Launch Control for a Rear-Wheel-Drive Parallel-Series Plug-In Hybrid Electric Vehicle". In: (2016). URL: https://commons.erau.edu/cgi/viewcontent.cgi?article=1314{\&}context=edt.

[35] John Warner. "Battery Pack Design Criteria and Selection". In: *The Handbook of Lithium-Ion Battery Pack Design*. Elsevier, 2015. Chap. 4. ISBN: 978-0-12-801456-1. DOI: 10.1016/B978-0-12-801456-1.00004-X.

[36] Low Wen Yao et al. "Modeling of lithium-ion battery using MATLAB/simulink". In: *IECON Proceedings (Industrial Electronics Conference)* (2013), pp. 1729–1734. DOI: 10.1109/IECON.2013.6699393.

[37] Guangzhen Zhang et al. "Analysis and optimization of current regulator time delay in Permanent Magnet Synchronous Motor drive system". In: *2013 International Conference on Electrical Machines and Systems, ICEMS 2013* 4.5 (2013), pp. 2286–2290. DOI: 10.1109/ICEMS.2013.6713235.

[38] Tao Zhang, Baolian Liu, and Huiping Zhang. "Direct torque control of permanent magnet synchronous motor". eng. In: *Proceedings of the 29th Chinese Control Conference*. IEEE, 2010, pp. 3358–3361. ISBN: 9781424462636.

[39] You Qun Zhao et al. "Estimation of Road Friction Coefficient in Different Road Conditions Based on Vehicle Braking Dynamics". In: *Chinese Journal of Mechanical Engineering (English Edition)* 30.4 (2017), pp. 982–990. ISSN: 21928258. DOI: 10.1007/s10033-017-0143-z.

[40] Keliang Zhou and Danwei Wang. "Relationship Between Space-Vector Modulation and Three-Phase Carrier-Based PWM: A Comprehensive Analysis". In: 49.1 (2002), pp. 186–196.